ROI DETECTION IN SPR MEASUREMENTS AND MOLECULE BINDING PARAMETER ESTIMATION

A thesis presented to the faculty of the Graduate School of
Western Carolina University in partial fulfillment of the
requirements for the degree of Master of Science in Technology.

By

Le Chen

Director: Dr. Yanjun Yan
Assistant Professor
Department of Engineering and Technology

Committee Members:
Dr. Peter Tay, Department of Engineering and Technology
Dr. Martin Tanaka, Department of Engineering and Technology

April 2015

ACKNOWLEDGEMENTS

Firstly, I am sincerely grateful to all the faculty members of Kimmel School for their assistance and support during the past two years. My gratitude is extended to my committee members Dr. Peter Tay and Dr. Martin Tanaka for their guidance and encouragement.

I would like to thank Dr. Weiguo Yang for his help and advice on my Ph.D. application.

Many thanks go to my fellow graduate students, AL Matthews, Cole Drawdy, Nathan Thomas, Yuanrui Sang , Zhou Yang and all other classmates for their patience and help during my past two years of study.

My utmost thanks go to my advisor, Dr. Yanjun Yan. Thank you for your encouragement, willingness to help and advise on issues far beyond this degree. You are not just the advisor during my study in the Kimmel School, but also an example of excellence as a researcher, mentor, instructor, and role model for my life.

Finally, I would like to thank and dedicate this thesis to my family for their endless support.

TABLE OF CONTENTS

LIST OF TABLES

LIST OF FIGURES

ABSTRACT

ROI DETECTION IN SPR MEASUREMENTS AND MOLECULE BINDING PARAMETER ESTIMATION

Le Chen, M.S.T.

Western Carolina University (April 2015)

Director: Dr. Yanjun Yan

Since 1983 when Surface Plasmon Resonance (SPR) was first proposed, it has become a widely-used methodology for various biosensing applications. In a SPR biosensing system in array format, locating the region of interest (ROI) and estimating the molecule binding parameters from the SPR measurements are of great importance. In this thesis, we addressed these two challenges by detecting the ROIs automatically and estimating the parameters optimally through the minimization of the mean square error (MSE).

We first pre-processed the SPR video frame images to help enhance the ROI detection performance, and then applied the randomized Hough transform to automatically detect the ROIs. With hundreds or even thousands of ROIs on a single SPR video frame image, our procedure to automatically detect the ROIs greatly reduced the labor to assign the ROIs.

We then extracted the image gray level intensity data from the ROIs as a function of time, which were used to estimate the molecule binding parameters, k_a (the rate of association) and k_d (the rate of dissociation). These binding parameters are vital in biosensing applications. In this research we use a Particle Swarm Optimization (PSO) algorithm to estimate the parameters and compared the performance to the commercially used Levenberg-Marquardt (LM) algorithm, a gradient based algorithm. Our PSO algorithm performed better than LM achieving a much lower MSE for all the active ROIs.

CHAPTER 1: INTRODUCTION

1.1 Background and Motivation

In biomedical research and pharmaceutical industry, biomolecular interaction analysis is crucial to help us to understand what happens when different molecules encounter each other, determine the choice of drug target [5] [6] or help us develop critical antibodies [7]. Hence, identifying and characterizing molecular interactions have become increasingly important in various areas of life science research. Many analytical techniques have been designed to study biomolecular interactions, such as scanning probe microscopy (SPM) [8], attenuated total reflectance infrared spectroscopy (ATR-IR) [9] and spectral ellipsometry [10]. However, these techniques can not perform analysis in real-time and are not sensitive enough for many applications.

Surface plasmons are electro-magnetic waves propagating along the interface between a metal and a dielectric material that satisfy certain properties. First introduced and applied for sensing in 1983, Surface Plasmon Resonance (SPR) [11] has attracted considerable interest because SPR is able to rapidly obtain information on the rate and extent of adsorption or degradation in real time, without the need to label the adsorbate nor prepare samples using a complex procedure. Being real-time, label-free, and highly-sensitive, the SPR technique is desirable and widely used in many fields such as bio-analytical research, environment monitoring, and food safety [12] [13] [14].

There are mainly two categories of SPR experimental systems, developed by Otto and Kretchmann, respectively. The Otto system varies the angles of the incident light to extract the measurements, while the Kretchmann system fine-tunes and then fixes the angle of the incident light [15]. The Kretchmann system will be used in this study and discussed below. A typical SPR instrument includes a flow cell with a slide and a monitoring system. The first group of interactants, called the ligands, are fixed onto a dextran-coated gold surface of the slide. The second interactant, called the analyte, is then injected through the flow cell and traverse the surface of the slide. The intensity of light reflected off the slide surface is affected

by the mass concentration of components at the liquid-surface interface. The interaction of the soluble analyte with the immobilized ligands is observed continuously and directly. The collected SPR measurements contain information on the kinetic rate and equilibrium binding constants for the interaction under investigation. In general, an SPR experiment consists of three steps: experiment, data extraction and signal processing.

Various techniques have been proposed to enhance SPR sensing efficiency and accuracy, such as using high-performance metal and dielectric interface layer [16], applying more stable protein adhesion site [17], and designing different structure of SPR devices for sensing [18]. These approaches have greatly improved SPR sensing technologies and detection results. However, there have not been much discussions on using data processing techniques to optimize the post-processing of SPR measurements. In Chapters 2 and 3, we proposed a procedure to automatically detect the ROIs and to optimally estimate the molecule binding parameters.

In order to extract the SPR measurements at the molecule binding sites, the ROI locations need to be identified. Doing so manually is costly both in labor and time. Furthermore, because estimation of molecule binding parameters from the measurements is the ultimate goal of an SPR system, the accuracy of the estimation is also important. State-of-the-art SPR systems are designed to measure high through-put, small molecule interactions, which places further demands on developing an efficient scheme to detect the ROIs and estimate the molecule binding parameters. This thesis will addressed these issues.

1.2 Objectives

The objective of this study is to use image processing and signal processing techniques to address the problems in the current SPR techniques (details in Chapter 3). Data we used in this research was video captured by PlexArray System and provided by its manufacturer, Plexera©. Specific tasks in this study include:

- Automatic detection the ROIs;

- Extraction of the light intensity signal inside the ROI and reduction of noise;
- Fitting of the extracted data to get SPR parameter k_a and k_d, which determine the rates of association and dissociation.

1.3 Significance of the Study

The molecule binding parameters, or the kinetic constants, are vital parameters for bio-molecular interaction, which are goal of using an SPR system. To determine the kinetic constants of a biomolecular interaction through SPR, the sensorgram must be fitted to the kinetic model. As a result, data extraction and data fitting are crucial. Accurate ROI detection will enable truthful measurement data extraction from within the exact region, and an adaptive fitting algorithm will help obtain a precise estimation of kinetic constants for all the ROIs.

The ROI detection results and the kinetic constant estimation results are presented in Chapter 4, and validate the effectiveness of our approach to process the SPR measurements. Using image processing techniques, we can location the ROIs automatically, which releases researches from tedious manual ROI identification work, and ensures that only the meaningful ROI measurements are used in the kinetic constant estimation. Our PSO algorithm can achieve a smaller MSE between the fitted curve and the measured data than the commercially used LM algorithm providing a more accurate estimation of the kinetic constants.

CHAPTER 2: BACKGROUND

2.1 Surface plasmon resonance theory

In SPR technique, a p-polarized (polarized in the plane of the surface) collimated light beam is passed through the surface between the prism and a glass slide coated with ~50 nm gold (or other metal), and reflected off the thin gold coating in contact with the liquid solution of interest (Figure 2.1). At the gold/solution interface, the incident light beam excites the electron waves which are called surface plasmon. At a certain incident angle near the so-called SPR angle, excitation of the surface plasmons results in nearly complete attenuation of the specularly reflected light intensity. The SPR angle depends on wavelength of the incident light (Figure 2.2). A slight change at the interface (e.g. a change in refractive index or formation of a nanoscale film thickness) will yield a change in SPR signal, allowing precise measurements of thin film properties as well as surface molecular interactions in real-time.

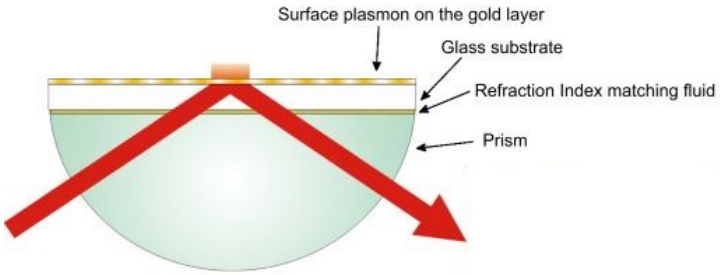

Figure 2.1: Schematic of SPR technique

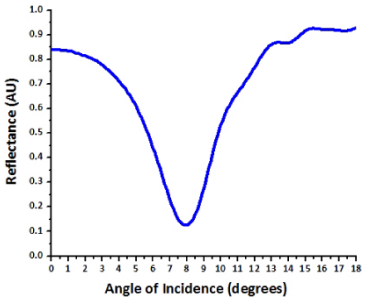

Figure 2.2: SPR Curve. The “dip” is the SPR angle at which the resonance occurs is extremely sensitive to any change in the refractive index (RI) of the medium adjacent to the metal surface, and such changes can be monitored by recording intensity of reflected light when the system goes out of resonance.

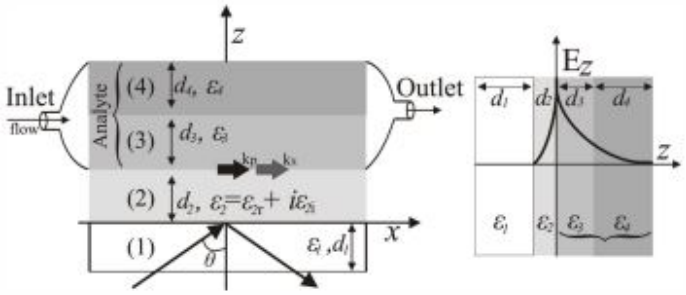

Figure 2.3: The multi-layer system excited with a p-polarized light. Layer (1) is made of K9 optical glass, layer (2) is a 50nm thickness film of gold whereas layers (3) and (4) are application-specific biomedical layers [1].

In the diagram shown in Figure 2.3, the multi-layer system is excited with a p-polarized light, with reflectivity index of layer (j) being n_j, with $j = 1,2,3$. In the study of E.G. Pereira,etc. [1], the vector of the surface plasmon propagating on the interface between layers (2) and (3) is given by

$$k_p = \frac{2\pi}{\lambda}\sqrt{\frac{\varepsilon_2 n_3^2}{\varepsilon_2 - n_3^2}} \tag{2.1}$$

where λ is the light wavelength and ε_2 the metal dielectric constant of layer (2). The component of the wave vector of light in the plasmon direction is given by

$$k_x = \frac{2\pi}{\lambda} n_1 \sin(\theta) \tag{2.2}$$

where θ is the incidence angle.

At a specific angle, called SPR angle (θ_R), k_x and k_p are equal and, consequently, light energy is absorbed, thus reducing surface reflectivity. At resonance, n_3 can be determined by

$$n_3 = \sqrt{\frac{\varepsilon_{2r}[n_1 \sin(\theta_R)]^2}{\varepsilon_{2r} - [n_1 \sin(\theta_R)]^2}} \tag{2.3}$$

where ε_{2r} and ε_{2i} are the the real part and imaginary part of the complex dielectric constant of the metal ($|\varepsilon_{2i}| \ll |\varepsilon_{2r}|$ and thus can be neglected). This means that the refractive index n_3 can be determined by tracking the resonance angle or the light intensity given a fixed resonance anlge [1].

2.2 SPR bio-sensor

Otto and Kretschmann configuration are two principal configurations to achieve plasmon excitation by light. The Kretschmann configuration (Figure 2.4) is used in most SPR bio-sensors, where a metal (usually silver or gold) film is placed at the interface of two dielectric media. Medium 1 is a high refractive index (n1) prism and medium 2 with a lower refractive index (n_2) can be the air or the solutions of interest.

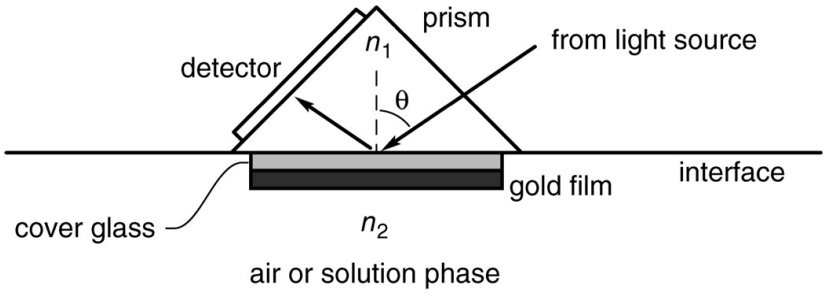

Figure 2.4: Kretschmann configuration of SPR [2]

Figure 2.5 (a) shows the basic schematic of SPR bio-sensor, which includes three main parts: light generator, interface and detector. The light source generates the p-polarized collimated light beam using a led chip, a collimator and a polarizer. The prism and a flow cell, with gold coated chip, can be combined with a range of surfaces to monitor the adsorption

process. On the right side to the prism, a CCD detector is used to detect the SPR signal after being processed by a combination of quarter wave plate, analyzer and imaging lens.

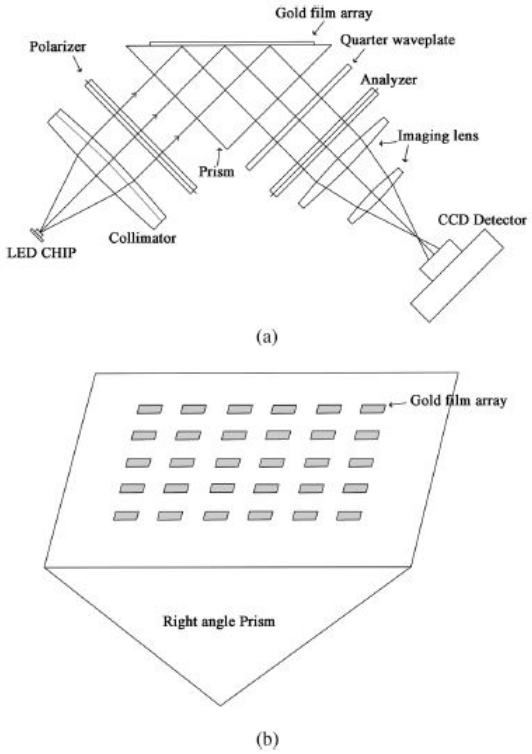

Figure 2.5: Schematic diagram of PlexArray Bio-Sensor [3]

2.2.1 Procedure of SPR sensing experiment for molecule binding

An SPR experiment involves the following several steps:

1. Prepare ligands and analytes.
2. Immobilise the ligands to flow cell.
3. Inject and control analyte over sensor surfaces and record video data.
4. Locate the region of interest and generate SPR sensorgram.
5. Analyse data by fitting SPR sensorgram to a kinetic model.

In this study, we are focusing on the last two steps. Working with the video data generated from step 4, we developed a procedure to automatically locate the region of interest (ROI). Figure 2.6 is a typical video frame of our SPR measurement data. Figure 2.7 shows the SPR curve of a typical bioaffinity interaction experiment. During the binding of the ligand and the analyte (association phase), the light intensity increases until it reaches the equilibrium phase. During the disassociation phase the ligand and analyte dissociate with each other. The experiment ends with rinsing the analyte using a cleaning liquid.

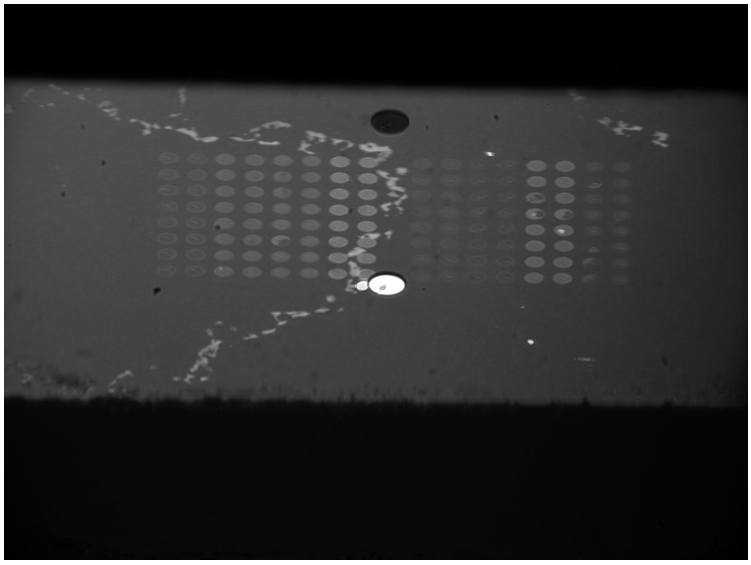

Figure 2.6: Image acquired from the Plexera HT bio-sensor

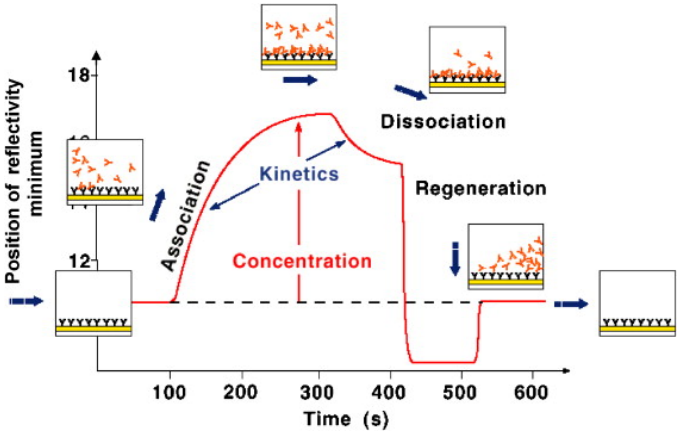

Figure 2.7: Typical SPR curve

2.2.2 SPR sensorgram fitting

To compute the kinetic constants of an interaction between molecules through SPR analysis, the sensorgram must be fitted to a kinetic model. The most commonly used binding model for SPR biosensors is the Langmuir model. It describes a 1:1 interaction in which one ligand molecule interacts with one analyte molecule. In theory, the formation of the ligand-analyte complex follows second-order kinetics. However, because the majority of SPR biosensors are fluidics-based and capable of maintaining a constant analyte concentration in a continuous liquid flow, complex formation actually follows pseudo first-order kinetics. In addition, this model assumes that the binding reactions are equivalent and independent at all binding sites. It also assumes that the reaction rate is not limited by mass transport. Many interactions adhere to this model, in which the interaction is described by the equation shown below, where B represents the ligand and A is the analyte. The rate of complex formation is represented by the association constant (k_a, in the unit of $M^{-1}s^{-1}$) and the rate of complex decay is represented by the dissociation constant (k_d, in the unit of s^{-1}), as given by Equation 2.4 [4]:

$$A + B \underset{k_d}{\overset{k_a}{\Longleftrightarrow}} AB \tag{2.4}$$

In kinetic analysis, the equilibrium constant (K_D, in the unit of M) is calculated from the two kinetic constants, $K_D = k_d / k_a$. Relating the interaction state to the SPR sensorgram is accomplished by applying specific equations relevant to the different sensorgram phases, as illustrated in Figure 2.8 [4].

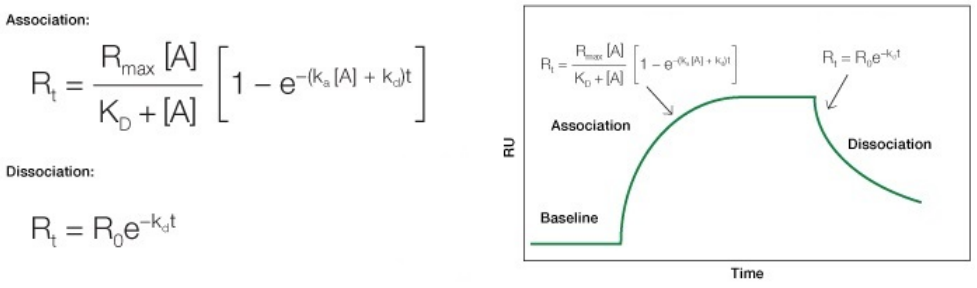

Figure 2.8: An idealized sensorgram with baseline, association, and dissociation phases. [4]

In the association phase, binding is measured while the analyte solution flows over the ligand surface. Analysis of the sensorgram in association phase allows determination of the rate of complex formation. There is an increase in response over time as the complex forms on the chip surface. The equations (2.5) to (2.9) outline the derivation of the association equation [4].

$$[A] = \text{constant} \tag{2.5}$$

$$[B] = [B]_{\max} - [AB] \tag{2.6}$$

$$\therefore \frac{d[AB]}{dt} = k_a[A][B] - k_d[AB] \tag{2.7}$$

$$\therefore \frac{dR_t}{dt} = k_a[A](R_{\max} - R_t) - k_d R_t \tag{2.8}$$

$$\therefore R_t = \frac{R_{\max}[A]}{K_D + [A]}\left[1 - e^{-(k_a[A]+k_d)t}\right] \tag{2.9}$$

In the dissociation phase, the analyte concentration in the flow is suddenly reduced to zero by the injection of running buffer. The rate of complex dissociation follows simple exponential decay, or first-order kinetics. Dissociation equation describes the time taken to reach a certain response level during the dissociation phase, as outlined in following equation, where R_0 is the signal level at the end of association [4].

$$\frac{d[AB]}{dt} = k_a[A]_t[B]_t - k_d[AB]_t \tag{2.10}$$

$$[A]_t = 0 \tag{2.11}$$

$$\therefore \frac{d[AB]}{dt} = -k_d[AB]_t \tag{2.12}$$

$$\therefore \frac{d[AB]}{dt} = -k_d R_t \tag{2.13}$$

$$\therefore R_t = R_0 e^{-k_d t} \tag{2.14}$$

2.3 Particle swarm optimization theory

PSO (Particle Swarm Optimization) was first designed by Eberhart and Kennedy [19] and used for optimization of continuous nonlinear functions. It is discovered through simulation of the social behavior of swarms. The swarm is composed of some volume-less particles with velocities, each of which represents a feasible solution in the solution space.

In PSO, all the particles are assigned fitness values, which are evaluated by the fitness function at each step of their movement and have velocities, which direct the flying paths of the particles. The particles fly through the problem space, with its velocities influenced by its momentum, cognitive awareness and social influence.

Initialized with a group of random particles (solutions), PSO searches for optima by updating their locations in the solution space in iterations. In every iteration, each particle is updated by following two "best" values. The first one is the best solution (fitness) it has achieved so far. The second one is the best value obtained by all particles in the population so far. The first value is called personal best and the seconde one is called global best. Both values are found, stored and updated in each iteration, and based on them, as well as the previous trajectory of the particle, the new particle velocity and position are calculated. If the stopping criteria is met, PSO program stops, otherwise it will move on to the next iteration.

In other evolutionary techniques such as genetic algorithms, chromosomes share information with each other by cross-over [20] and hence altering both solution chromosomes that conduct the crossover. As a comparison, in PSO, only the global best is shared with others to affect the next movement, which helps a quick convergence to the best solution in most cases.

2.4 SPR experiment design for this study

In this thesis, we first prepared the flow cell by planting the ligand on the chip following the array in Figure 2.9. And then let the analyte, Human Immunoglobulin G with different concentrations, flow through the flow cell. Plexera Array bio-sensor monitors and records the real-time interaction, with which we do ROI detection, SPR data extraction and kinetics constant estimation, etc,. Among all the spot, column 1, 2, 11, 12 are know as valid data for study of this thesis.

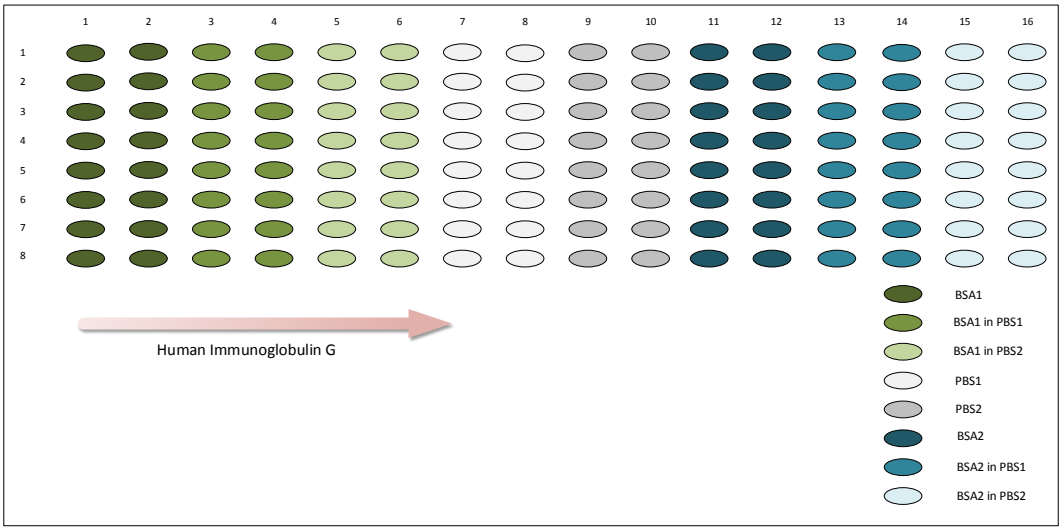

Figure 2.9: SPR experiment design for this study

CHAPTER 3: METHODOLOGY

To solve the current problems in SPR technology, we have designed a procedure, with a flow chart shown in Figure 3.1, to process the video and estimate the molecule binding parameters automatically.

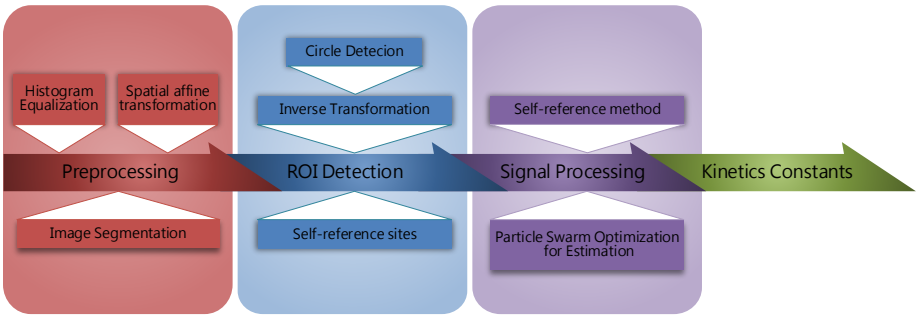

Figure 3.1: Procedure to process the video and estimate the molecule binding parameters automatically.

3.1 Pre-processing of the video data generated by the SPR machine

3.1.1 Histogram equalization (HE) and spatial affine transformation

A sample frame was presented earlier in Figure 2.6, which was cropped to obtain Figure 3.2 (a) to be processed later on. The SPR measurement video frame is usually dark as shown, and the contrast between the elliptical ROIs and the background is not significant, making the ROI detection a challenging task. Histogram Equalization (HE) is effective to achieve a wide dynamic range, and it is applied on Figure 3.2 (a) to yield Figure 3.2 (b). Suppose the probability of occurrence of intensity level r_k in a digital image is approximated by

$$p_r(r_k) = \frac{n_k}{MN}, \quad k = 0, 1, 2, \ldots, L-1 \tag{3.1}$$

where MN is the total number of pixels in the image, n_k is the number of pixels that have intensity r_k, and L is the number of possible intensity levels in the image. Then the histogram equalized intensity level is defined as

$$s_k = T(r_k) = (L-1)\sum_{j=0}^{k} p_r(r_j) = \frac{L-1}{MN}\sum_{j=0}^{k} n_j, \quad k = 0, 1, 2, \ldots, L-1 \tag{3.2}$$

Namely, the HE result image is obtained by mapping each pixel in the input image with intensity r_k into a corresponding pixel with level s_k in the output image.

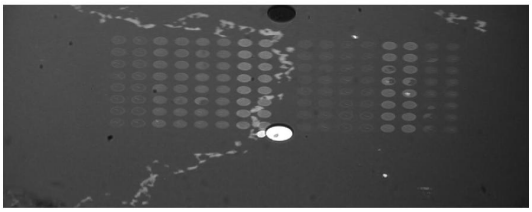

(a)

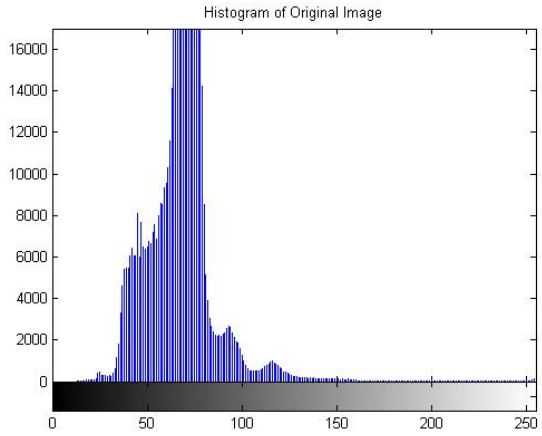

(b)

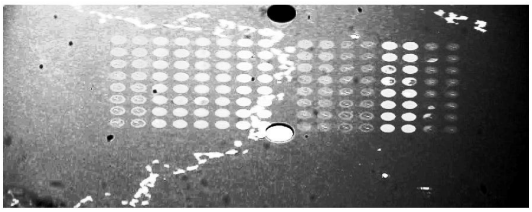

(c)

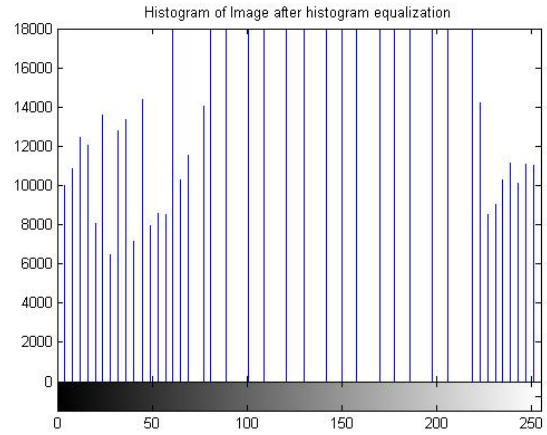

(d)

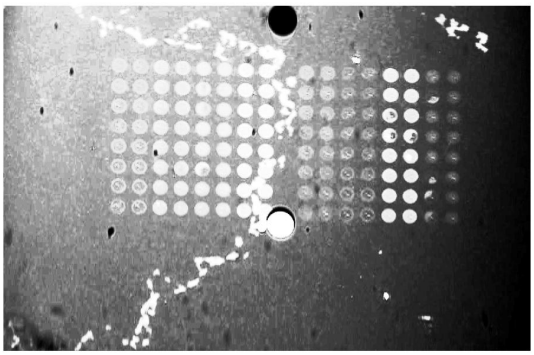

(e)

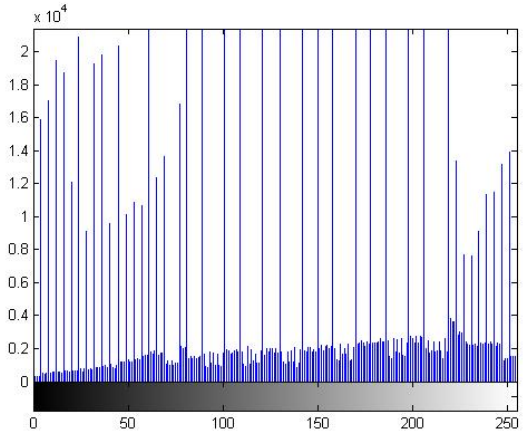

(f)

Figure 3.2: Histogram Equalization (a) original image; (b) histogram of original image; (c) HE result; (d) histogram of HE result; (e) affine transformed result; (f) histogram of transformed image

In SPR experiment, the size of the spots on the monitoring slides are mostly circles. However, due to image deformation, the spots are transformed to be ellipses. In order to facilitate the ROI detection, we apply an affine transformation, scaling, to be exact, on the image to recover the circular shape of the ROIs and then locate the circles. Once the ROIs are identified in the transformed domain, we apply an inverse affine transform to convert the pixel locations within the ROIs back to the original image to extract the exact measurements in the original image. The general affine transformation on the pixel locations is defined below,

$$\begin{bmatrix} x & y & 1 \end{bmatrix} = \begin{bmatrix} v & w & 1 \end{bmatrix} T = \begin{bmatrix} v & w & 1 \end{bmatrix} \begin{bmatrix} t_{11} & t_{12} & 0 \\ t_{21} & t_{22} & 0 \\ t_{31} & t_{32} & 1 \end{bmatrix} \tag{3.3}$$

where $[x, y]$ are the pixel coordinates in the output image, and $[v, w]$ are the ones in the input image. In our case to use scaling, we have used

$$T = \begin{bmatrix} 1 & 0 & 0 \\ 0 & 1.7 & 0 \\ 0 & 0 & 1 \end{bmatrix} \tag{3.4}$$

Figure 3.2 (e) is the scaled image of Figure 3.2 (c). The histograms for original cropped image, the HE image, and the scaled HE image are presented on the right hand side of each one of them, in Figure 3.2 (b), (d), and (f).

3.1.2 Image segmentation

Due to the differences in brightness in different sections, the thresholds in circle detection algorithm are hard to set globally. The frame image is segmented by the group of the ligands, which helps the circle detection later on.

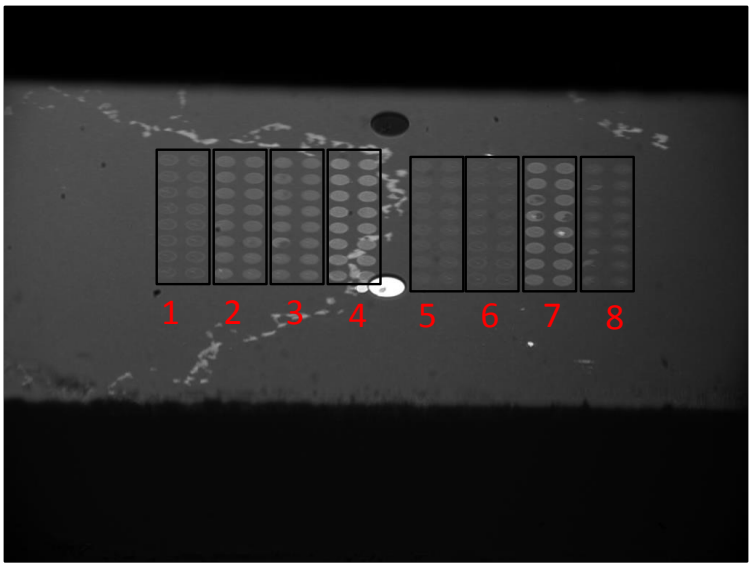

Figure 3.3: Frame image segmentation

3.2 Randomized hough transform for circle detection

ROI detection is essential to extract the SPR measurement of all the interaction sites between different ligands on the slide and the same analyte in the fluid. Currently users need to manually locate the ROIs, which takes a lot of time and labor, and the manually labeled ROIs may be inaccurate. In this thesis, we introduced randomized Hough transform (RHT) to detect the circular ROIs after our pre-processing.

The RHT requires several user-defined parameters to control the execution of the algorithm. These parameters are listed below.

- The validating threshold, v. The RHT accumulates votes through random sampling for a relatively small number of points in the circle parameter space. Once a circle parameter point gets at least v votes, the existence of the corresponding circle will be verified in a verification phase of the algorithm, in which the whole circle is constructed, and the exact number of edge points on the circle is counted. v is usually a small integer, with typical values of 2 or 3.

- The circle percentage threshold, p. The RHT does not expect to find a perfect circle.

Instead, if there are enough points on a candidate circle, the RHT reports it as a real circle. This is not only reasonable but also necessary, since the quantization error of the imaging, the failure of the edge detection process to extract weak or blurred object boundaries, and the existence of other random noises would distort or even damage parts of the circular pattern in the edge image. In the standard RHT, p is set for the number of points on a circle: if a candidate circle is verified to have n_c points on it, then the circle will be reported as a real circle if n_c is no less than p. A more reasonable form, however, is to define p as the ratio of n_c to the circumference of the candidate circle. For example, for a $p = 0.7$, a candidate circle is treated as a real one if 70 percent of the circle is present in the edge image.

- The maximum number of sampling, T. The RHT halts when no circle is detected in a run of T samplings. The RHT regards this case as an indication that there is no circles in the edge image.

The RHT are summarized in the following steps, with a flow chart in Figure 3.4.

Step 1: Initialize a counter variable $t = 0$, which stores the number of unsuccessful sampling in the current sampling run.

Step 2: Randomly select three edge points from the binary edge image. This selection step is called a sampling. If these points are collinear, they cannot define a circle, thus the sampling fails. Set $t = t + 1$. Otherwise a circle with a center at (x, y) and a radius of r can be computed. The circle parameters (x, y, r) form a point in the parameter space.

Step 3: Store the parameter set, (x, y, r), into a hash table and set a vote count for it. The count is initialized to 1. If the parameter set is already in the hash table, increase its vote count by 1.

Step 4: If the parameter set gets more votes than the validating threshold v, the corresponding candidate circle is verified, and the number of edge points on the candidate circle is counted and stored in n_c. Then the ratio $p_c = \frac{n_c}{2\pi r}$ is calculated. If p_c is greater than or

equal to the circle percentage threshold p, the candidate is recorded as a real circle in the edge image. The points on the identified circle are erased from the edge image, the hash table is emptied, and the counter variable t is reset to 0.

Step 5: If no circle is detected based on the three random edge points, set $t = t+1$, and resample the edge points from Step 2. Until t reaches the maximum sampling threshold T, the algorithm halts, and the detected circle parameters are reported.

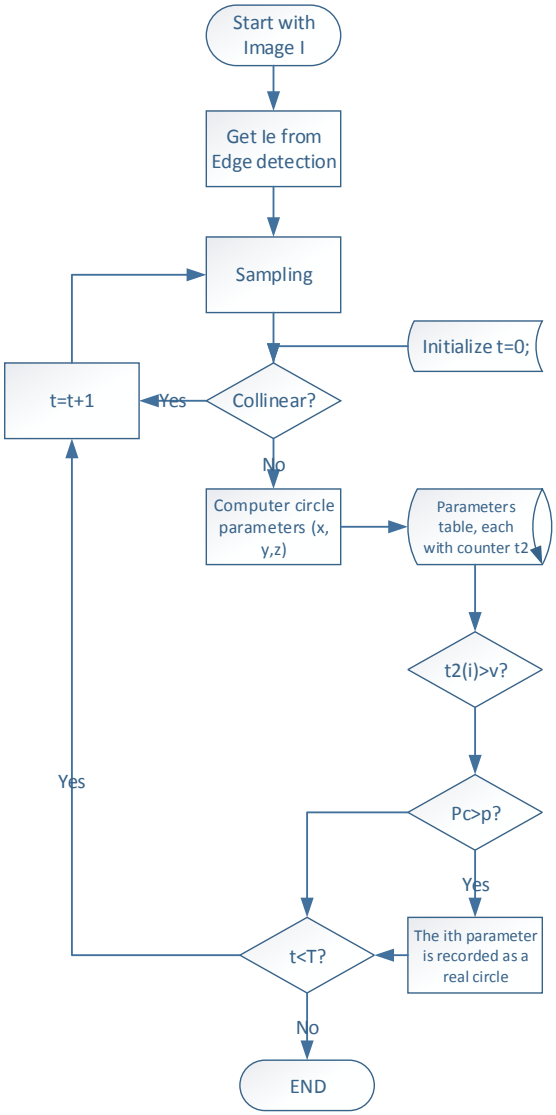

Figure 3.4: RHT procedures

Figure 3.5 is an example run of RHT to illustrate its steps. After circular ROI detection by RHT, the coordinates of the pixels within the ROI are inverse-transformed back onto the original image, with all the ROIs shown in Figure 3.6 (a). Figure 3.6 (b) is a zoomed-in version with the ROI boundary marked by a green ellipse and each pixel within the ROI marked by a yellow asterisk.

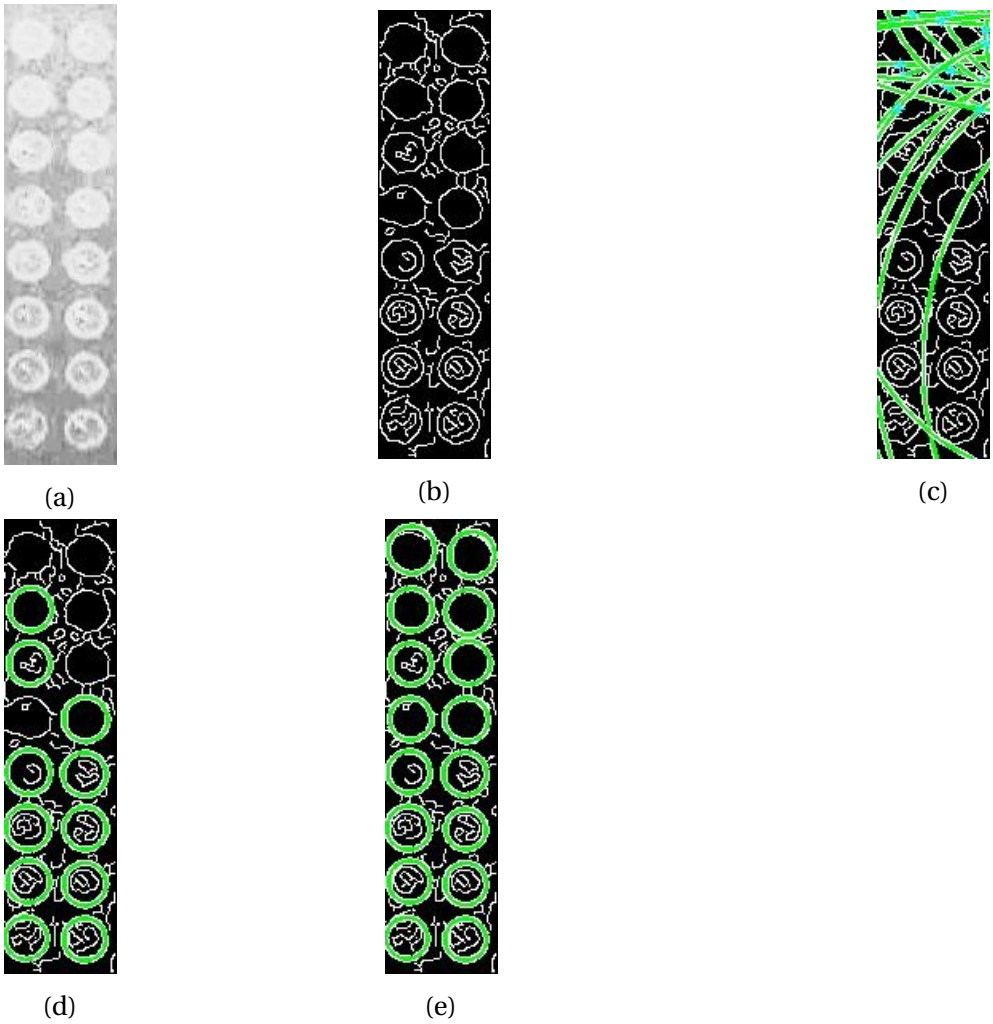

Figure 3.5: Example of RHT. (a) initial segment image; (b) edge detection result; (c) randomly pick 3 points and find the circle that passes through them if they are non-collinear; (d) converging to the region of interest; (e) RHT result

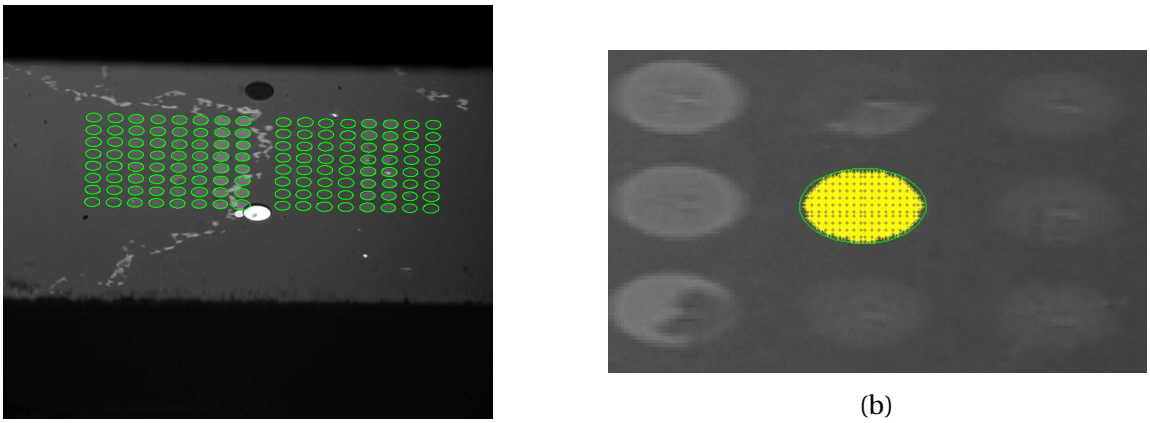

(a) (b)

Figure 3.6: ROI detection of images after pre-processing. (a) RHT result; (b) Pixels in one detected ROI for later data extraction

3.3 Self-referencing method

To eliminate long-term drift that affects the whole image during measurement, such as fluctuations of light source and ambient temperature, we adopted the self-referencing method. First, four satellite spots are selected for each ROI at the following locations.

$$\begin{bmatrix} x_1 & y_1 \\ x_2 & y_2 \\ x_3 & y_3 \\ x_4 & y_4 \end{bmatrix} = \begin{bmatrix} x_0 - r_0 & y_0 - r_0 \\ x_0 - r_0 & y_0 + r_0 \\ x_0 + r_0 & y_0 - r_0 \\ x_0 + r_0 & y_0 + r_0 \end{bmatrix} \tag{3.5}$$

where $[x_0,\ y_0,\ r_0]$ are the center coordinates and radius of the ROI, $[x_j,\ y_j]$ with $j = 1,\ldots,4$, are the four satellite sites around this ROI. Based on whether the satellite sites are compromised by drastic noise, such as the bubble, or not, we define P_i to be either 1 or 0 to indicate the choice to include this satellite spot in the satellite set or not.

$$P_i = \begin{cases} 0 & \text{if } \sigma_i / \sigma_{i'} \geq \tau \\ 1 & \text{otherwise} \end{cases} \tag{3.6}$$

where σ_i is the variance of all satellites; $\sigma_{i'}$ is the variance of other satellites, and τ is a threshold. We use the average gray level values of the pixels in the satellite set as the reference to obtain a normalized SPR intensity curve.

$$I_{\text{normalized}} = I_{\text{signal}} - \bar{I}_{\text{satellites}} \tag{3.7}$$

where $I_{\text{normalized}}$ and I_{signal} denote the normalized signal and the original intensity, respectively, and $\bar{I}_{\text{satellites}}$ is given by

$$\bar{I}_{\text{satellites}} = \frac{\Sigma I_{s_i} \times P_i}{\Sigma P_i} \tag{3.8}$$

where ΣI_{s_i} is the light intensity of ith satellite in a satellite set. Figure 3.7 shows the self-referencing result of spot 1.

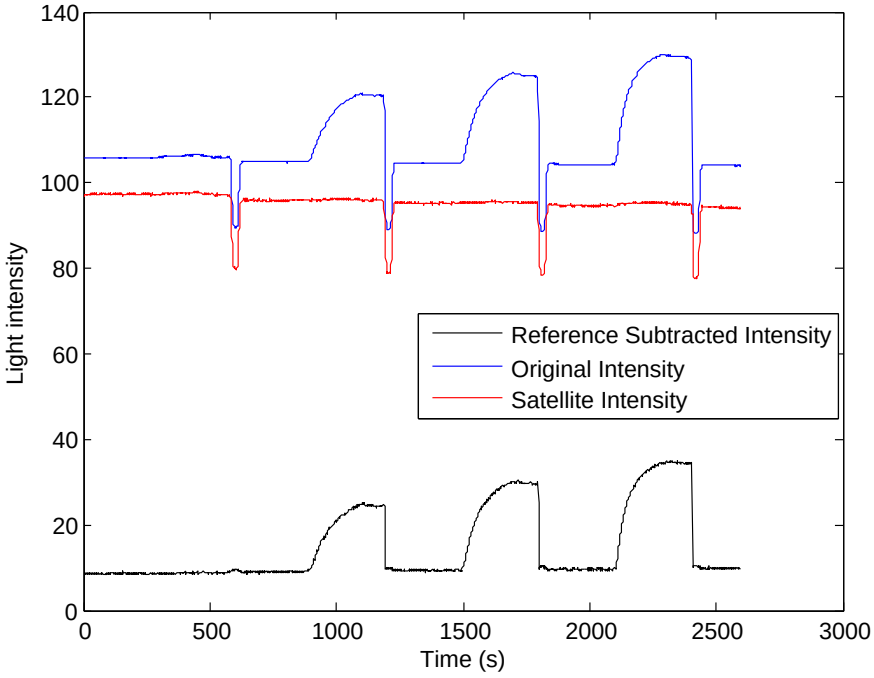

Figure 3.7: Self-referencing result of spot 1

3.4 Application of particle swarm optimization

PSO starts by having a population of particles initialized with random positions marked by vector $\vec{x_i}$ and random velocities $\vec{v_i}$. The population of such particles is called a "swarm". Each particle P stores two state variables viz., its current position $\overrightarrow{x(t)}$ and its current velocity $\overrightarrow{v(t)}$. It is also equipped with a small memory comprising its previous best position $\overrightarrow{p(t)}$, i.e., the personal best experience and the best $\overrightarrow{p(t)}$ of all P's, $\overrightarrow{g(t)}$, i.e., the best position found so far in the neighborhood of the particle. The following parameters are used in the PSO algorithm:

- an inertia weight factor ω;

- two uniformly distributed random numbers, $0 \leq \varphi_1, \varphi_2 \leq 2$ on the velocity update formula;
- two constant multiplier terms C_1 and C_2, which are the weights of "self cognitive awareness" and "social influence", respectively.

Initially, $\overrightarrow{p(t)}$ and $\overrightarrow{g(t)}$ are set as $\overrightarrow{p(t)} = \overrightarrow{g(t)} = \overrightarrow{x(0)}$ for all particles. Once the particles are all initialized, iterations begin, where the positions and velocities of all the particles are altered by the following recursive equations (3.9) and (3.10). The equations are presented for the dth dimension of the position and velocity of the ith particle.

$$V_{id}(t+1) = \omega v_{id}(t) + C_1\varphi_1(p_{id}(t) - x_{id}(t)) + C_2\varphi_2(g_{id}(t) - x_{id}(t)) \tag{3.9}$$

$$x_{id}(t+1) = x_{id}(t) + v_{id}(t+1) \tag{3.10}$$

The first term in the velocity updating formula represents the inertia of the particle. Since the coefficient C_1 has a contribution towards the self-exploration (or experience) of a particle, we regard it as the particle' self-confidence. On the other hand, the coefficient C_2 weights the contribution towards motion of the particles in global best's direction, which takes into account the motion of all the particles in the preceding iterations. After calculating the velocities and positions of the particles at the next time step $t+1$, the first iteration of the algorithm is completed. Typically, this process is iterated for a certain number of time steps, or until some acceptable solution has been found, or until an upper limit of CPU usage has been reached. The algorithm can be summarized in the following pseudo code:

Algorithm 1 PSO algorithm

Require: Randomly initialized position and velocity of the particles: $\overrightarrow{X_i}(0)$ and $\overrightarrow{V_i}(0)$
1: **while** terminating condition is not reached **do**
2: **for** $i = 1$ to number of particles **do**
3: Evaluate the fitness$\leftarrow f(\overrightarrow{X_i})$
4: Update $\overrightarrow{p_i}$ and $\overrightarrow{g_i}$
5: Adapt velocity of the particle using equation 3.9 and 3.10
6: Update the position of the particle;
7: **return**

To apply PSO algorithm in SPR kinetic constant fitting, we first defined the solution space as the possible range of the k_a, k_d, and R_{max}, in which the initial positions of particles were initialized. Based on the mean square error (MSE) metric between the parametric curve using our estimated kinetic constants and the sensorgram data as the fitness function, the fitness for each iteration was computed for next set of k_a, k_d, and R_{max}. Eventually, the iteration stopped when it reached the stopping criteria based on total iteration number and the convergence of MSE value.

CHAPTER 4: RESULTS

4.1 SPR experiment and the objectives in this study

Figure 4.1 shows the SPR experiment in our study. Eight sets of ligands were planted on the chip prior to injecting the analyte through the surface. Each set of ligand in the ligands Table 4.1 takes an array of 8 rows by 2 columns on the surface. The analyte is the Human Immunoglobulin G (HIgG) with different concentration according to Table 4.2. The ROI spots are labeled by numerical indices in Figure 4.1, and the analysis results on these ROIs will be referred to by these indices hereafter.

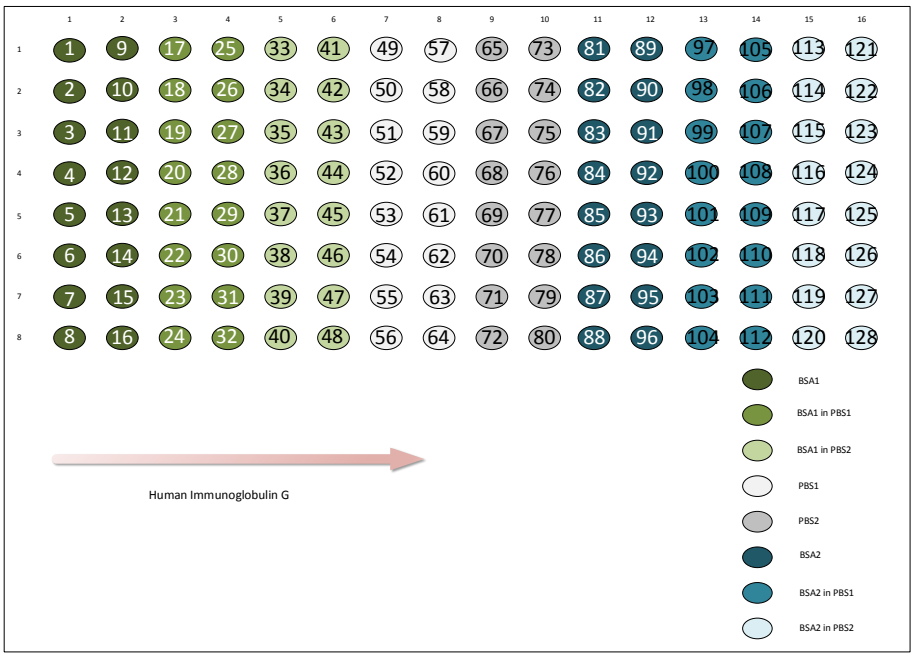

Figure 4.1: SPR experiment illustration

Among all the ligands, BSA1 and BSA2 (spot 1-16 and spot 81-96) are active ligands which will interact with the analyte and the rests are the reference for observation. In addition, spot 88 and spot 96 are affected by bubble noise during the experiment, hence, their data will be processed individually. Figure 4.2 to 4.4 illustrate the sensorgram example for interested spot, reference spot and spot affected by air bubble.

Ligands List	
1-16	Bovine Serum Albumin (BSA) 1
17-32	BSA 1 in PBS 1
33-40	BSA 1 in PBS 2
41-56	Phosphate-buffered Saline (PBS) 1
57-72	Phosphate-buffered Saline (PBS) 2
73-88	Bovine Serum Albumin (BSA) 2
89-112	BSA 1 in PBS 1
113-128	BSA 2 in PBS 2

Table 4.1: Ligands List

Analyte List	
1	HIgG, 1.67×10^{-7}(M)
2	HIgG, 3.33×10^{-7}(M)
3	HIgG, 6.67×10^{-7}(M)

Table 4.2: Analyte List

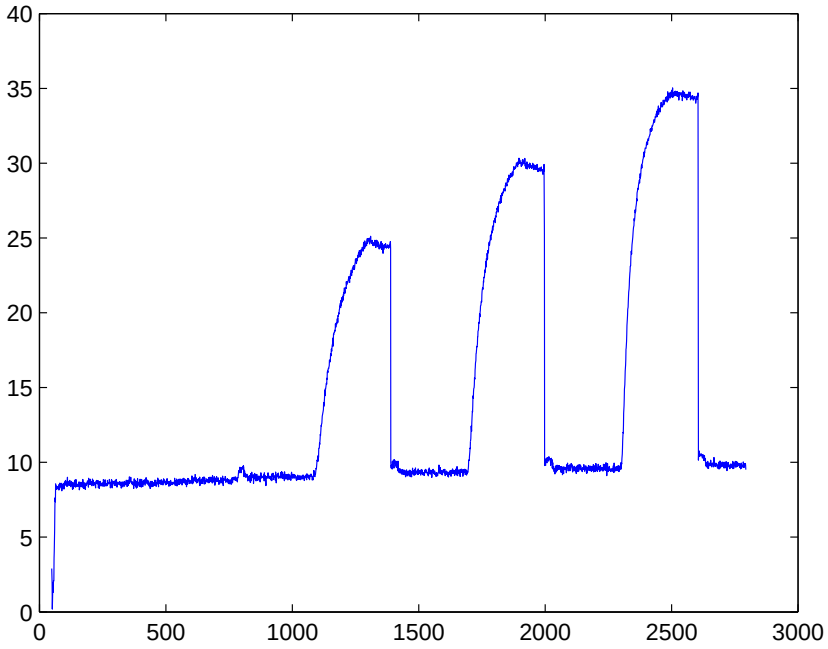

Figure 4.2: Example of active spot

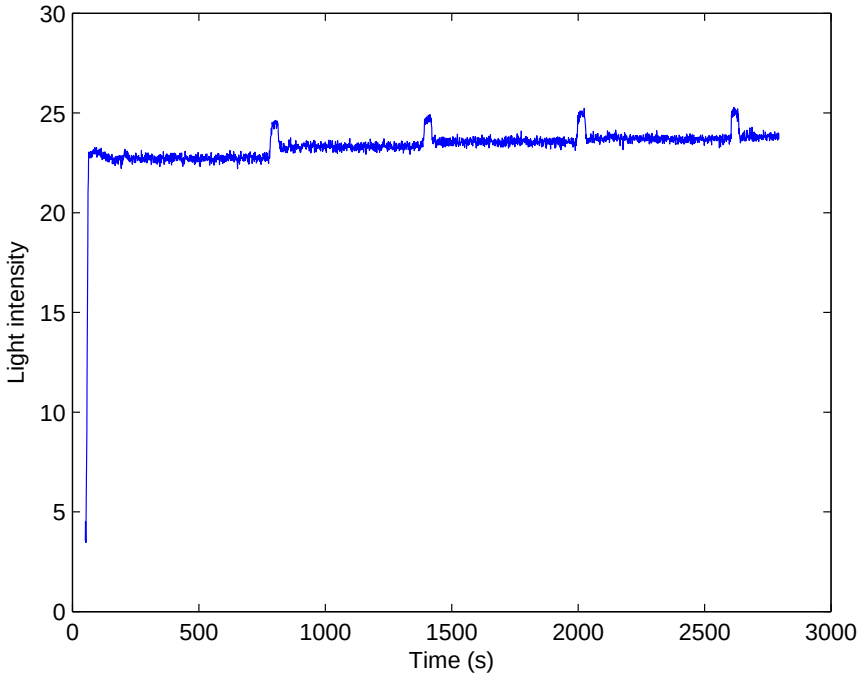

Figure 4.3: Example of reference spot

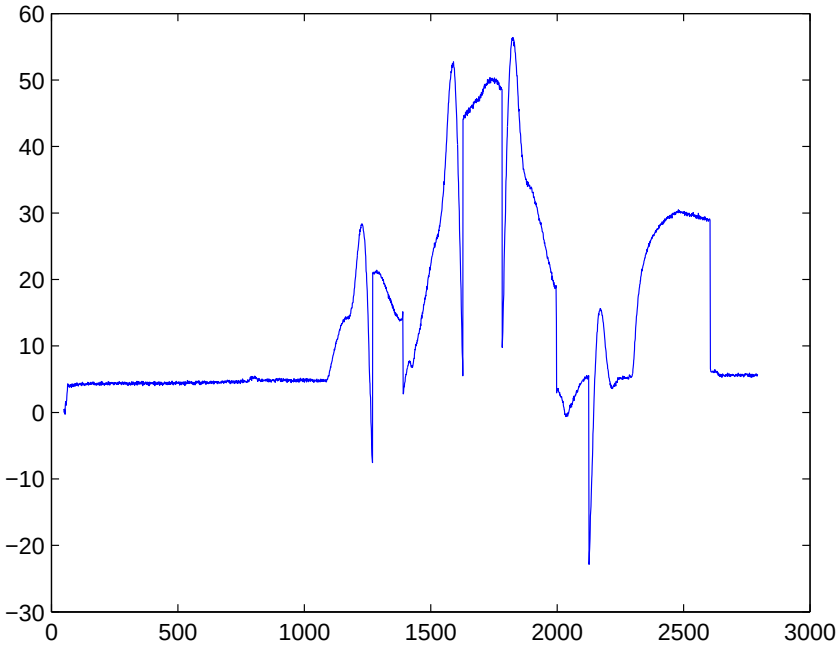

Figure 4.4: Example of active spot affected by air bubble

The objectives of our SPR experiments are:

1. To detect ROIs automatically;

2. To estimate the kinetics constants k_a and k_d for active spots 1-16, 81-87, and 89-96.

4.2 ROI auto-detection result

Figure 4.5 (a) shows the ROI detection result with the satellites. Figure 4.5 (b) is an example showing the pixel inside the detected ROI, which are used for intensity data extraction to generate the SPR sensorgram. As can be observed, we successfully captured all the ROIs on the surface. Furthermore, the pixel detection inside each ROI is precise and can promise the accuracy of the following estimation work.

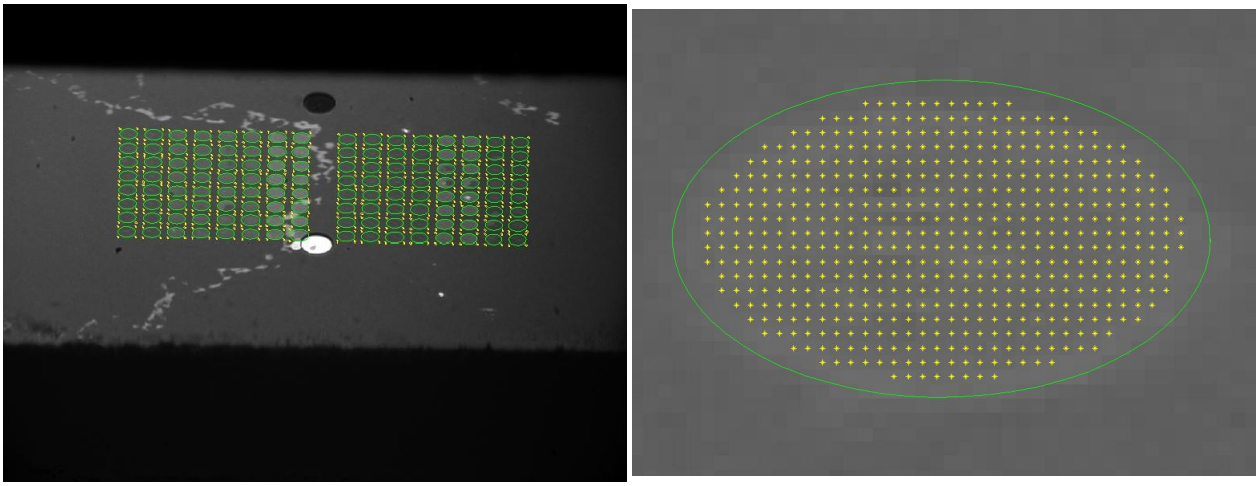

(a) Detection of ROI and its satellites

(b) Detected Pixels in Spot 1

Figure 4.5: ROI detection result

4.3 Kinetic constant estimation and fitting results for spot 1

In this section, we will first show the kinetic constant fitting for active spots and take spot 1 as example. Then the fitting for active spot affected by air bubble is show in section 4.4. In the end a summary of the MSE comparison between LM fitting and PSO fitting for all the active spots is given in table 4.3.

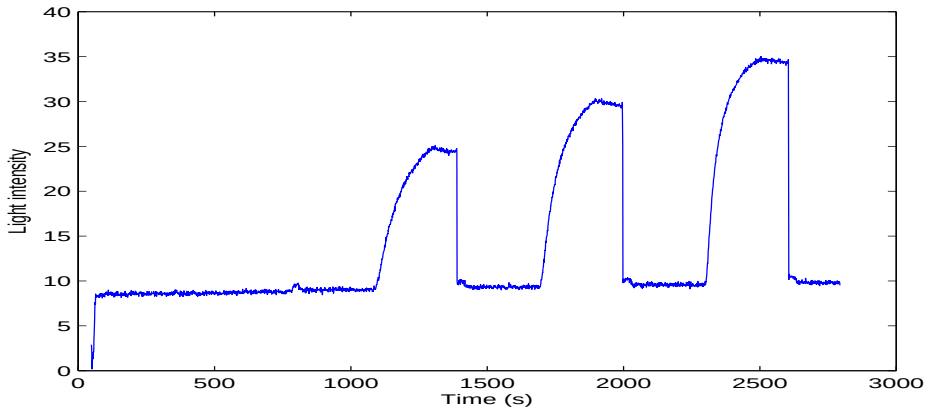

Figure 4.6: SPR curve of Spot 1

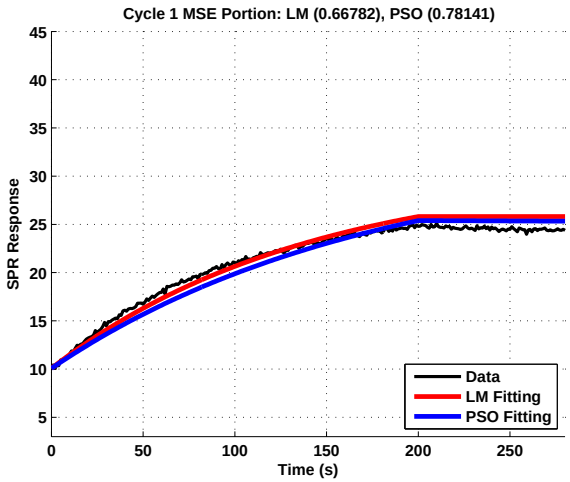

(a)

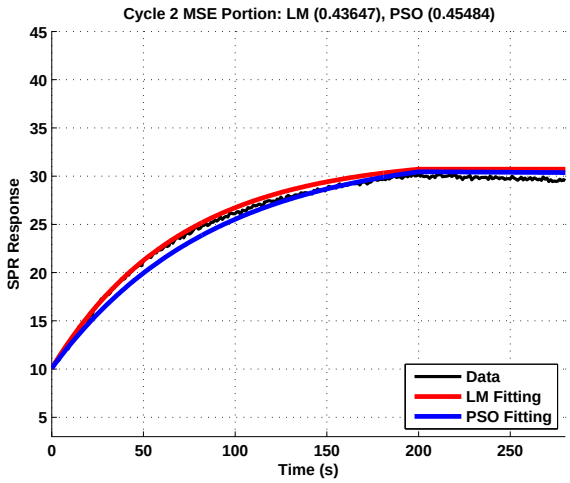

(b)

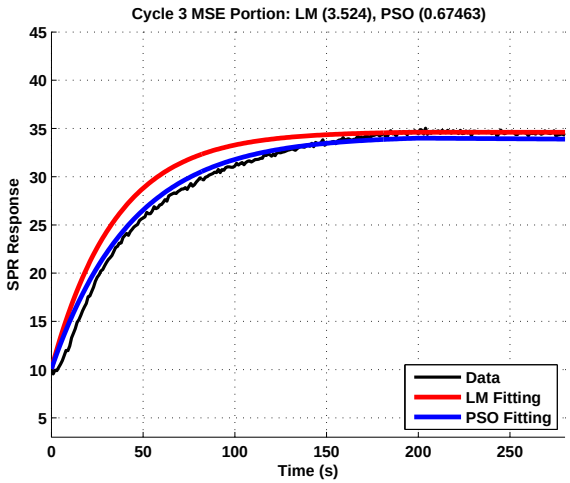

(c)

	$k_a(s^{-1}M^{-1})$	$k_d(s^{-1})$	MSE
LM	4.2900×10^4	0	4.6283
PSO best	3.4211×10^4	5.1457×10^{-5}	1.9109

The ranges of parameters obtained by PSO in 100 Monte-Carlo runs are below:

$$3.4211 \times 10^4 < k_a < 3.4469 \times 10^4$$
$$0 < k_d < 5.1457 \times 10^{-5}$$
$$1.9109 < \text{MSE} < 1.9455$$

Figure 4.7: PSO curve fitting result for spot 1

Figure 4.7 (a) to 4.7 (c) shows the LM and PSO curve fitting results for three cycles of spot 1. Since the three cycles share the same kinetic constants k_a and k_d, the fitting MSE is evaluated as the summation of MSE across all three cycles. Using either LM and PSO, the order of estimated magnitude of ka or kd is similar.

PSO is a random searching algorithm and hence 100 Monte Carlo simulation runs were carried out. The range of the estimated parameters, as well as MSE values, are reported. It is observed that PSO consistently yields a smaller MSE value than the LM algorithm. Based on the Monte Carlo simulation results of our PSO algorithm, we can deduce that the solution space of this project is highly nonlinear with many local minimas, because the best result with the minimum MSE is not always achieved in the 100 Monte Carlo simulations, although the other solutions are also very good, and much better than the LM estimated parameters. Because of the nature of this problem, the LM algorithm, which is a gradient based approach, is restricted by the local minimas, and hence not being able to achieve a comparable result as PSO.

4.4 Kinetic constant estimation and fitting results for tainted data

ROI spots 88 and 96 are affected by air bubble in the flow cell, as shown in Figure 4.8. As a result, the sensorgrams of spots 88 and 96 are not always valid in the 3 cycles, as illustrated in Figure 4.9 and 4.11. To deal with the spots affected by bubble noise, we only consider the valid cycles in the PSO analysis. Figure 4.10 and 4.12 show the PSO fitting results using the valid cycles of spots 88 and 96.

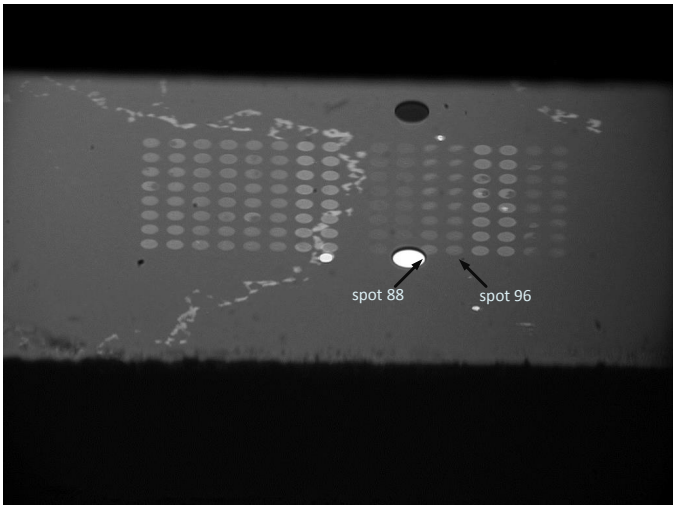

(a)

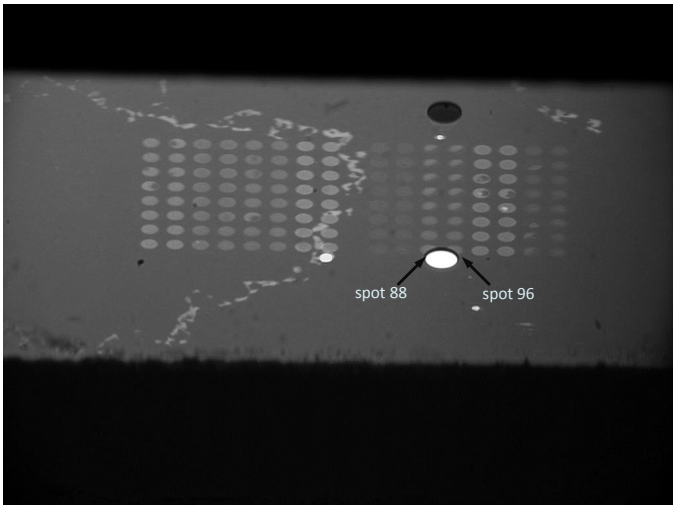

(b)

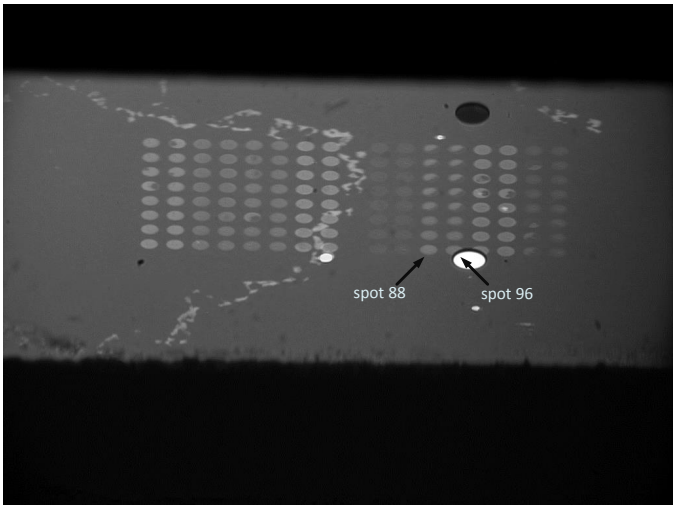

(c)

Figure 4.8: (a) Air bubble starts to affect spot 88 (at 1346 second); (b) Air bubble moves from spot 88 towards spot 96 (at 1947 second); (c) Air bubble leaves spot 96 (at 2466 second).

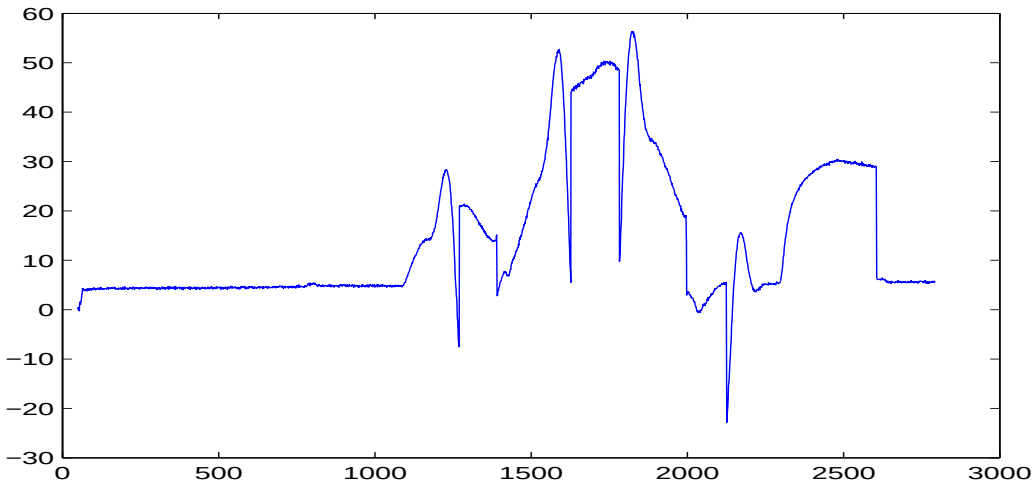

Figure 4.9: Sensorgram of spot 88

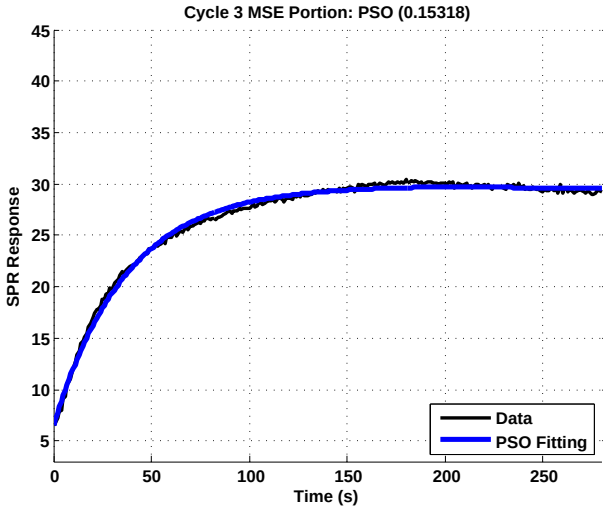

(c)

	$k_a(s^{-1}M^{-1})$	$k_d(s^{-1})$	MSE
PSO best	4.0072×10^4	7.7162×10^{-5}	0.1532

The ranges of parameters obtained by PSO in 100 Monte-Carlo runs are below:

$$3.9957 \times 10^4 < \ k_a \ < 4.0371 \times 10^4$$
$$0 < \ k_d \ < 7.7162 \times 10^{-5}$$
$$0.1532 < \text{MSE} < 0.1613$$

Figure 4.10: PSO curve fitting result for cycle 3, the only valid cycle, of spot 88

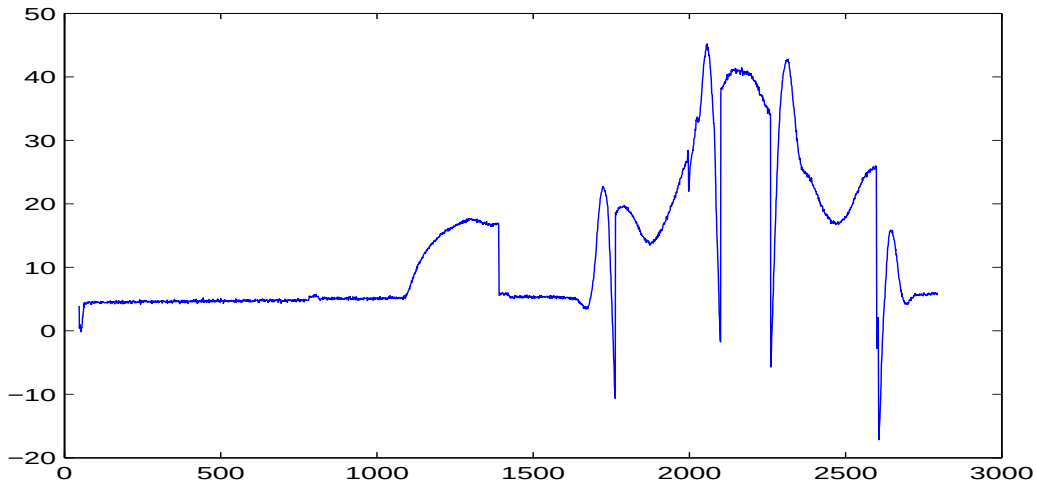

Figure 4.11: Sensorgram of spot 96

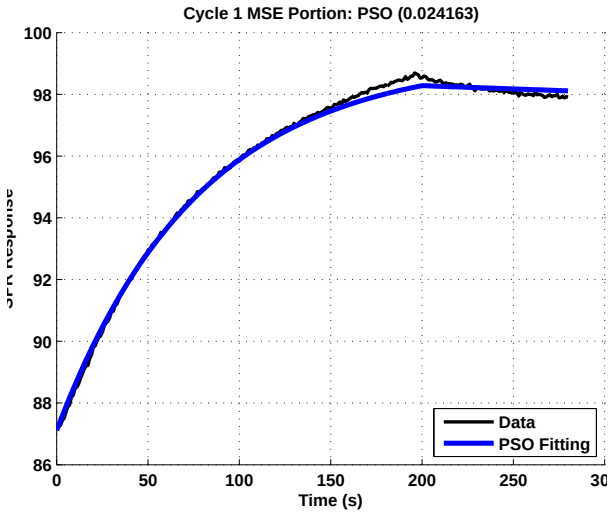

(c)

	$k_a(s^{-1}M^{-1})$	$k_d(s^{-1})$	MSE
PSO best	7.6498×10^4	19.1692×10^{-5}	0.0501

The ranges of parameters obtained by PSO in 100 Monte-Carlo runs are below:

$$7.6498 \times 10^4 < k_a < 7.9841 \times 10^4$$
$$0 < k_d < 19.1692 \times 10^{-5}$$
$$0.0501 < \text{MSE} < 0.0639$$

Figure 4.12: PSO curve fitting result for cycle 1, the only valid cycle, of spot 96

4.5 MSE comparison between LM fitting and PSO fitting for all the spots

Besides ROI spot 1 that was analyzed in details in section 4.3, we have analyzed all the other active ROI spots, with their detailed results presented in the Appendix. As a summary, the estimated parameters as well as the MSE comparison between LM and PSO are presented in Table 4.3.

	LM			PSO		
Spot	k_a	k_d	MSE	k_a	k_d	MSE
1	4.2900×10^4	0	4.6283	3.4211×10^4	5.1457×10^{-5}	1.9109
2	4.1600×10^4	0	5.1734	3.2236×10^4	7.8155×10^{-5}	1.8845
3	4.7400×10^4	0	8.5518	3.3677×10^4	6.8332×10^{-5}	2.3899
4	4.8800×10^4	0	8.4644	3.5122×10^4	7.7952×10^{-5}	2.9143
5	4.4100×10^4	0	10.6897	3.0690×10^4	4.9807×10^{-5}	2.8205
6	4.5200×10^4	0	11.2869	3.1773×10^4	5.4298×10^{-5}	3.6504
7	4.9600×10^4	0	18.5110	3.2335×10^4	6.2582×10^{-5}	4.8308
8	4.7200×10^4	0	18.2665	3.1914×10^4	6.6521×10^{-5}	5.8437
9	3.8200×10^4	0	2.1794	3.9394×10^4	7.5838×10^{-5}	1.8181
10	4.0000×10^4	0	4.0172	3.3308×10^4	6.5380×10^{-5}	1.5995
11	4.0500×10^4	0	4.0637	3.3085×10^4	8.3508×10^{-5}	1.7088
12	4.2400×10^4	0	5.4863	3.2648×10^4	7.3786×10^{-5}	1.8776
13	4.3200×10^4	0	6.6458	3.2797×10^4	5.8035×10^{-5}	2.1497
14	4.4200×10^4	0	8.9908	3.2292×10^4	5.2531×10^{-5}	2.6341
15	4.5300×10^4	0	10.7705	3.3166×10^4	6.7892×10^{-5}	3.4486
16	4.5500×10^4	0	11.8910	3.2913×10^4	6.6027×10^{-5}	3.9762
81	3.9300×10^4	0	1.2178	5.3109×10^4	8.3513×10^{-5}	0.5733
82	4.0000×10^4	0	0.9118	4.8966×10^4	8.5889×10^{-5}	0.5117
83	3.8100×10^4	0	1.2309	4.8692×10^4	7.1950×10^{-5}	0.6149
84	3.7800×10^4	0	1.0766	4.7274×10^4	7.4515×10^{-5}	0.6058
85	3.6900×10^4	0	1.2125	4.6796×10^4	6.5092×10^{-5}	0.6204
86	3.3100×10^4	0	1.5157	4.3628×10^4	7.0387×10^{-5}	0.6619
87	3.6300×10^4	0	1.6559	4.4077×10^4	9.1886×10^{-5}	0.8707
89	3.6100×10^4	0	1.1302	5.0284×10^4	6.0331×10^{-5}	0.4134
90	3.8100×10^4	0	0.8470	4.9719×10^4	6.3409×10^{-5}	0.4091
91	3.8000×10^4	0	1.0342	4.8193×10^4	8.2558×10^{-5}	0.4951
92	3.7600×10^4	0	1.1500	4.8336×10^4	5.5014×10^{-5}	0.5566
93	3.6500×10^4	0	0.9602	4.5642×10^4	5.8846×10^{-5}	0.4696
94	3.3700×10^4	0	1.0884	4.4378×10^4	6.7123×10^{-5}	0.4608
95	3.4400×10^4	0	1.2054	4.2790×10^4	7.9544×10^{-5}	0.5909

Table 4.3: Parameter estimation and MSE comparison between LM and PSO fitting on all the active ROI spots

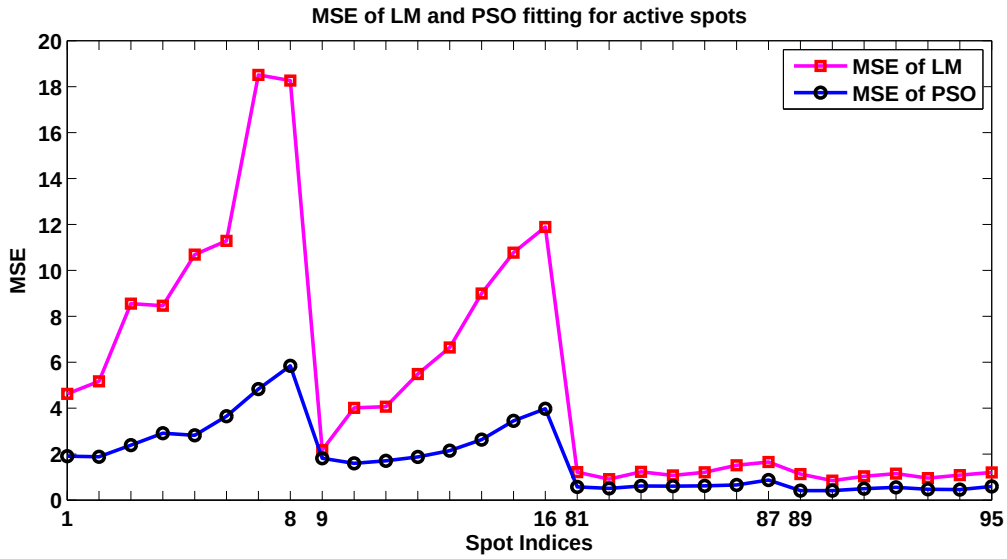

Figure 4.13: MSE comparison between LM and PSO fitting on all the active ROI spots

Table 4.3 lists the estimated kinetic constants using both LM and PSO, as well as the MSE comparison between LM and PSO fitting on all the active ROI spots. To make the MSE comparison easy to observe, we also plotted the MSE values for all the active ROI spots in Figure 4.13. The PSO fitting algorithm shows better accuracy than the commercially used LM algorithm consistently for all the active ROI spots.

CHAPTER 5: CONCLUSION AND FUTURE WORK

This thesis studied the Surface Plasmon Resonance (SPR) measurement processing procedures and achieved enhancement in two aspects: efficiency of the Region of Interest (ROI) assignment and the accuracy of SPR data fitting.

The ROI detection was achieved using image processing techniques such as image histogram equalization, edge detection, and randomized hough transformation. Applying the combination of these techniques successfully captured the pixel inside the ROIs for data extraction. Self-referencing method was used to mitigate the affect of long term baseline shift and other noises, prior to the utilization of particle swarm optimization for estimating the molecule binding parameters. Figure 4.5 (a) illustrates the automatic and convenient ROIs detection. Our fitting results in Chapter 4 and Appendix demonstrate a better fitting accuracy using the PSO algorithm than using the LM algorithm, yielding a smaller MSE value consistently. Out of 100 Monte Carlo simulation runs, the MSE decrease from the commercially used LM algorithm to PSO algorithm is at least 16.58%, up to as big as 73.9%.

Future work includes: *(1)* Refine each method to further improve the detection efficiency for better performance in real-time applications. *(2)* Collect real-time data from more experiments to verify the robustness of the proposed detection and fitting methods.

BIBLIOGRAPHY

[1] E. Pereira, L. Oliveira, M. Morais, A. Lima, and H. Neff, "Improved data extraction algorithm for biosensors utilizing surface plasmon resonance sensing," in *Instrumentation and Measurement Technology Conference (I2MTC) Proceedings, 2014 IEEE International*, May 2014, pp. 1105–1110.

[2] Y. Tang and X. Zeng, "Surface plasmon resonance: An introduction to a surface spectroscopy technique," *journal of chemical education*, vol. 87, no. 7, pp. 742–746, April 2010.

[3] Z. Huang and X. Wang, "Noise reduction in the surface plasmon resonance array sensor," *Optical Engineering*, vol. 52, no. 4, pp. 044 403–044 403, 2013.

[4] R. Luo, *Protein interaction analysis*, 1st ed. USA: Bio-Rad Laboratories, Inc., 2013.

[5] M. Malmqvist and R. Karlsson, "Biomolecular interaction analysis: affinity biosensor technologies for functional analysis of proteins," in *Current Opinion in Chemical Biology*, February 2002, pp. 378–383.

[6] R. Copeland, D. Pompliano, and T. Meek., "Drug-target residence time and its implications for lead optimization," in *Nat Rev Drug Discov*, September 2002, pp. 730–739.

[7] R. Glaser. and G. Hausdorf, "Binding kinetics of an antibody against HIV p24 core protein measured with real-time biomolecular interaction analysis suggest a slow conformational change in antigen p24," in *Journal of Immunological Methods*, September 1996, pp. 1–14.

[8] S. Salapaka and M. Salapaka, "Scanning probe microscopy," *Control Systems, IEEE*, vol. 28, no. 2, pp. 65–83, April 2008.

[9] B. Redlich, "Infrared spectroscopy of (bio)molecules in the gas phase using the free-electron-laser 'felix'," in *Infrared and Millimeter Waves and 13th International Conference on Terahertz Electronics, 2005. IRMMW-THz 2005. The Joint 30th International Conference on*, vol. 1, Sept 2005, pp. 307–308 vol. 1.

[10] Y. Kolesnikov, M. Kabakova, A. Novikov, E. Thiel, and V. Zemskii, "Spectral gas sensitivity of immobilized ph-indicator molecules," in *Lasers and Electro-Optics Europe, 2003 Conference on*, June 2003, p. 498.

[11] B. Liedberg, C. Nylander, and I. Lunström, "Zeitschrift für physik," *Sens. Actuators*, vol. 4, pp. 299–340, 1983.

[12] J. Homola, "Surface plasmon resonance sensors for detection of chemical and biological species," *Chem. Rev.*, vol. 108, no. 2, pp. 462–493, 2008.

[13] M. Piliarik, L.Parova, and J.Homola, "High-throughput SPR sensor for food safety," *Biosens. Bioelectron*, vol. 24, no. 5, pp. 1399–1404, 2009.

[14] D. Shankaran, K.V.Gobi, and N.Miura, "Recent advancements in surface plasmon resonance immunosensors for detection of small molecules of biomedical, food and environmental interest," *Sens. Actuat. B. Chem*, vol. 121, no. 1, pp. 158–177, 2007.

[15] K. Erika, *Handbook of Biosensors and Electronic Noises: Medicine, Food, and the Environment*, 1st ed. USA: CRC Press, 1996.

[16] R. Nejm, M. Hussein, and A. Ayesh, "A study of the surface plasmon enhancement using ARC on thin film si solar cell performance," in *High Capacity Optical Networks and Enabling Technologies (HONET-CNS), 2013 10th International Conference on*, Dec 2013, pp. 51–55.

[17] Y. Xu, X. Ma, and H. Zhao, "A novel design of distributed surface plasmon sensors based on nanoparticles composite layers," in *Biophotonics, Nanophotonics and Metamaterials, 2006. Metamaterials 2006. International Symposium on*, Oct 2006, pp. 310–313.

[18] W. Yuan, H. Ho, C. Wong, S. Wu, Y. Suen, S. Kong, and C. Lin, "Sensitivity enhancement of phase-sensitive surface plasmon resonance biosensor using multi-pass interferometry," in *Biophotonics, Nanophotonics and Metamaterials, 2006. Metamaterials 2006. International Symposium on*, Oct 2006, pp. 202–205.

[19] R. Eberhart and J. Kennedy, "A new optimizer using particle swarm theory," in *Micro Machine and Human Science, 1995. MHS '95., Proceedings of the Sixth International Symposium on*, Oct 1995, pp. 39–43.

[20] K. Deb, A. Pratap, S. Agarwal, and T. Meyarivan, "A fast and elitist multiobjective genetic algorithm: NSGA-ii," *Evolutionary Computation, IEEE Transactions on*, vol. 6, no. 2, pp. 182–197, Apr 2002.

Appendices

Appendix A: ANALYSIS ON ALL THE OTHER ACTIVE SPOTS

The molecule binding parameter fitting results for spot 1 are presented in section 4, and the rest of the ROIs, extracted from the video frame images, are presented in this appendix from the next page. On each page, there are two figures: the first one is the overall gray level value along time, and the three cycles when the analyte was injected at three different molarities were segmented and used for data fitting together to yield the k_a, k_d parameters. The ligants have not changed, and the ingredient of the anlayte does not change except its molarity, so the k_a, k_d parameters should be identical at the three cycles. Since we strive to fit one set of k_a, k_d parameters for each spot's sensorgram, the fitting may appear more fit in one cycle than in other cycles. The second figure on each page illustrates the fitting results using the parameters and the model to derive the fitted result (red being LM fitting result, and blue being PSO result). PSO is randomly initialized, and hence the derived parameters and MSE may vary slightly, but as observed in the variation range in 100 Monte-Carlo runs, k_a and MSE are quite stable, while k_d is close to 0, since the dissociation appears to be nearly flat, slower than the time between analyte cleaning sessions.

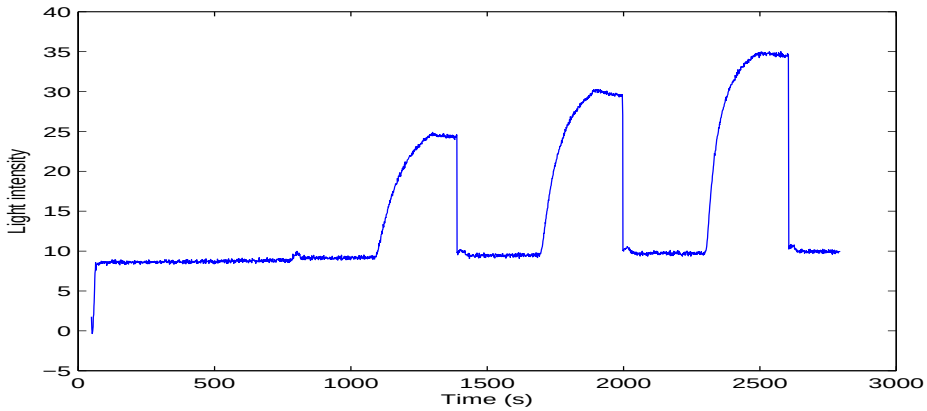

Figure A.1: SPR curve of Spot 2

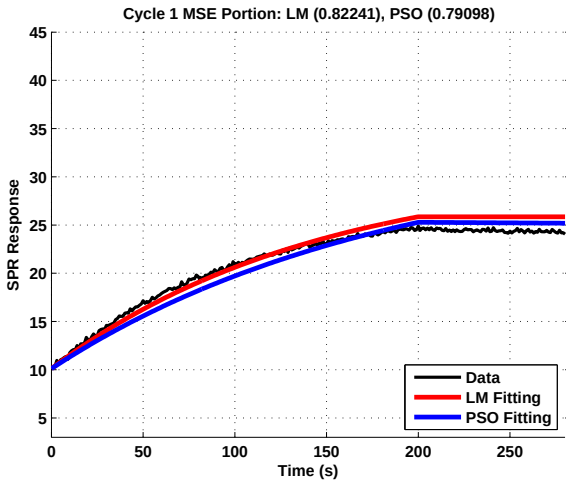

(a)

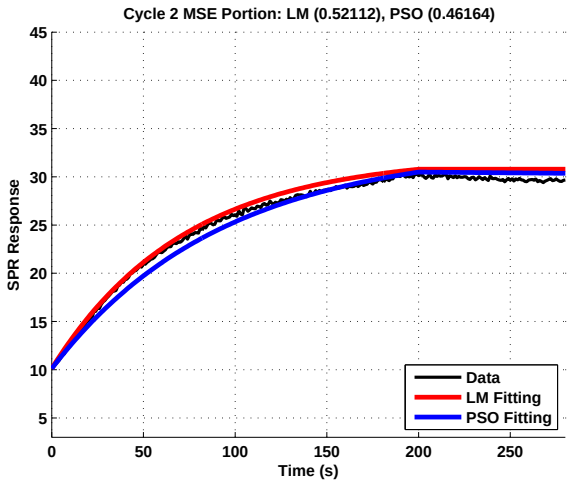

(b)

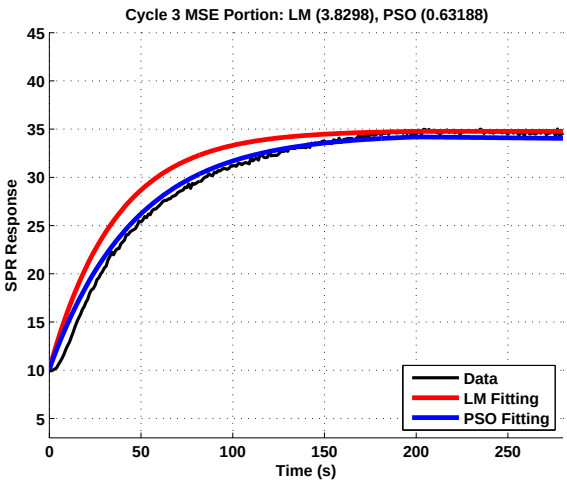

(c)

	$k_a(s^{-1}M^{-1})$	$k_d(s^{-1})$	MSE
LM	4.1600×10^4	0	5.1734
PSO best	3.2236×10^4	7.8155×10^{-5}	1.8845

The ranges of parameters obtained by PSO in 100 Monte-Carlo runs are below:

$$2.6990 \times 10^4 < k_a < 3.2698 \times 10^4$$
$$0 < k_d < 7.8155 \times 10^{-5}$$
$$1.8845 < \text{MSE} < 2.5864$$

Figure A.2: PSO curve fitting result for spot 2

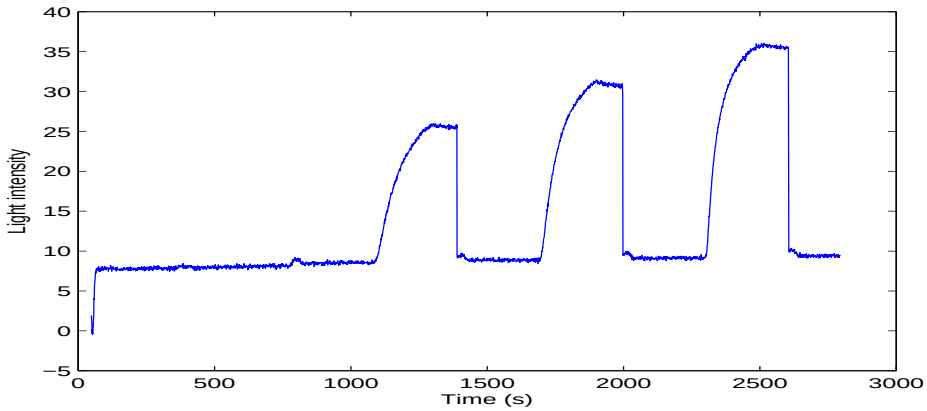

Figure A.3: SPR curve of Spot 3

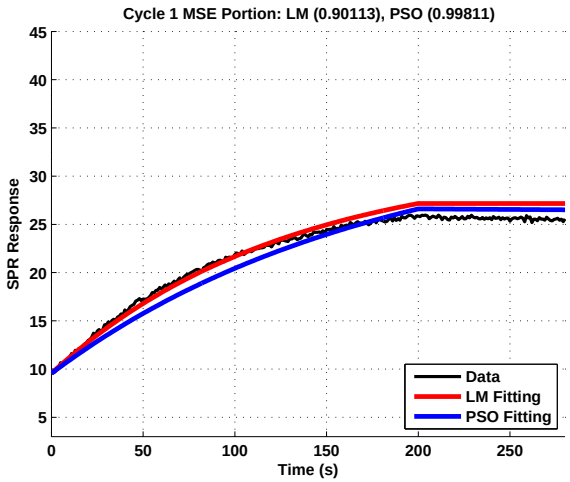

(a)

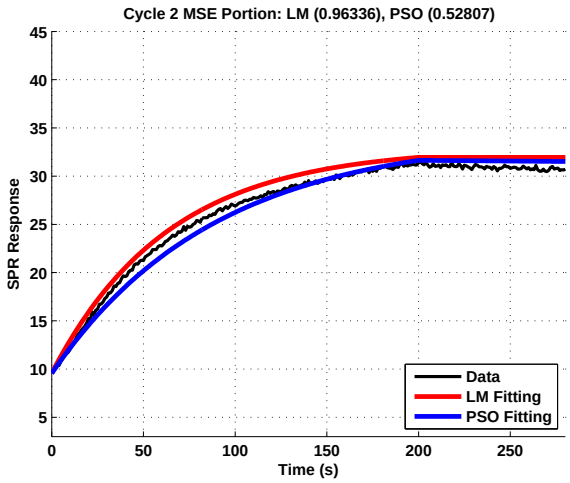

(b)

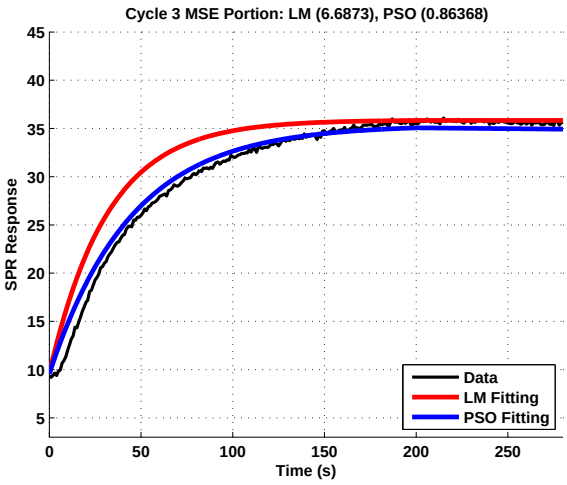

(c)

	$k_a(s^{-1}M^{-1})$	$k_d(s^{-1})$	MSE
LM	4.7400×10^4	0	8.5518
PSO best	3.3677×10^4	6.8332×10^{-5}	2.3899

The ranges of parameters obtained by PSO in 100 Monte-Carlo runs are below:

$$3.1770 \times 10^4 < k_a < 3.4054 \times 10^4$$
$$0 < k_d < 6.8332 \times 10^{-5}$$
$$2.3899 < \text{MSE} < 2.5684$$

Figure A.4: PSO curve fitting result for spot 3

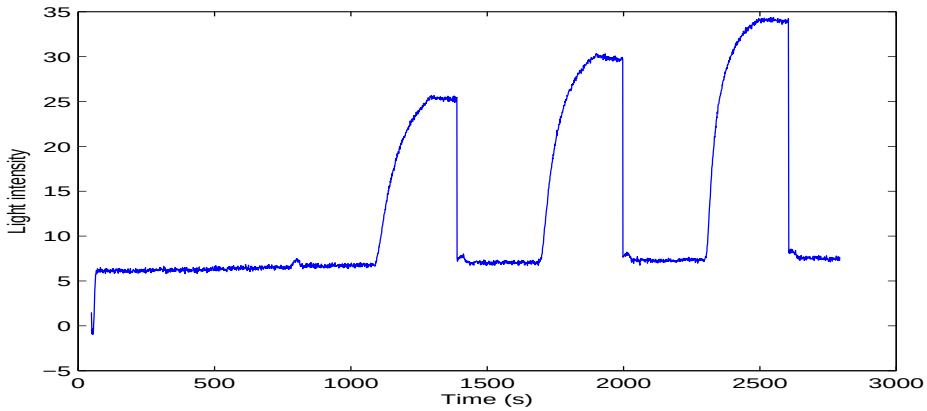

Figure A.5: SPR curve of Spot 4

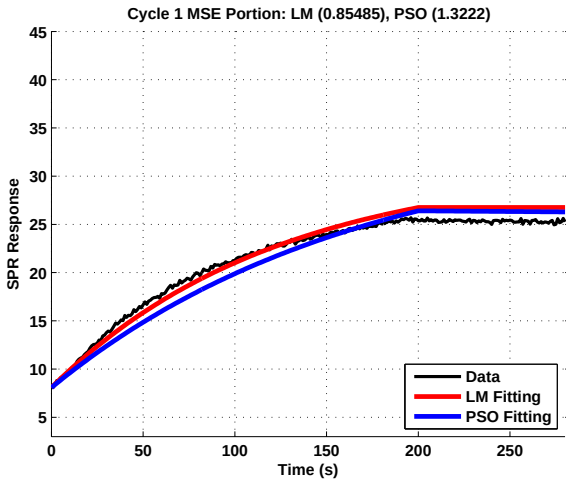

(a)

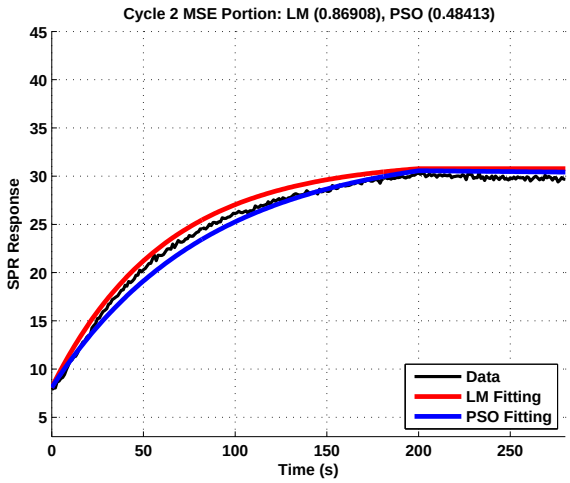

(b)

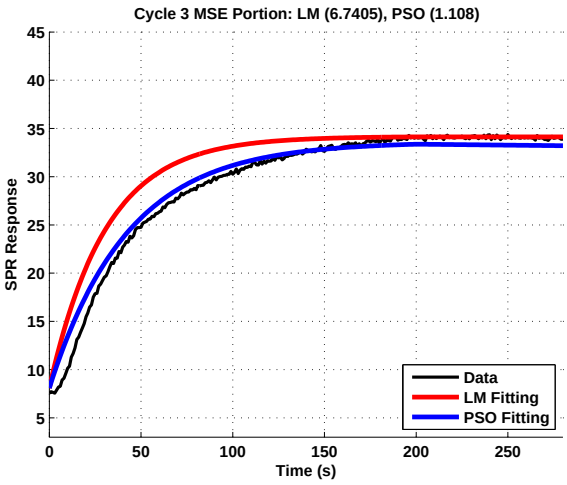

(c)

	$k_a(s^{-1}M^{-1})$	$k_d(s^{-1})$	MSE
LM	4.8800×10^4	0	8.4644
PSO best	3.5122×10^4	7.7952×10^{-5}	2.9143

The ranges of parameters obtained by PSO in 100 Monte-Carlo runs are below:

$$3.5122 \times 10^4 < k_a < 3.5522 \times 10^4$$
$$0 < k_d < 7.7952 \times 10^{-5}$$
$$2.9143 < \text{MSE} < 2.9815$$

Figure A.6: PSO curve fitting result for spot 4

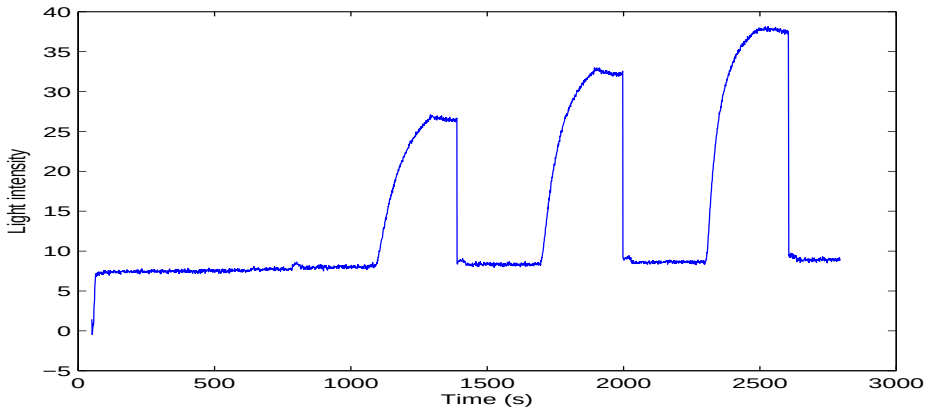

Figure A.7: SPR curve of Spot 5

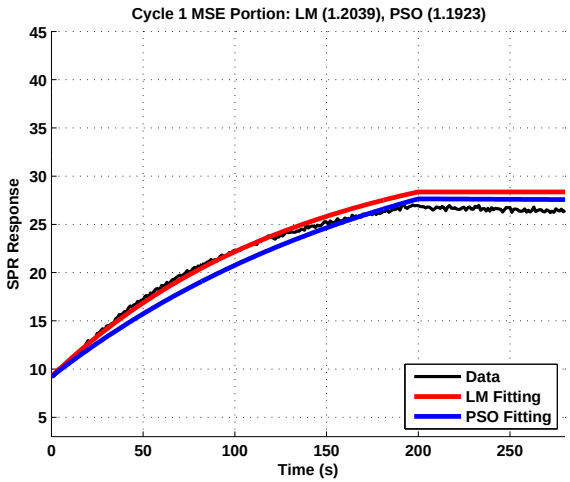

(a)

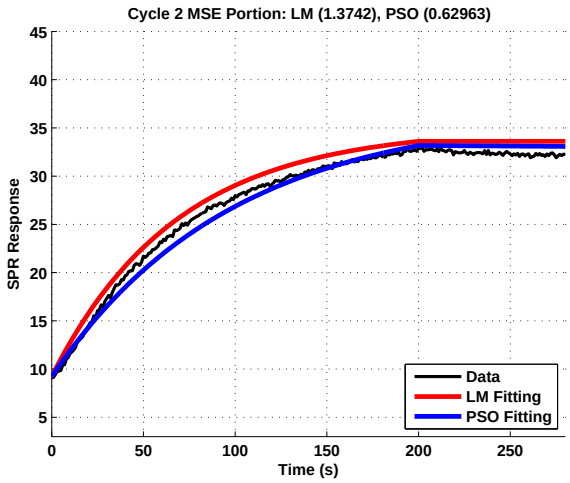

(b)

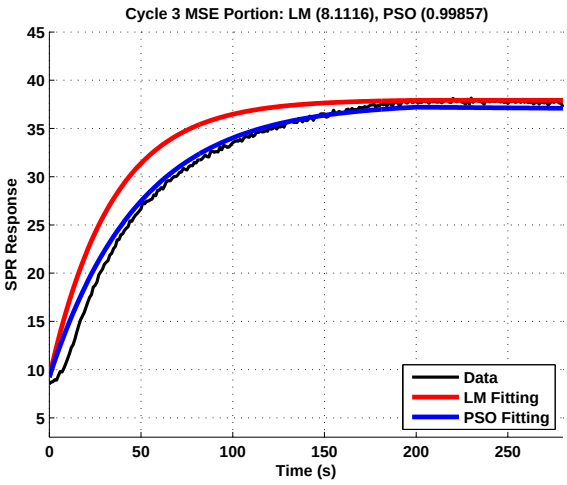

(c)

	$k_a(s^{-1}M^{-1})$	$k_d(s^{-1})$	MSE
LM	4.4100×10^4	0	10.6897
PSO best	3.0690×10^4	4.9807×10^{-5}	2.8205

The ranges of parameters obtained by PSO in 100 Monte-Carlo runs are below:

$$0.9912 \times 10^4 < k_a < 3.0964 \times 10^4$$
$$0 < k_d < 4.9807 \times 10^{-5}$$
$$2.8205 < \text{MSE} < 20.9109$$

Figure A.8: PSO curve fitting result for spot 5

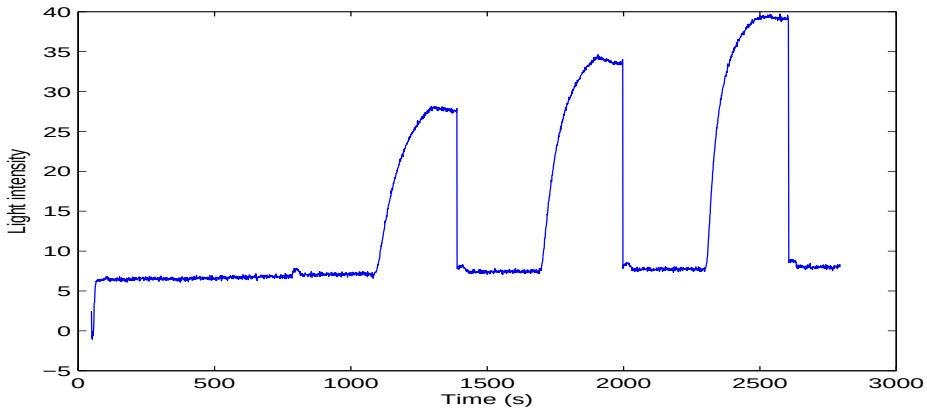

Figure A.9: SPR curve of Spot 6

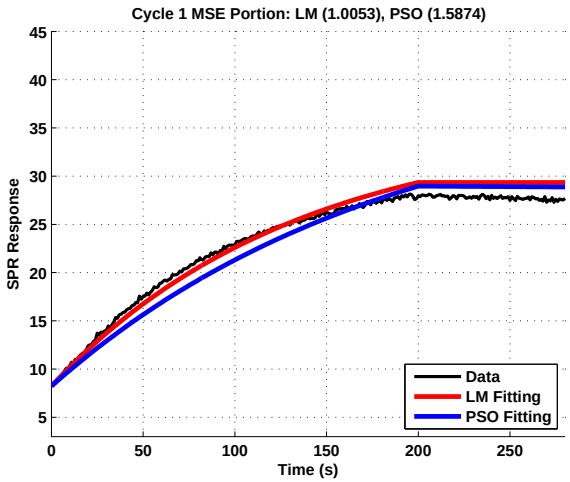

(a)

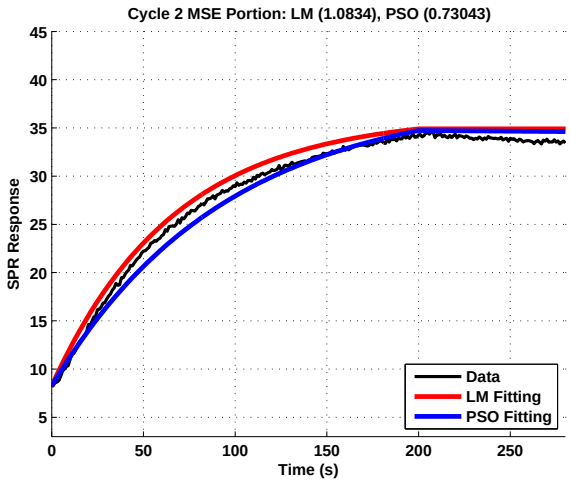

(b)

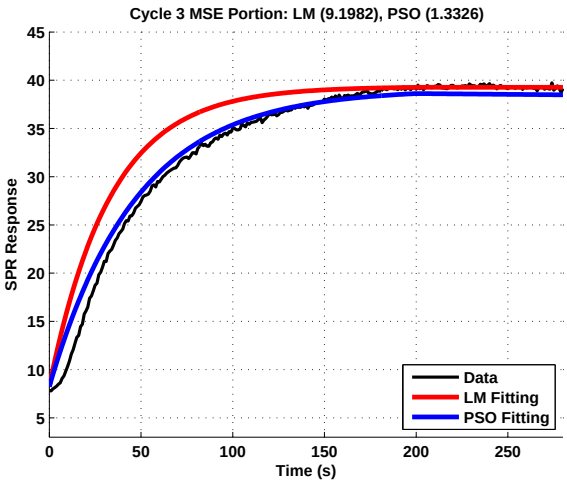

(c)

	$k_a(s^{-1}M^{-1})$	$k_d(s^{-1})$	MSE
LM	4.5200×10^4	0	11.2869
PSO best	3.1773×10^4	5.4298×10^{-5}	3.6504

The ranges of parameters obtained by PSO in 100 Monte-Carlo runs are below:

$$3.1701 \times 10^4 < k_a < 3.1997 \times 10^4$$
$$0 < k_d < 5.4298 \times 10^{-5}$$
$$3.6504 < \text{MSE} < 3.7230$$

Figure A.10: PSO curve fitting result for spot 6

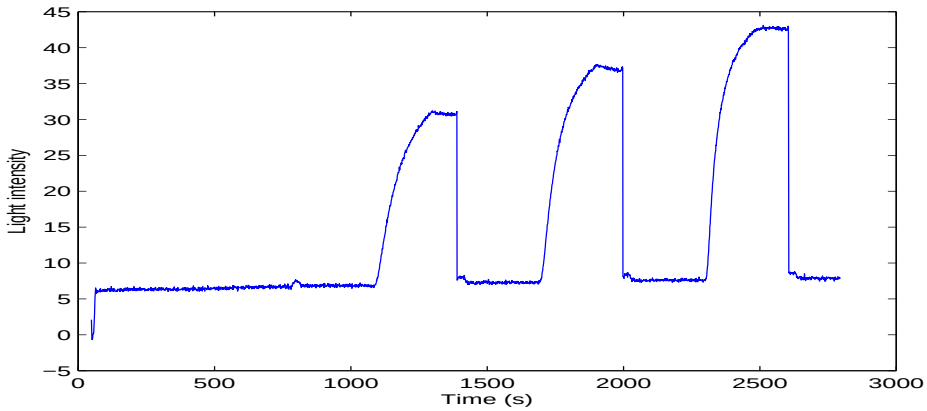

Figure A.11: SPR curve of Spot 7

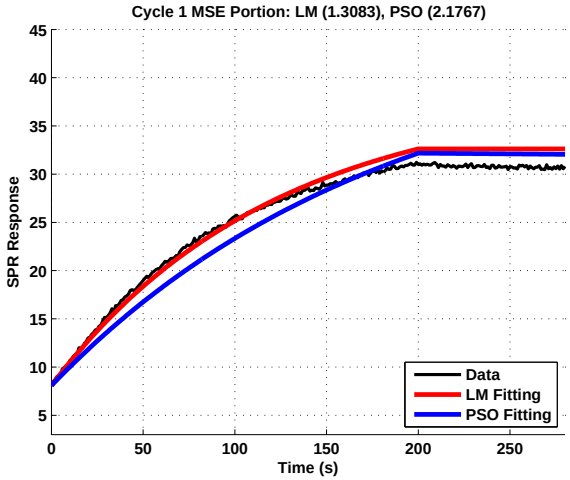

(a)

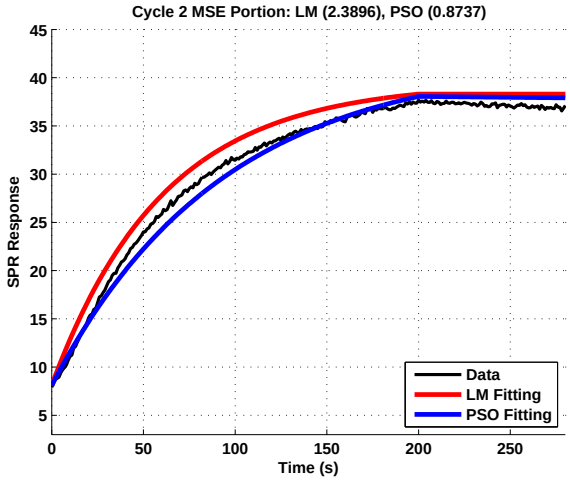

(b)

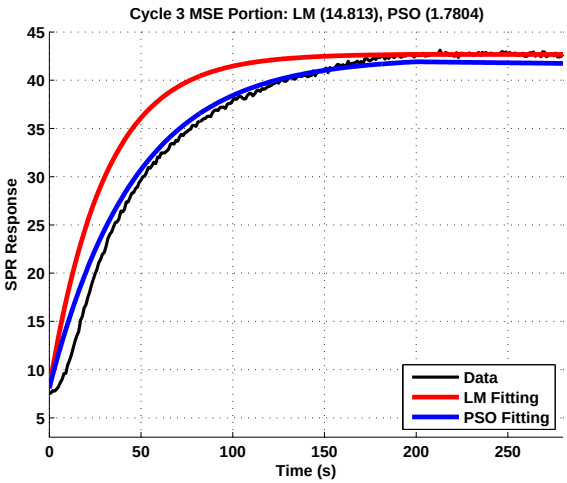

(c)

	$k_a(s^{-1}M^{-1})$	$k_d(s^{-1})$	MSE
LM	4.9600×10^4	0	18.5110
PSO best	3.2335×10^4	6.2582×10^{-5}	4.8308

The ranges of parameters obtained by PSO in 100 Monte-Carlo runs are below:

$$2.8645 \times 10^4 < k_a < 3.3181 \times 10^4$$
$$0 < k_d < 6.2582 \times 10^{-5}$$
$$4.8308 < \text{MSE} < 5.6225$$

Figure A.12: PSO curve fitting result for spot 7

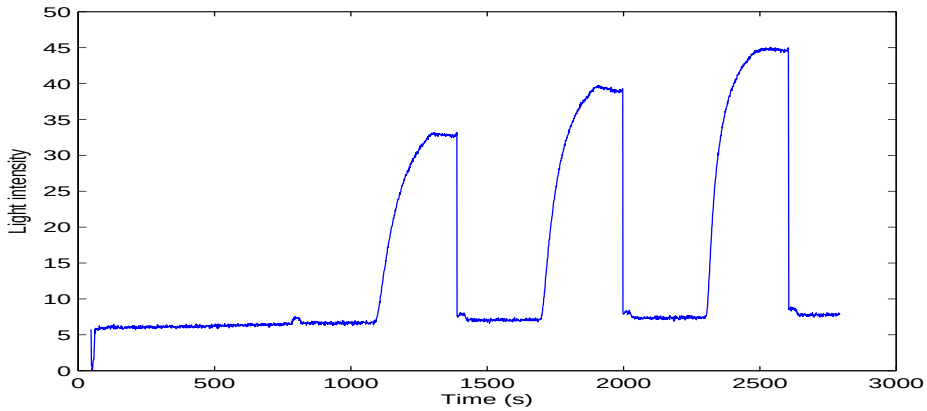

Figure A.13: SPR curve of Spot 8

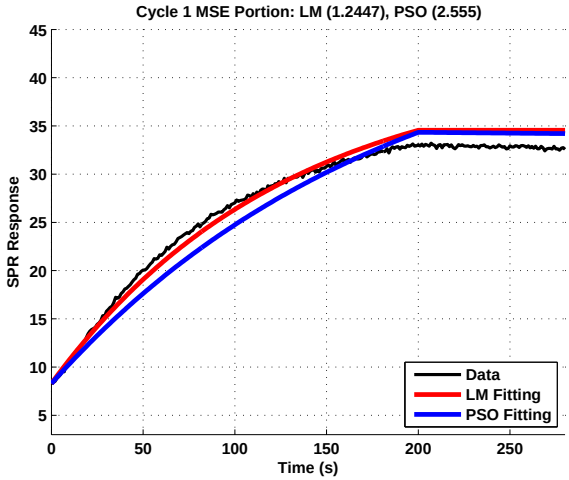

(a)

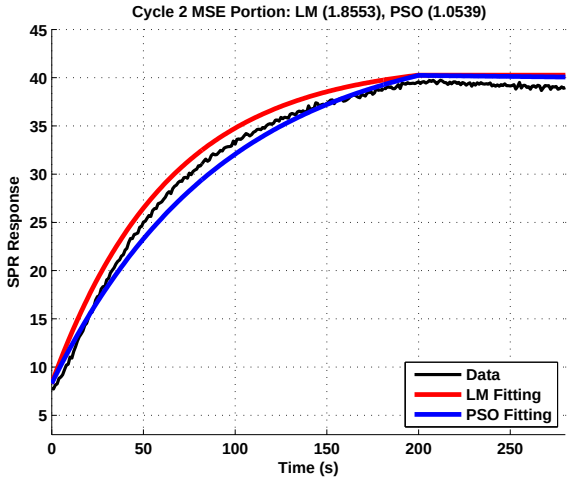

(b)

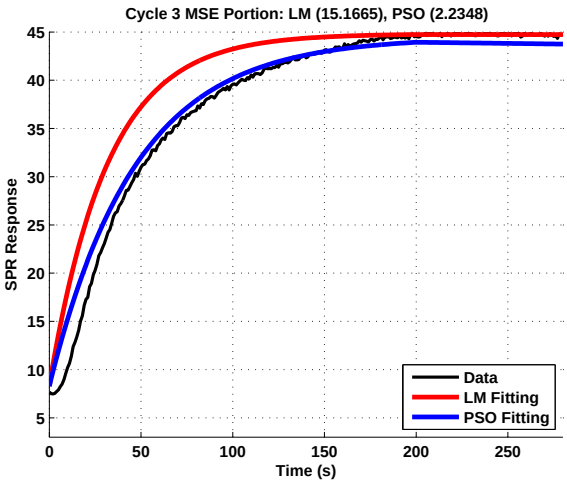

(c)

	$k_a(s^{-1}M^{-1})$	$k_d(s^{-1})$	MSE
LM	4.7200×10^4	0	18.2665
PSO best	3.1914×10^4	6.6521×10^{-5}	5.8437

The ranges of parameters obtained by PSO in 100 Monte-Carlo runs are below:

$$3.1444 \times 10^4 < k_a < 3.2978 \times 10^4$$
$$0 < k_d < 6.6521 \times 10^{-5}$$
$$5.8437 < \text{MSE} < 5.9735$$

Figure A.14: PSO curve fitting result for spot 8

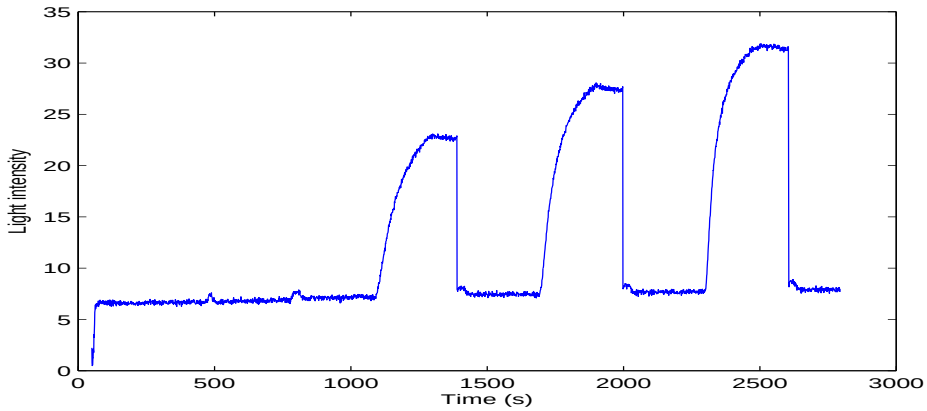

Figure A.15: SPR curve of Spot 9

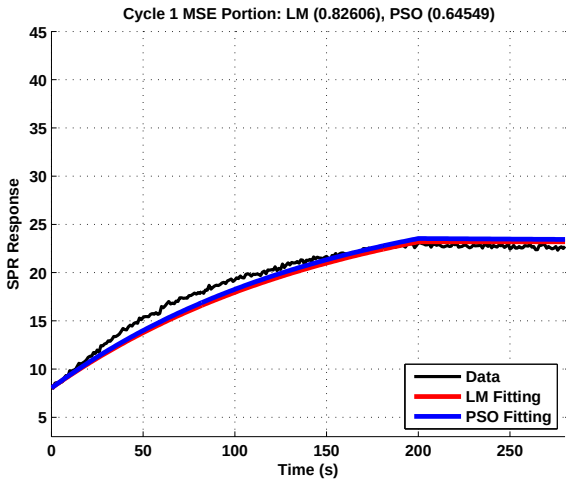

(a)

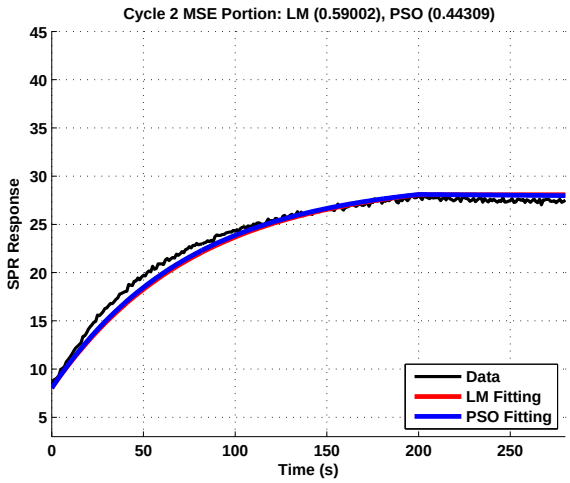

(b)

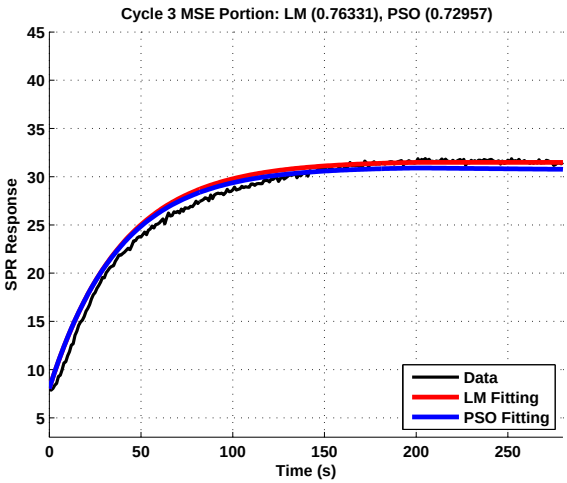

(c)

	$k_a(s^{-1}M^{-1})$	$k_d(s^{-1})$	MSE
LM	3.8200×10^4	0	2.1794
PSO best	3.9394×10^4	7.5838×10^{-5}	1.8181

The ranges of parameters obtained by PSO in 100 Monte-Carlo runs are below:

$$3.4525 \times 10^4 < k_a < 3.9830 \times 10^4$$
$$0 < k_d < 7.5838 \times 10^{-5}$$
$$1.8181 < \text{MSE} < 2.1861$$

Figure A.16: PSO curve fitting result for spot 9

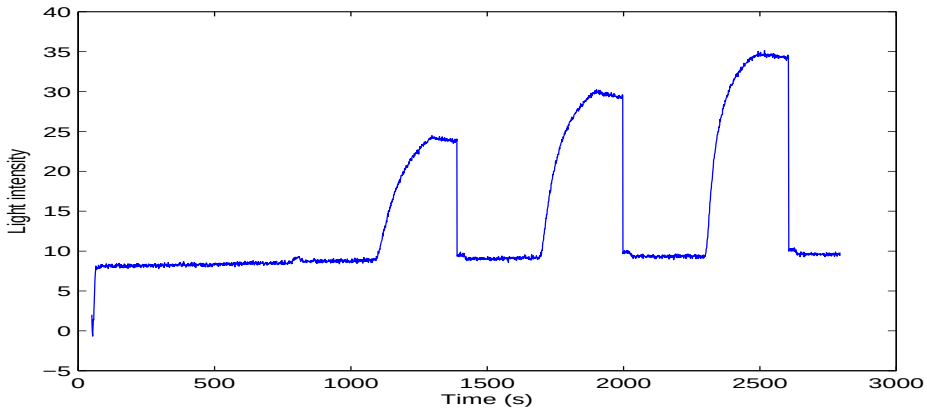

Figure A.17: SPR curve of Spot 10

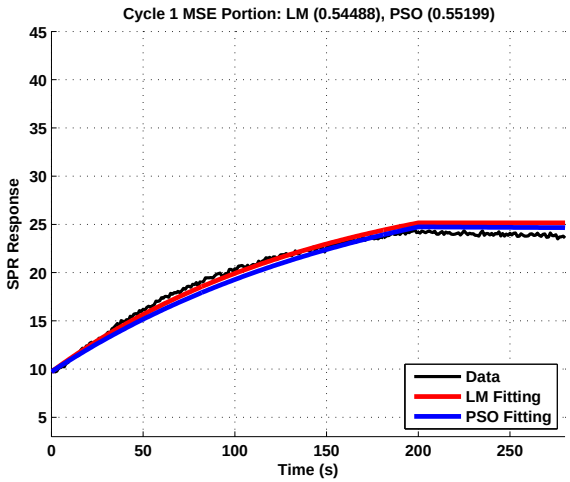

(a)

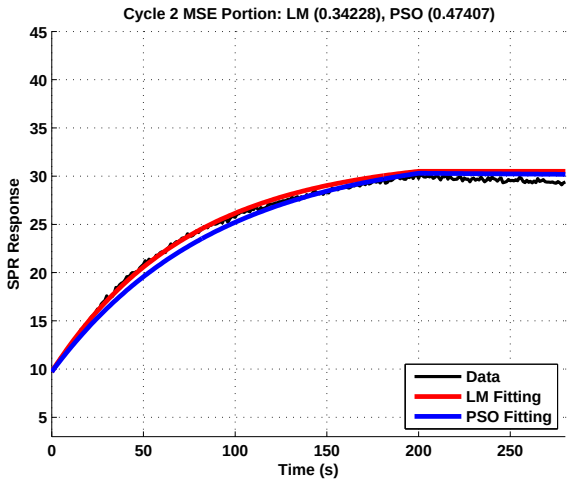

(b)

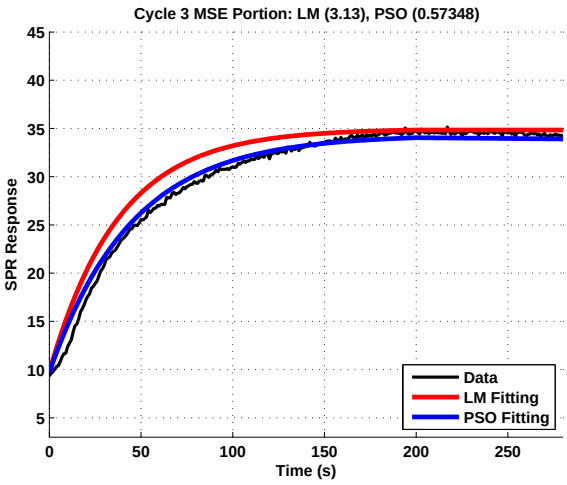

(c)

	$k_a(s^{-1}M^{-1})$	$k_d(s^{-1})$	MSE
LM	4.0000×10^4	0	4.0172
PSO best	3.3308×10^4	6.5380×10^{-5}	1.5995

The ranges of parameters obtained by PSO in 100 Monte-Carlo runs are below:

$$3.1226 \times 10^4 < k_a < 3.3615 \times 10^4$$
$$0 < k_d < 6.5380 \times 10^{-5}$$
$$1.5995 < \text{MSE} < 1.7100$$

Figure A.18: PSO curve fitting result for spot 10

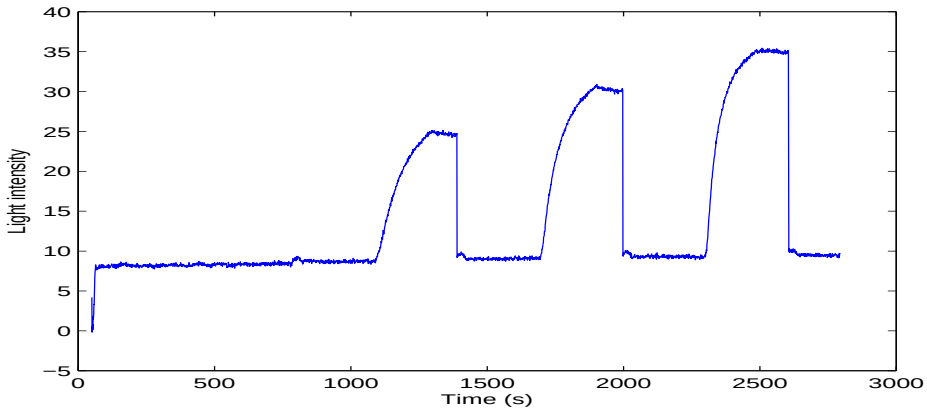

Figure A.19: SPR curve of Spot 11

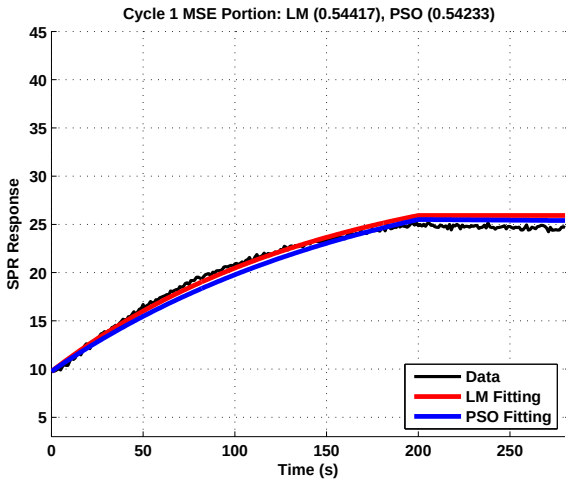

(a)

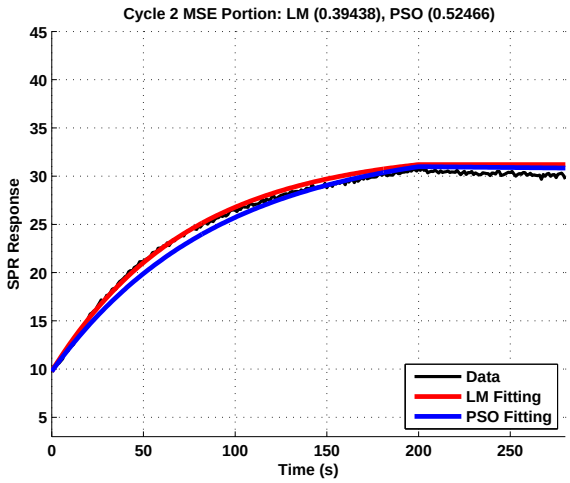

(b)

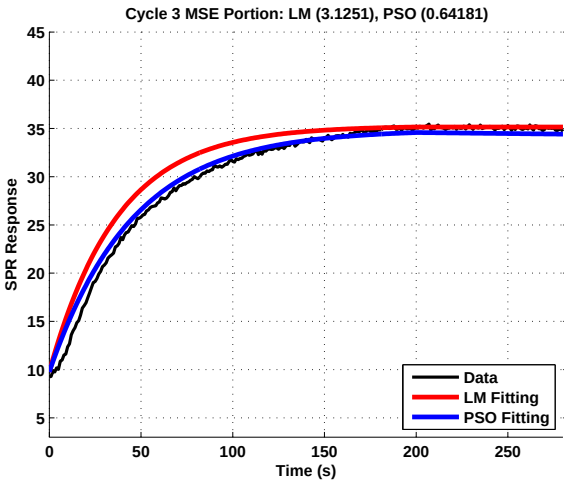

(c)

	$k_a(s^{-1}M^{-1})$	$k_d(s^{-1})$	MSE
LM	4.0500×10^4	0	4.0637
PSO best	3.3085×10^4	8.3508×10^{-5}	1.7088

The ranges of parameters obtained by PSO in 100 Monte-Carlo runs are below:

$$3.3085 \times 10^4 < k_a < 3.3483 \times 10^4$$
$$0 < k_d < 8.3508 \times 10^{-5}$$
$$1.7088 < \text{MSE} < 1.7646$$

Figure A.20: PSO curve fitting result for spot 11

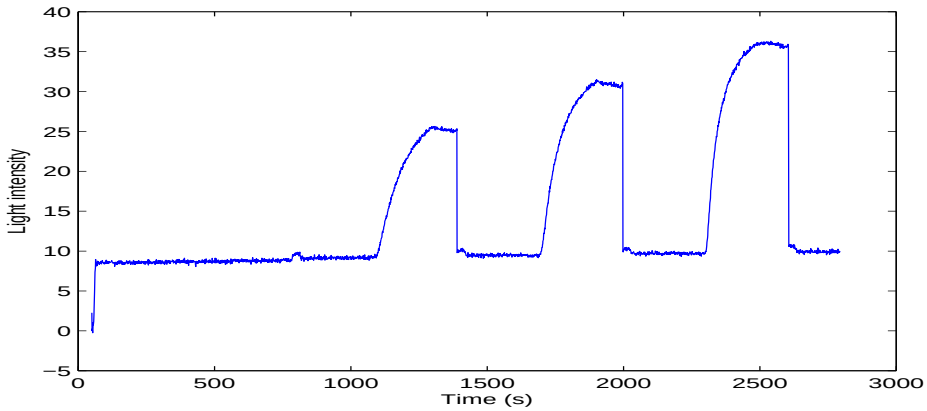

Figure A.21: SPR curve of Spot 12

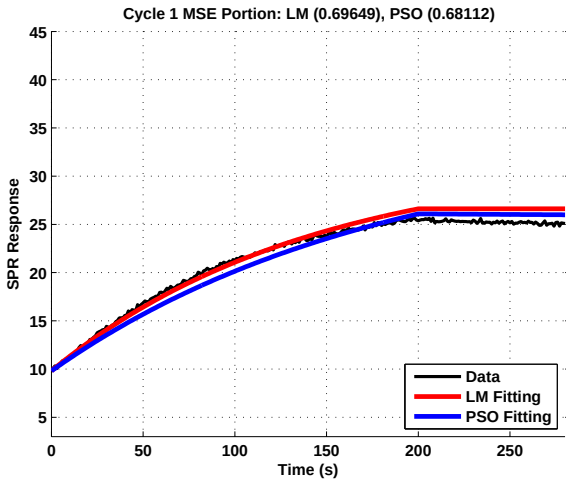

(a)

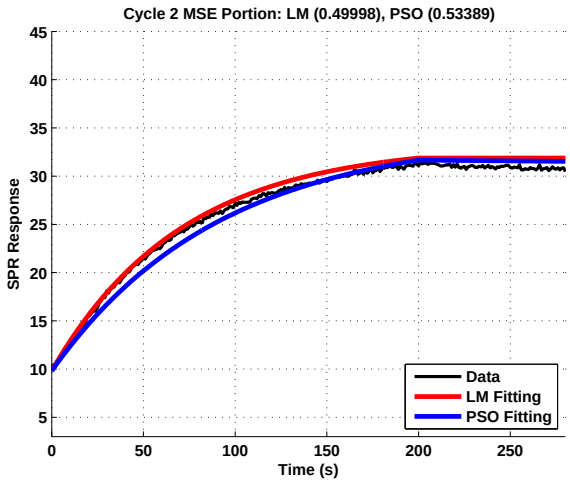

(b)

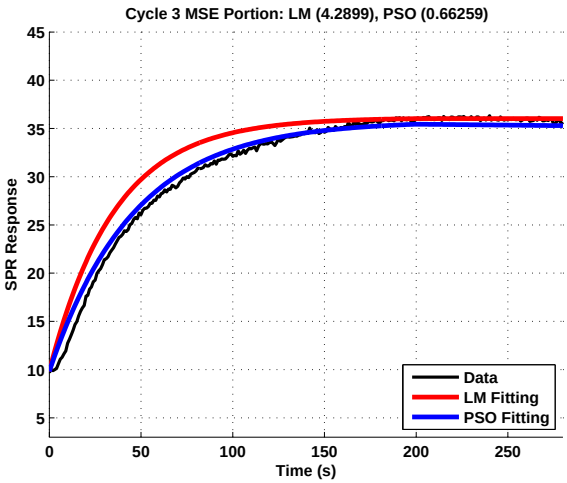

(c)

	$k_a(s^{-1}M^{-1})$	$k_d(s^{-1})$	MSE
LM	4.2400×10^4	0	5.4863
PSO best	3.2648×10^4	7.3786×10^{-5}	1.8776

The ranges of parameters obtained by PSO in 100 Monte-Carlo runs are below:

$$3.2648 \times 10^4 < k_a < 3.3019 \times 10^4$$
$$0 < k_d < 7.3786 \times 10^{-5}$$
$$1.8776 < \text{MSE} < 1.9330$$

Figure A.22: PSO curve fitting result for spot 12

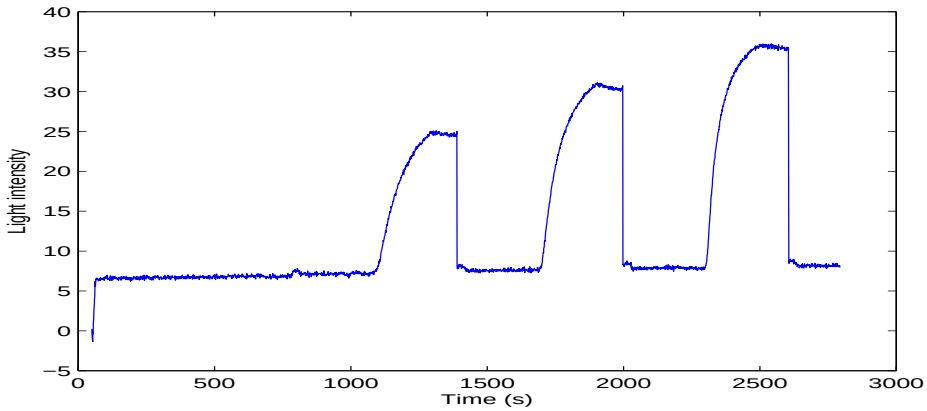

Figure A.23: SPR curve of Spot 13

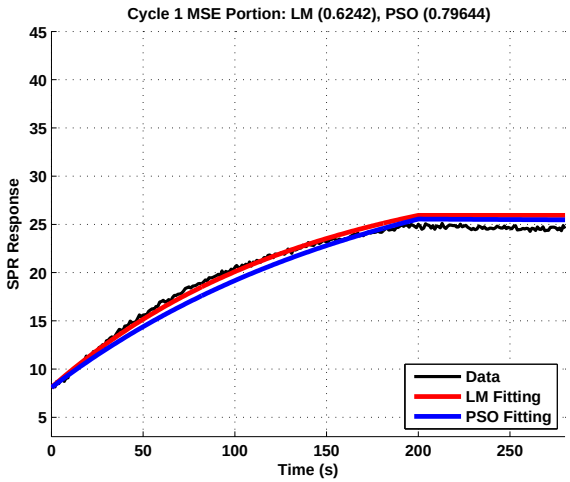

(a)

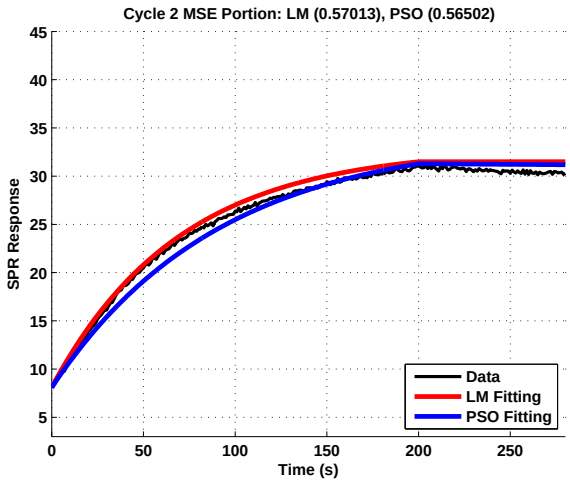

(b)

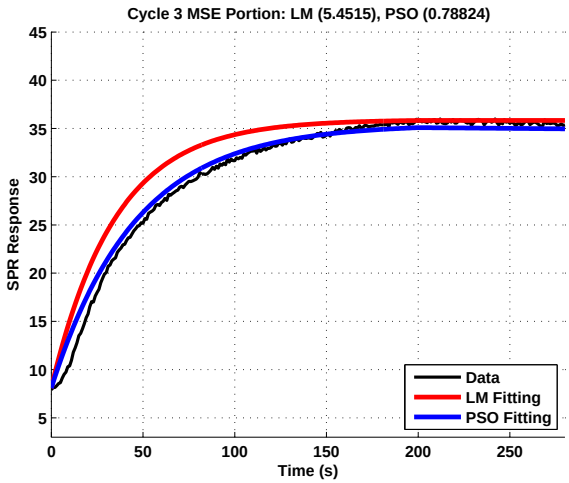

(c)

	$k_a(s^{-1}M^{-1})$	$k_d(s^{-1})$	MSE
LM	4.3200×10^4	0	6.6458
PSO best	3.2797×10^4	5.8035×10^{-5}	2.1497

The ranges of parameters obtained by PSO in 100 Monte-Carlo runs are below:

$$3.1485 \times 10^4 < k_a < 3.3110 \times 10^4$$
$$0 < k_d < 5.8035 \times 10^{-5}$$
$$2.1497 < \text{MSE} < 2.2594$$

Figure A.24: PSO curve fitting result for spot 13

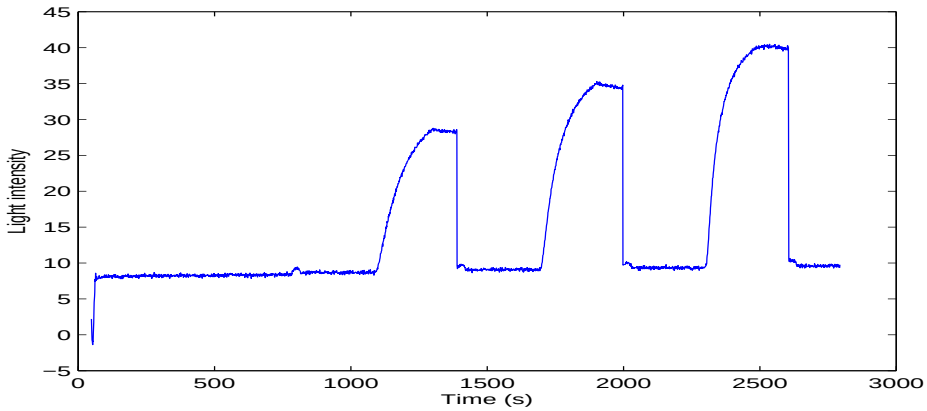

Figure A.25: SPR curve of Spot 14

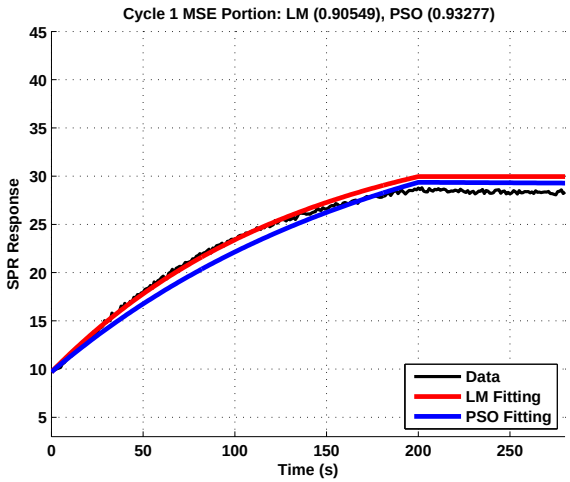

(a)

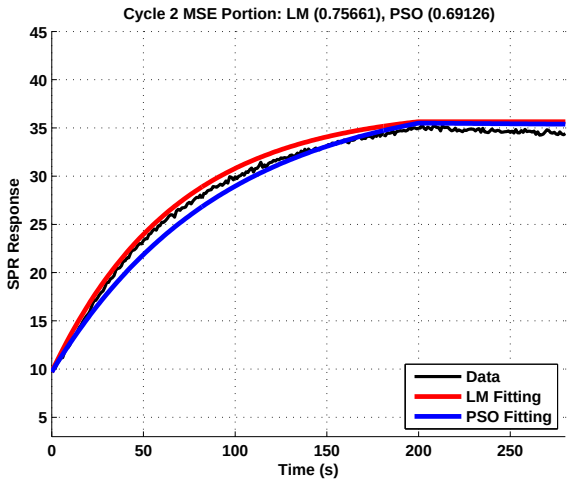

(b)

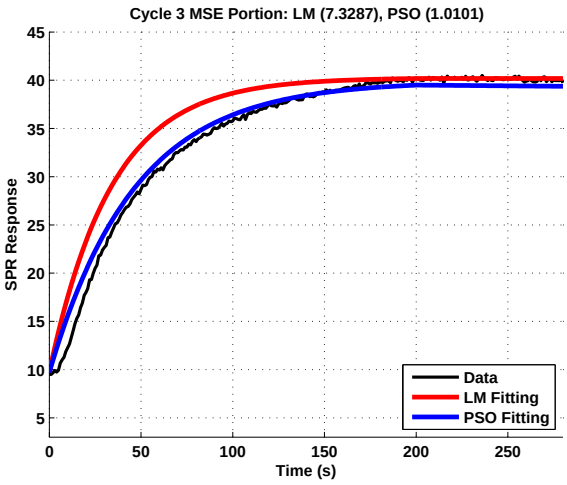

(c)

	$k_a(s^{-1}M^{-1})$	$k_d(s^{-1})$	MSE
LM	4.4200×10^4	0	8.9908
PSO best	3.2292×10^4	5.2531×10^{-5}	2.6341

The ranges of parameters obtained by PSO in 100 Monte-Carlo runs are below:

$$3.2291 \times 10^4 < k_a < 3.2645 \times 10^4$$
$$0 < k_d < 5.2531 \times 10^{-5}$$
$$2.6341 < \text{MSE} < 2.6881$$

Figure A.26: PSO curve fitting result for spot 14

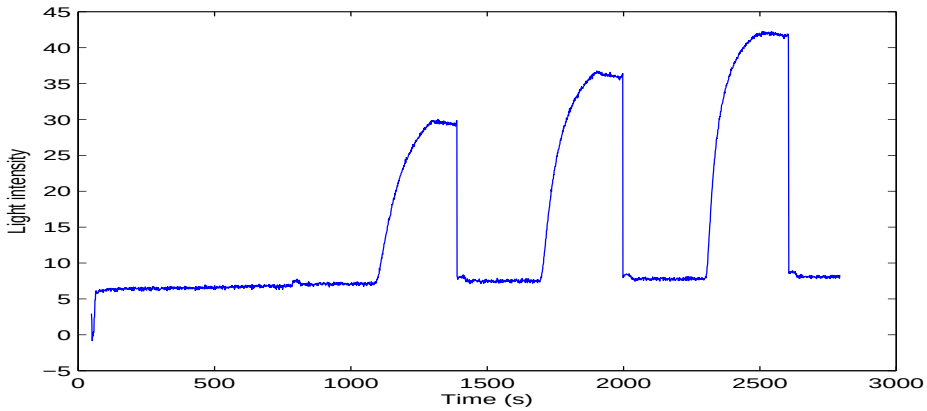

Figure A.27: SPR curve of Spot 15

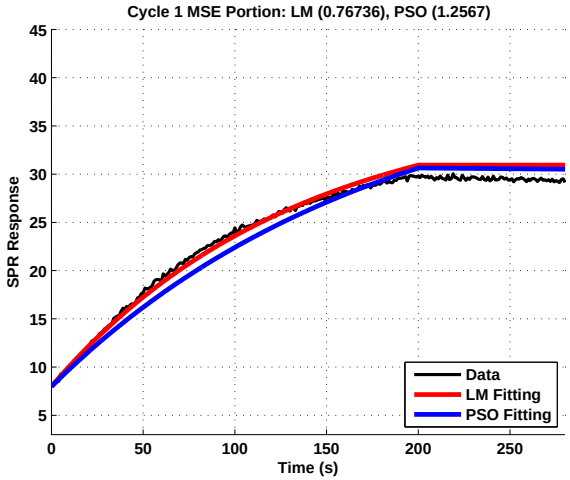

(a)

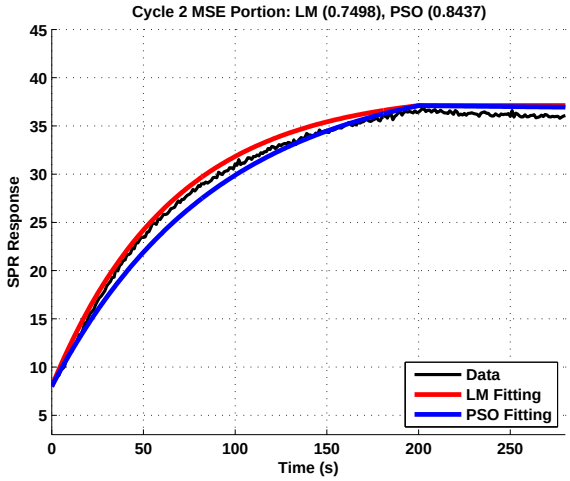

(b)

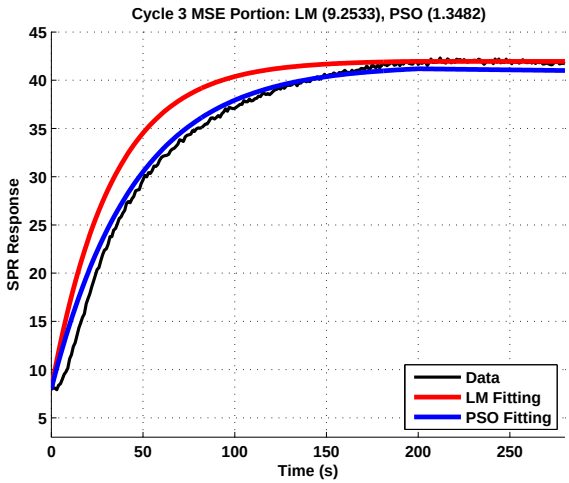

(c)

	$k_a(s^{-1}M^{-1})$	$k_d(s^{-1})$	MSE
LM	4.5300×10^4	0	10.7705
PSO best	3.3166×10^4	6.7892×10^{-5}	3.4486

The ranges of parameters obtained by PSO in 100 Monte-Carlo runs are below:

$$3.3166 \times 10^4 < k_a < 3.3580 \times 10^4$$
$$0 < k_d < 6.7892 \times 10^{-5}$$
$$3.4486 < \text{MSE} < 3.5370$$

Figure A.28: PSO curve fitting result for spot 15

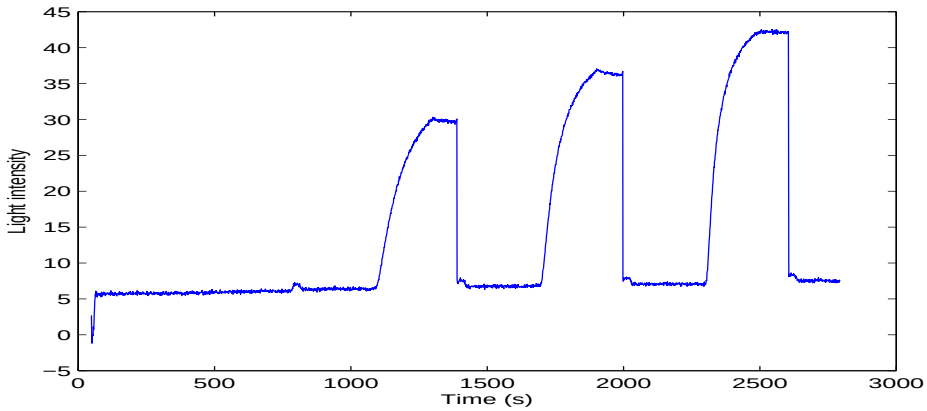

Figure A.29: SPR curve of Spot 16

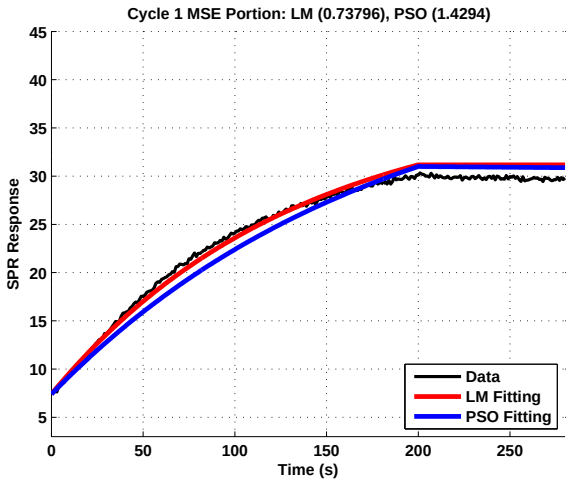

(a)

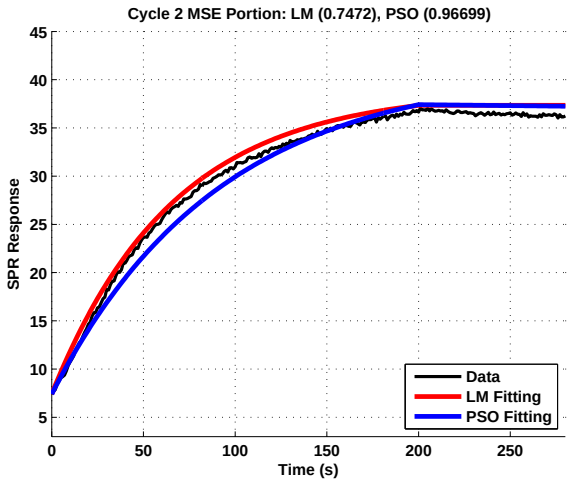

(b)

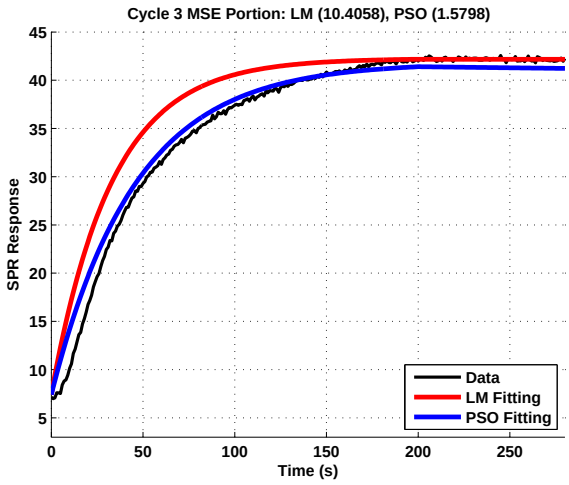

(c)

	$k_a(s^{-1}M^{-1})$	$k_d(s^{-1})$	MSE
LM	4.5500×10^4	0	11.8910
PSO best	3.2913×10^4	6.6027×10^{-5}	3.9762

The ranges of parameters obtained by PSO in 100 Monte-Carlo runs are below:

$$2.2070 \times 10^4 < k_a < 3.3260 \times 10^4$$
$$0 < k_d < 6.6027 \times 10^{-5}$$
$$3.9762 < \text{MSE} < 9.3419$$

Figure A.30: PSO curve fitting result for spot 16

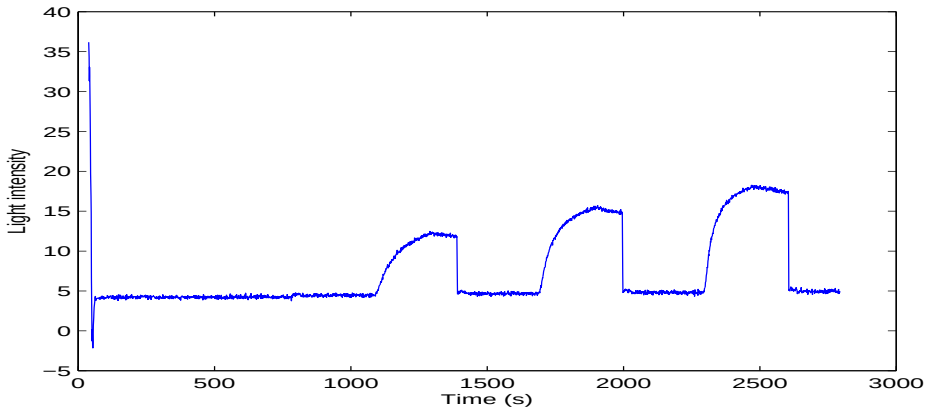

Figure A.31: SPR curve of Spot 81

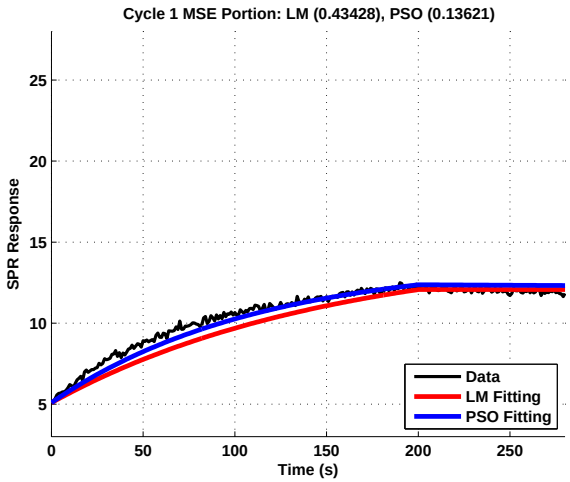

(a)

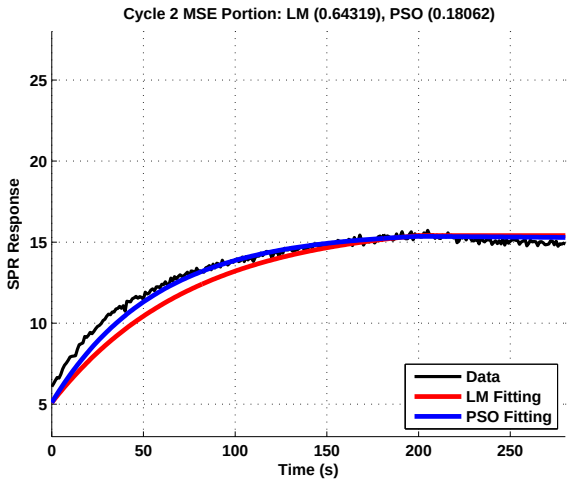

(b)

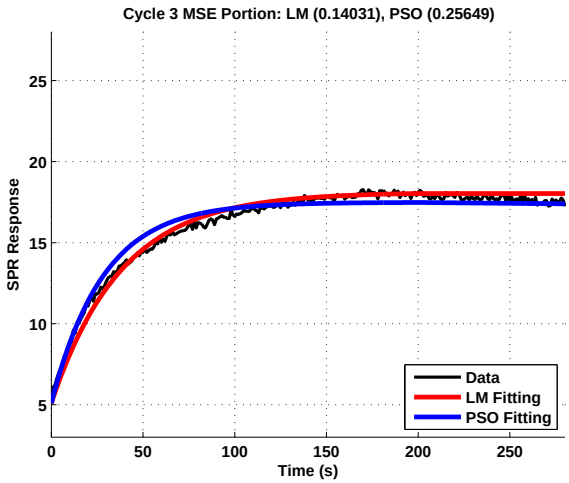

(c)

	$k_a(s^{-1}M^{-1})$	$k_d(s^{-1})$	MSE
LM	3.9300×10^4	0	1.2178
PSO best	5.3109×10^4	8.3513×10^{-5}	0.5733

The ranges of parameters obtained by PSO in 100 Monte-Carlo runs are below:

$$5.3096 \times 10^4 < k_a < 5.3619 \times 10^4$$
$$0 < k_d < 8.3513 \times 10^{-5}$$
$$0.5733 < \text{MSE} < 0.5848$$

Figure A.32: PSO curve fitting result for spot 81

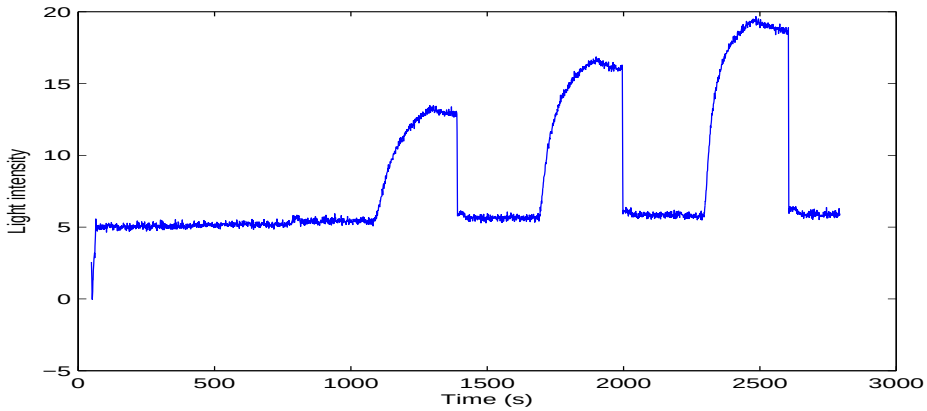

Figure A.33: SPR curve of Spot 82

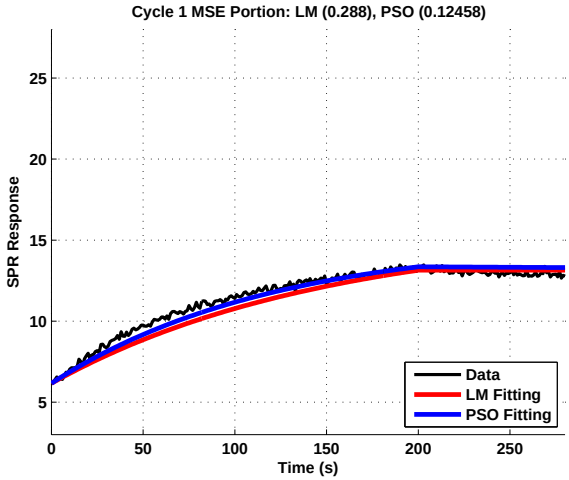

(a)

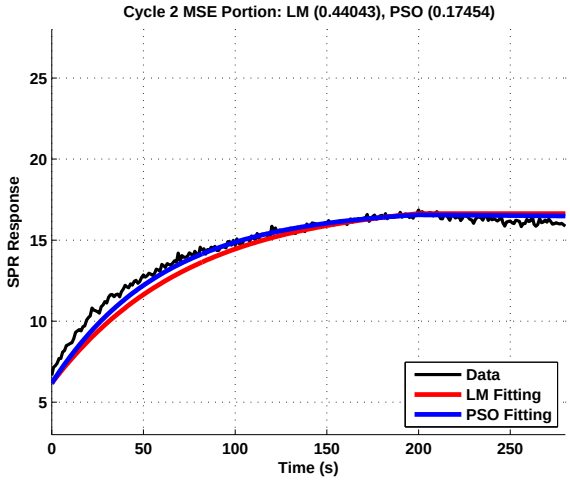

(b)

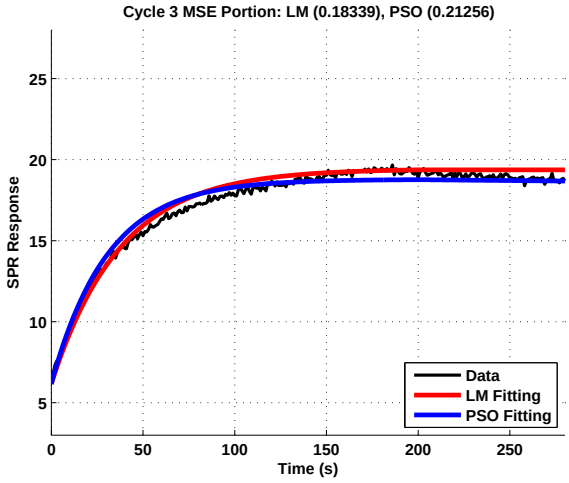

(c)

	$k_a(s^{-1}M^{-1})$	$k_d(s^{-1})$	MSE
LM	4.0000×10^4	0	0.9118
PSO best	4.8966×10^4	8.5889×10^{-5}	0.5117

The ranges of parameters obtained by PSO in 100 Monte-Carlo runs are below:

$$4.3644 \times 10^4 < k_a < 4.9534 \times 10^4$$
$$0 < k_d < 8.5889 \times 10^{-5}$$
$$0.5117 < \text{MSE} < 0.5905$$

Figure A.34: PSO curve fitting result for spot 82

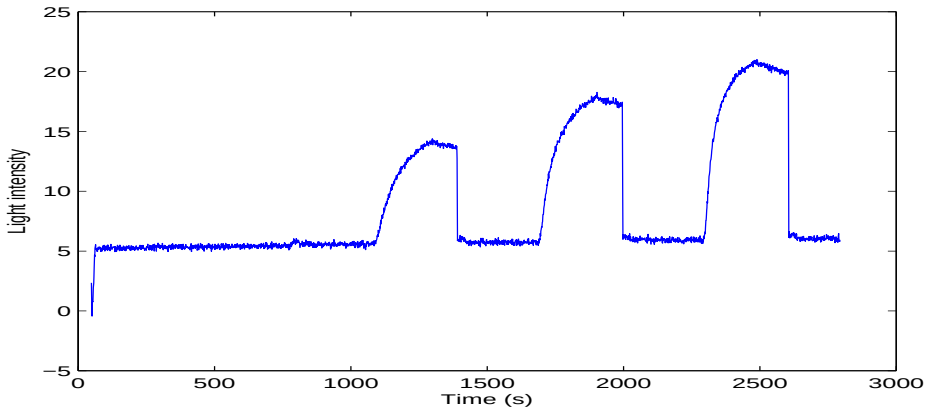

Figure A.35: SPR curve of Spot 83

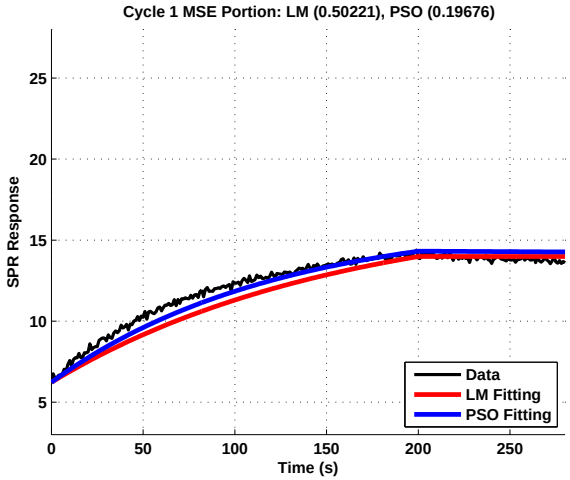

(a)

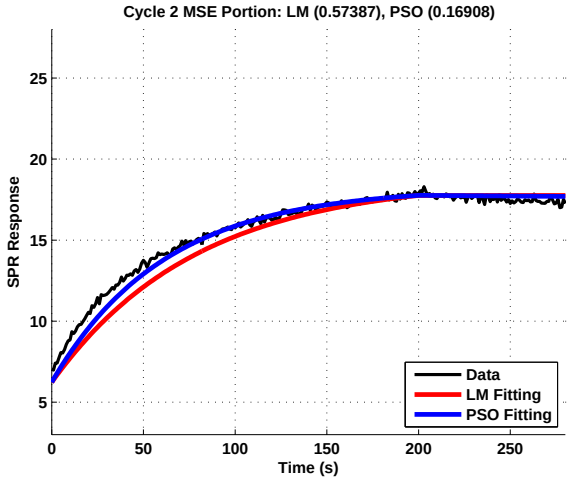

(b)

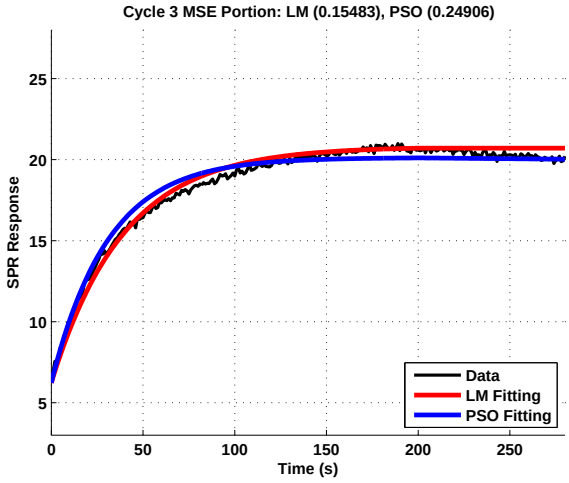

(c)

	$k_a(s^{-1}M^{-1})$	$k_d(s^{-1})$	MSE
LM	3.8100×10^4	0	1.2309
PSO best	4.8692×10^4	7.1950×10^{-5}	0.6149

The ranges of parameters obtained by PSO in 100 Monte-Carlo runs are below:

$$4.8692 \times 10^4 < k_a < 4.9078 \times 10^4$$
$$0 < k_d < 7.1950 \times 10^{-5}$$
$$0.6149 < \text{MSE} < 0.6291$$

Figure A.36: PSO curve fitting result for spot 83

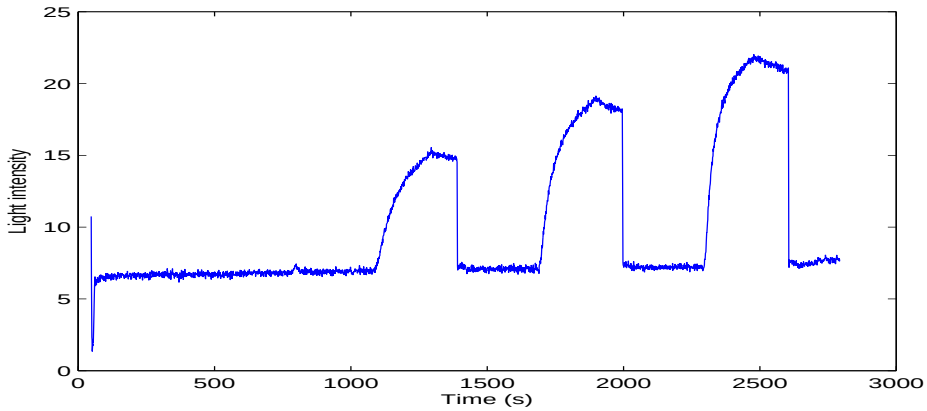

Figure A.37: SPR curve of Spot 84

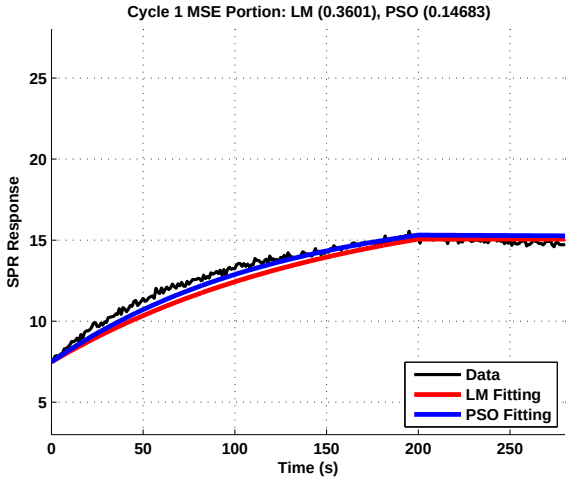

(a)

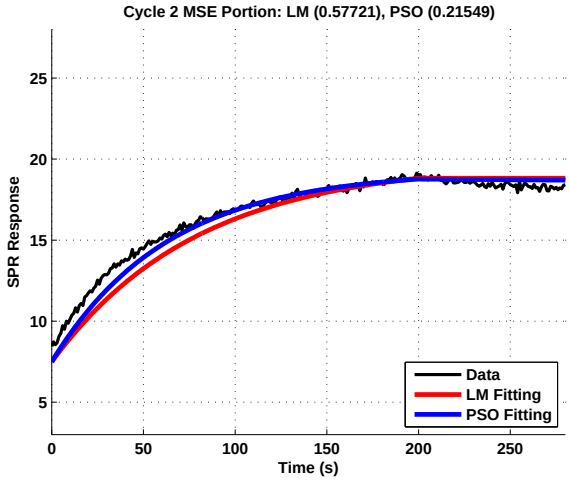

(b)

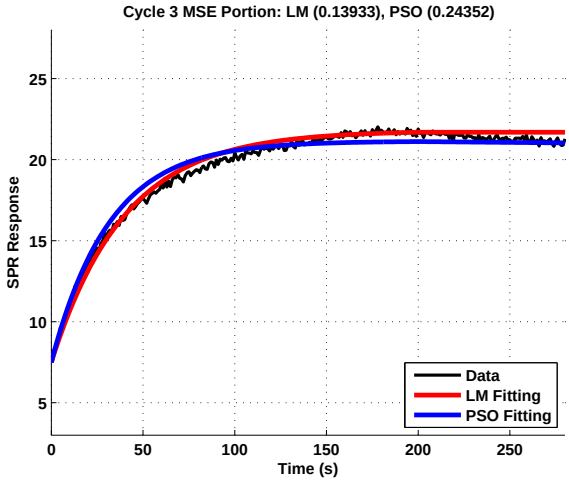

(c)

	$k_a(s^{-1}M^{-1})$	$k_d(s^{-1})$	MSE
LM	3.7800×10^4	0	1.0766
PSO best	4.7274×10^4	7.4515×10^{-5}	0.6058

The ranges of parameters obtained by PSO in 100 Monte-Carlo runs are below:

$$3.9514 \times 10^4 < k_a < 4.7690 \times 10^4$$
$$0 < k_d < 7.4515 \times 10^{-5}$$
$$0.6058 < \text{MSE} < 0.8283$$

Figure A.38: PSO curve fitting result for spot 84

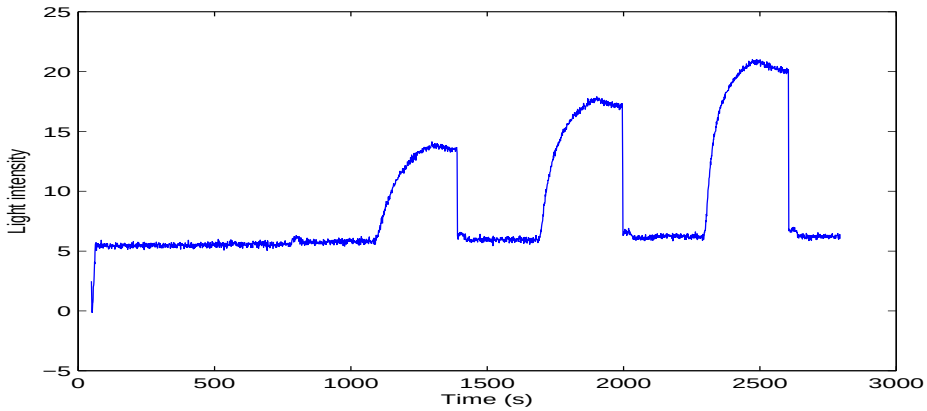

Figure A.39: SPR curve of Spot 85

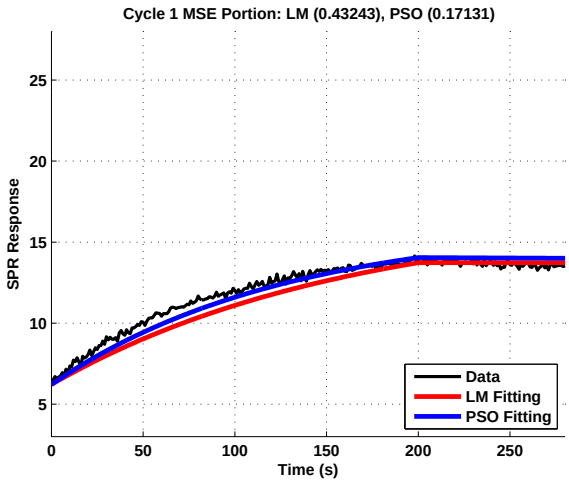

(a)

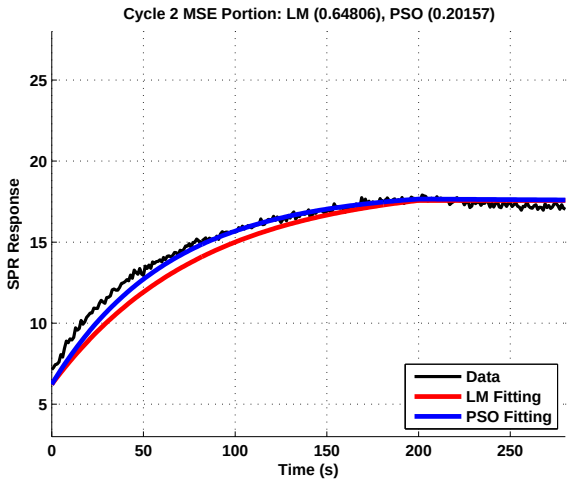

(b)

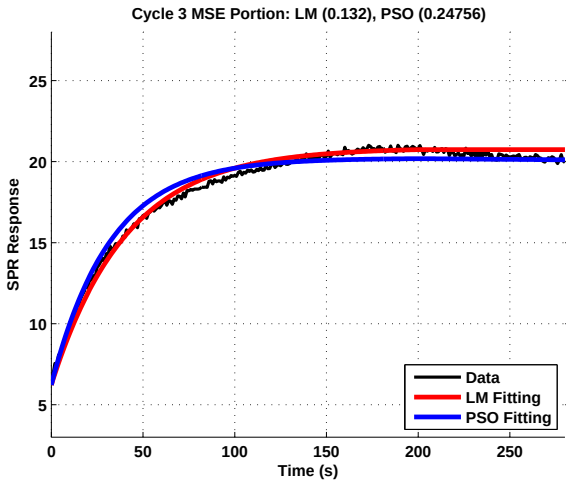

(c)

	$k_a(s^{-1}M^{-1})$	$k_d(s^{-1})$	MSE
LM	3.6900×10^4	0	1.2125
PSO best	4.6796×10^4	6.5092×10^{-5}	0.6204

The ranges of parameters obtained by PSO in 100 Monte-Carlo runs are below:

$$4.1347 \times 10^4 < k_a < 4.7195 \times 10^4$$
$$0 < k_d < 6.5092 \times 10^{-5}$$
$$0.6204 < \text{MSE} < 0.7245$$

Figure A.40: PSO curve fitting result for spot 85

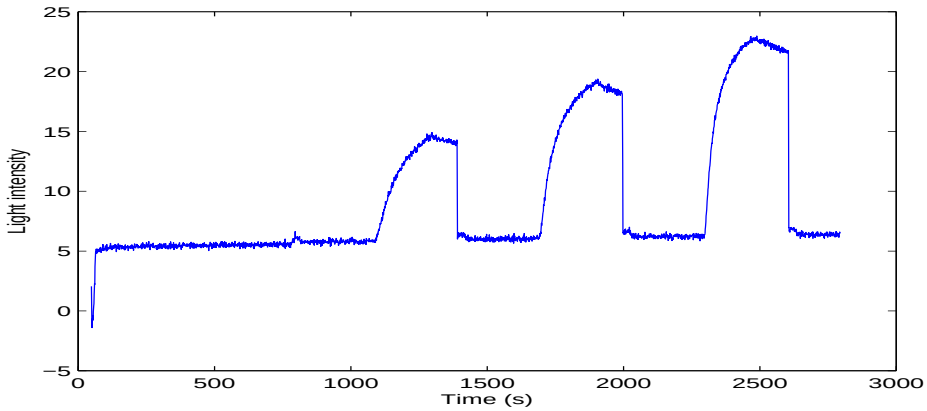

Figure A.41: SPR curve of Spot 86

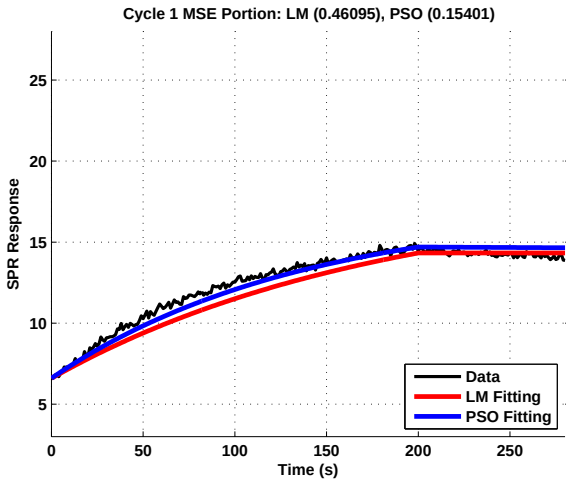

(a)

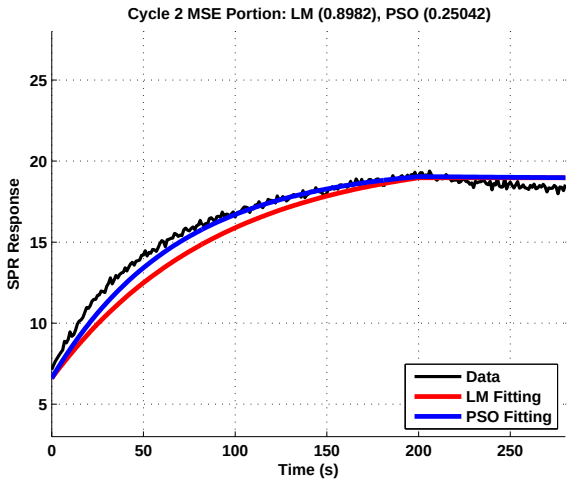

(b)

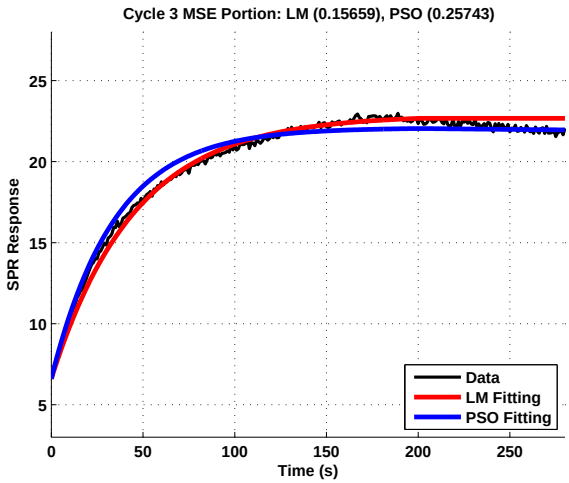

(c)

	$k_a(s^{-1}M^{-1})$	$k_d(s^{-1})$	MSE
LM	3.3100×10^4	0	1.5157
PSO best	4.3628×10^4	7.0387×10^{-5}	0.6619

The ranges of parameters obtained by PSO in 100 Monte-Carlo runs are below:

$$3.6086 \times 10^4 < k_a < 4.4000 \times 10^4$$
$$0 < k_d < 7.0387 \times 10^{-5}$$
$$0.6619 < \text{MSE} < 0.9377$$

Figure A.42: PSO curve fitting result for spot 86

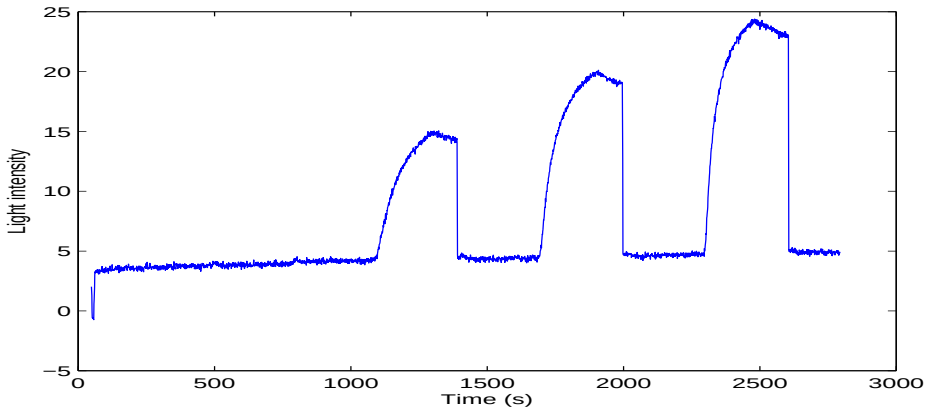

Figure A.43: SPR curve of Spot 87

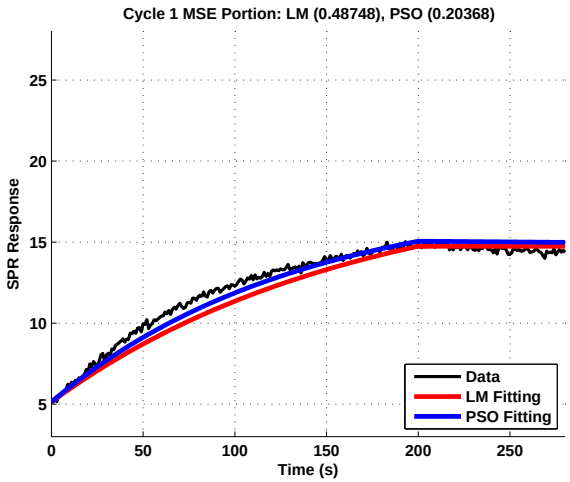

(a)

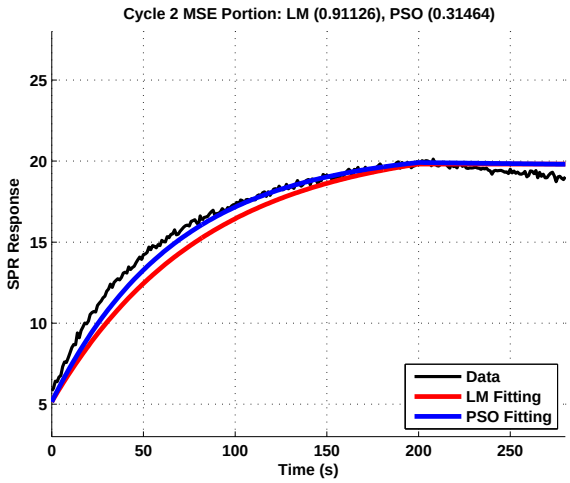

(b)

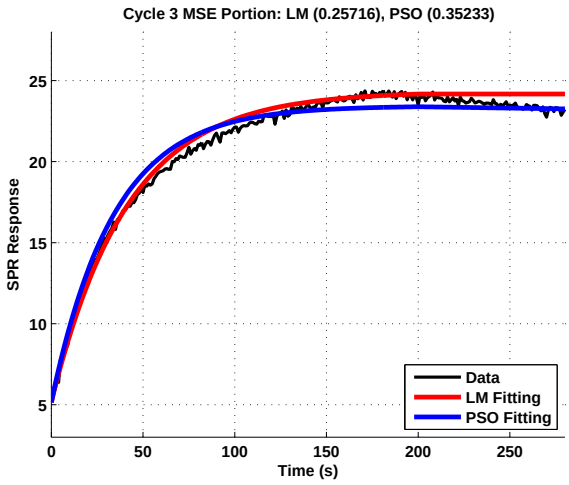

(c)

	$k_a(s^{-1}M^{-1})$	$k_d(s^{-1})$	MSE
LM	3.6300×10^4	0	1.6559
PSO best	4.4077×10^4	9.1886×10^{-5}	0.8707

The ranges of parameters obtained by PSO in 100 Monte-Carlo runs are below:

$$4.3051 \times 10^4 < k_a < 4.4662 \times 10^4$$
$$0 < k_d < 9.1886 \times 10^{-5}$$
$$0.8707 < \text{MSE} < 0.9298$$

Figure A.44: PSO curve fitting result for spot 87

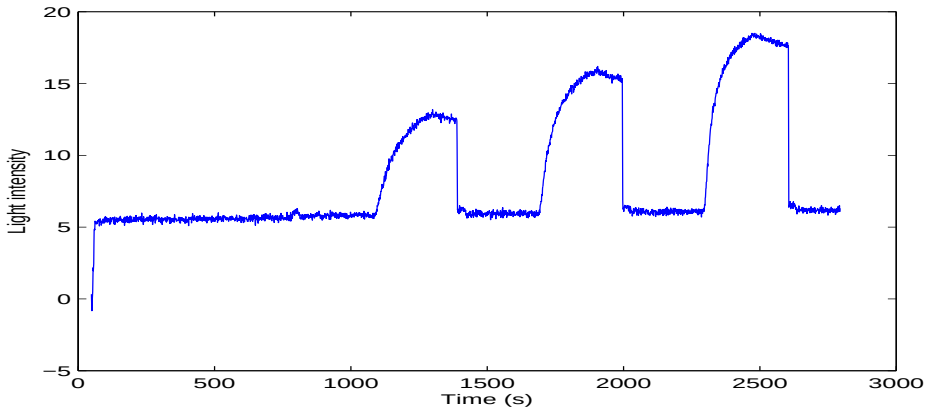

Figure A.45: SPR curve of Spot 89

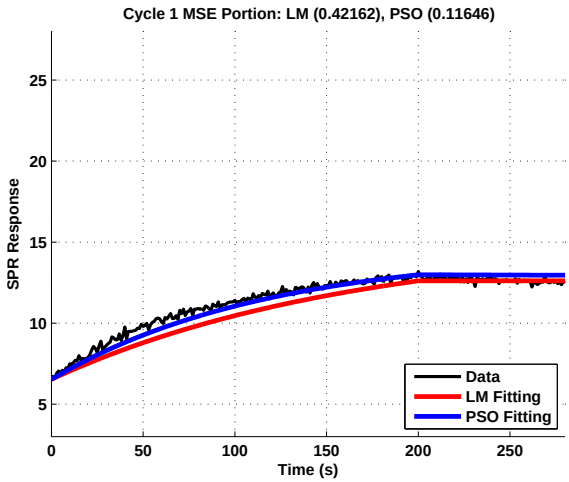

(a)

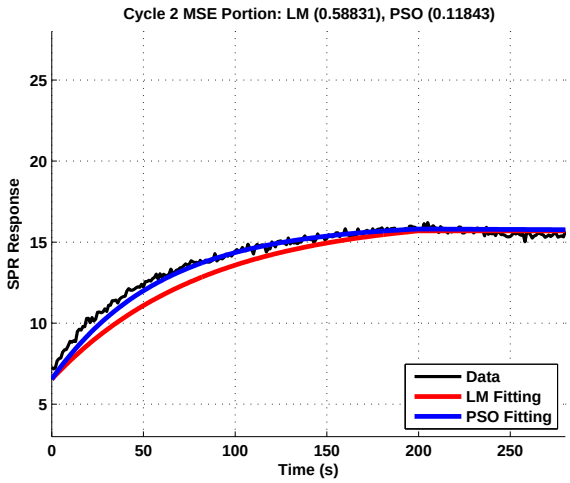

(b)

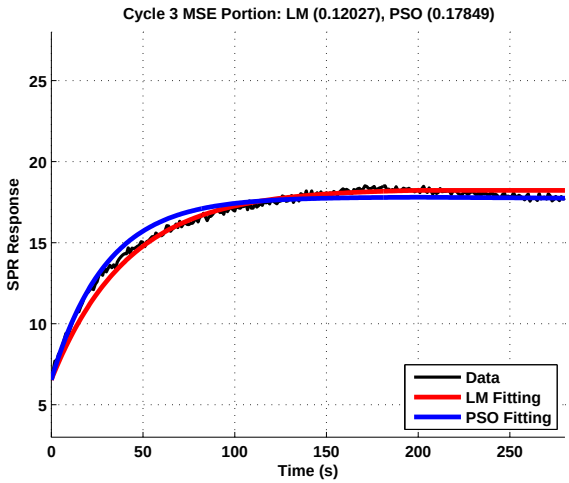

(c)

	$k_a(s^{-1}M^{-1})$	$k_d(s^{-1})$	MSE
LM	3.6100×10^4	0	1.1302
PSO best	5.0284×10^4	6.0331×10^{-5}	0.4134

The ranges of parameters obtained by PSO in 100 Monte-Carlo runs are below:

$$5.0116 \times 10^4 < k_a < 5.0600 \times 10^4$$
$$0 < k_d < 6.0331 \times 10^{-5}$$
$$0.4134 < \text{MSE} < 0.4218$$

Figure A.46: PSO curve fitting result for spot 89

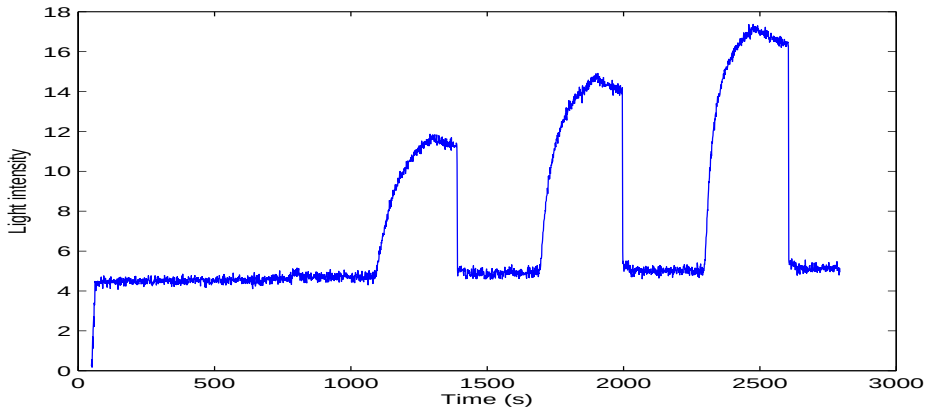

Figure A.47: SPR curve of Spot 90

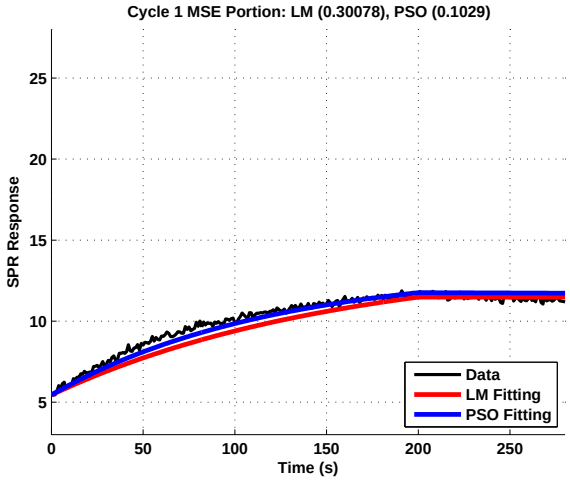

(a)

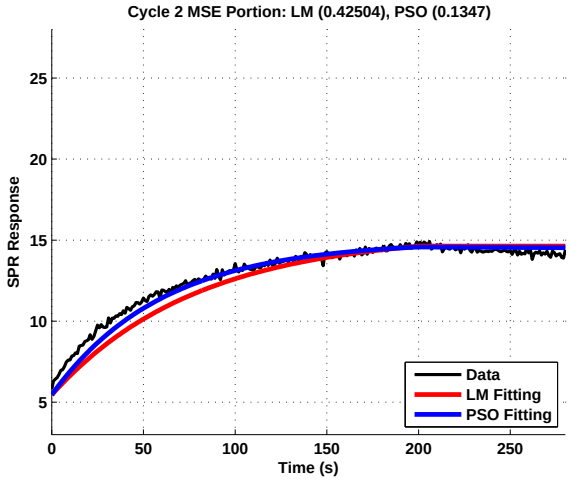

(b)

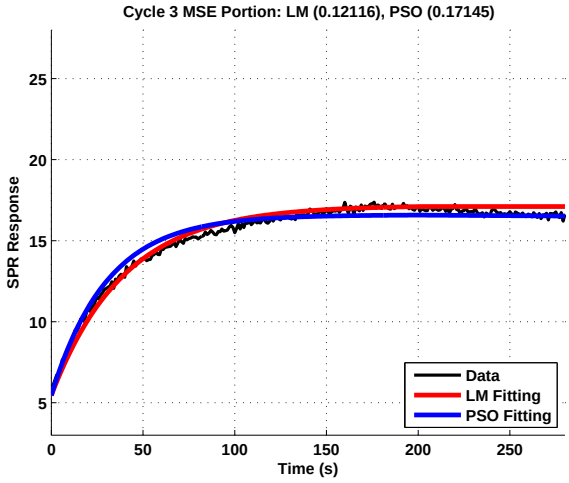

(c)

	$k_a(s^{-1}M^{-1})$	$k_d(s^{-1})$	MSE
LM	3.8100×10^4	0	0.8470
PSO best	4.9719×10^4	6.3409×10^{-5}	0.4091

The ranges of parameters obtained by PSO in 100 Monte-Carlo runs are below:

$$4.9062 \times 10^4 < k_a < 5.0259 \times 10^4$$
$$0 < k_d < 6.3409 \times 10^{-5}$$
$$0.4091 < \text{MSE} < 0.4192$$

Figure A.48: PSO curve fitting result for spot 90

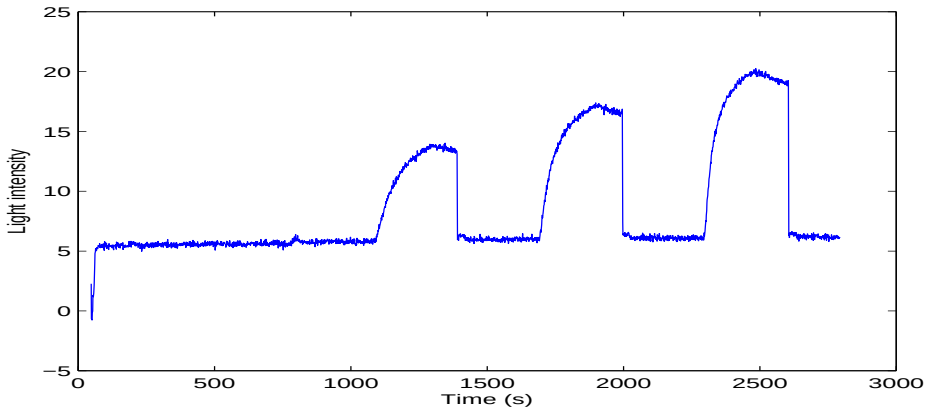

Figure A.49: SPR curve of Spot 91

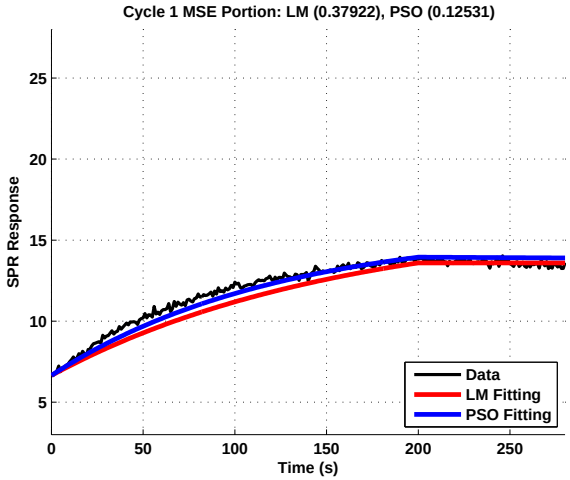

(a)

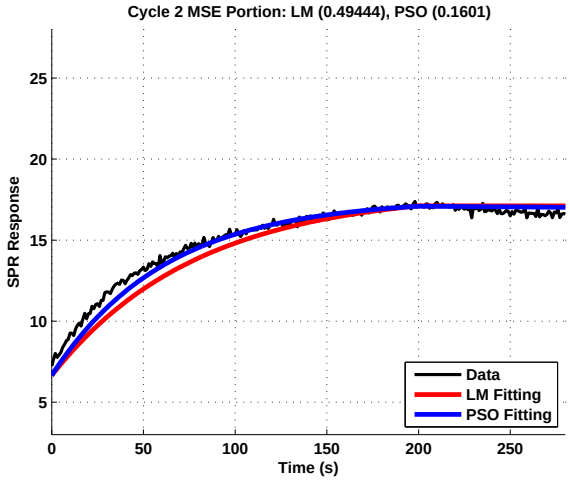

(b)

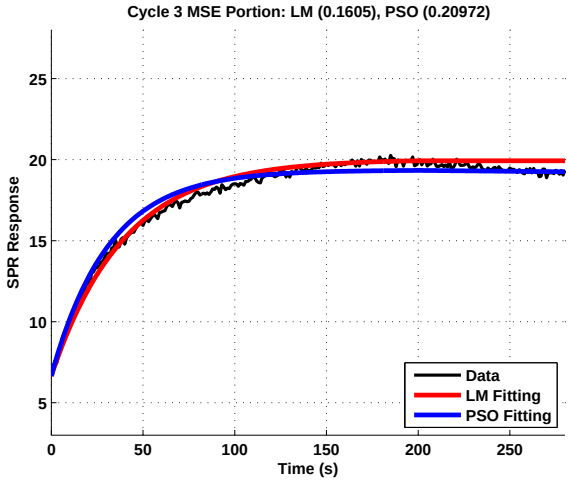

(c)

	$k_a(s^{-1}M^{-1})$	$k_d(s^{-1})$	MSE
LM	3.8000×10^4	0	1.0342
PSO best	4.8193×10^4	8.2558×10^{-5}	0.4951

The ranges of parameters obtained by PSO in 100 Monte-Carlo runs are below:

$$4.5579 \times 10^4 < k_a < 4.8658 \times 10^4$$
$$0 < k_d < 8.2558 \times 10^{-5}$$
$$0.4951 < \text{MSE} < 0.5258$$

Figure A.50: PSO curve fitting result for spot 91

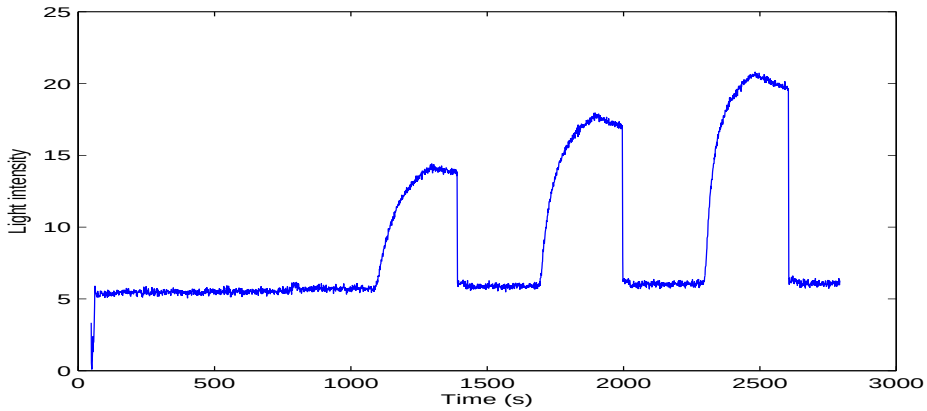

Figure A.51: SPR curve of Spot 92

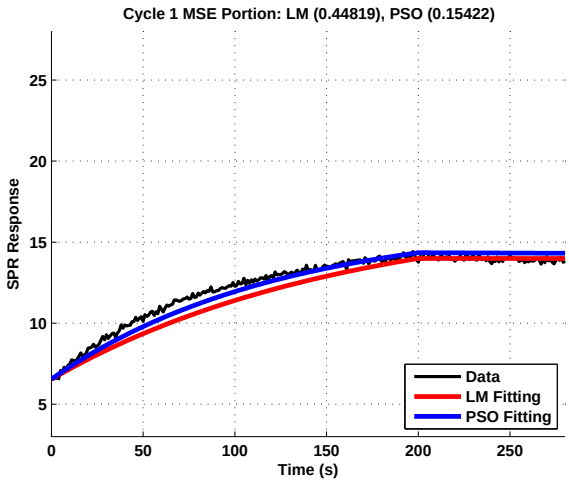

(a)

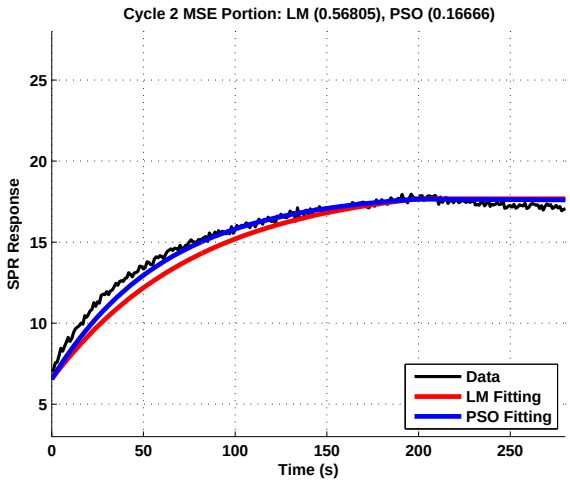

(b)

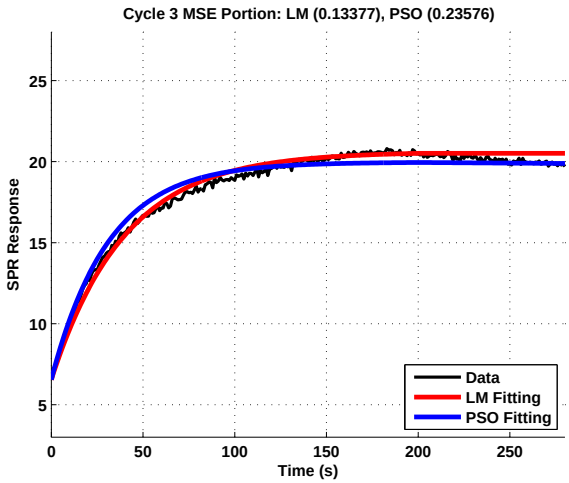

(c)

	$k_a(s^{-1}M^{-1})$	$k_d(s^{-1})$	MSE
LM	3.7600×10^4	0	1.1500
PSO best	4.8336×10^4	5.5014×10^{-5}	0.5566

The ranges of parameters obtained by PSO in 100 Monte-Carlo runs are below:

$$4.5364 \times 10^4 < k_a < 4.8720 \times 10^4$$
$$0 < k_d < 5.8207 \times 10^{-5}$$
$$0.5566 < \text{MSE} < 0.5787$$

Figure A.52: PSO curve fitting result for spot 92

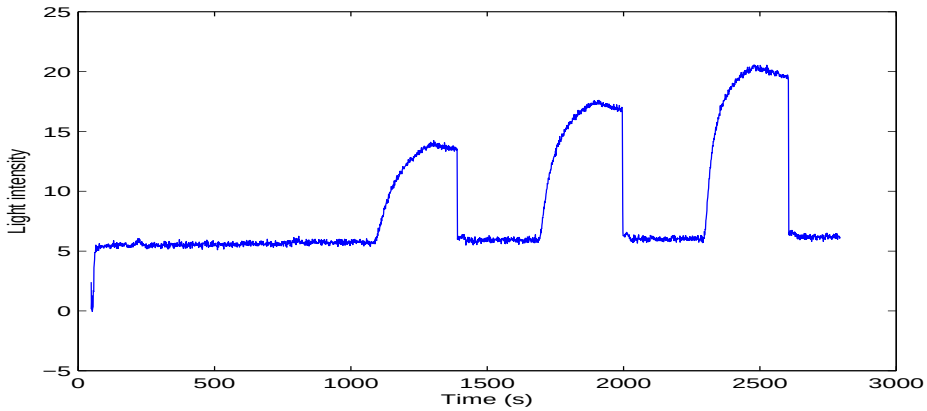

Figure A.53: SPR curve of Spot 93

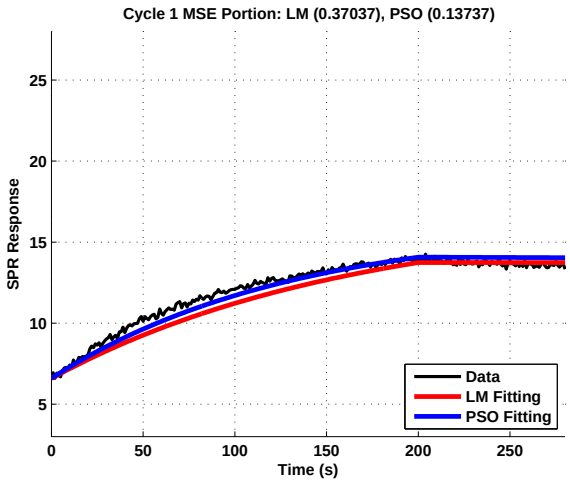

(a)

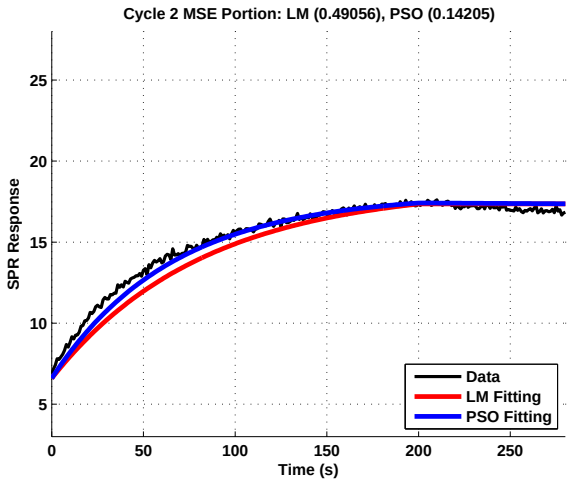

(b)

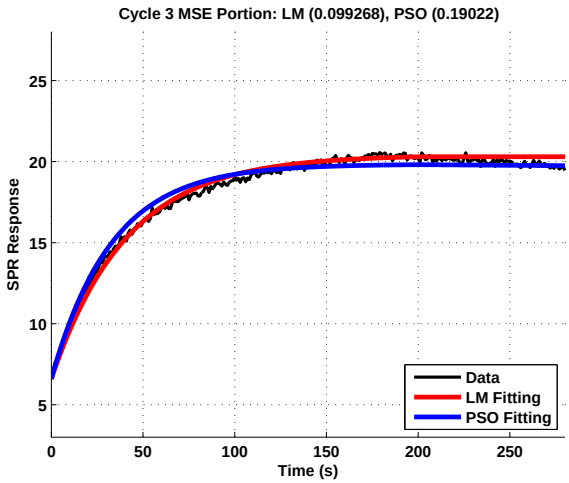

(c)

	$k_a(s^{-1}M^{-1})$	$k_d(s^{-1})$	MSE
LM	3.6500×10^4	0	0.9602
PSO best	4.5642×10^4	5.8846×10^{-5}	0.4696

The ranges of parameters obtained by PSO in 100 Monte-Carlo runs are below:

$$4.4308 \times 10^4 < k_a < 4.5978 \times 10^4$$
$$0 < k_d < 5.8846 \times 10^{-5}$$
$$0.4696 < \text{MSE} < 0.4873$$

Figure A.54: PSO curve fitting result for spot 93

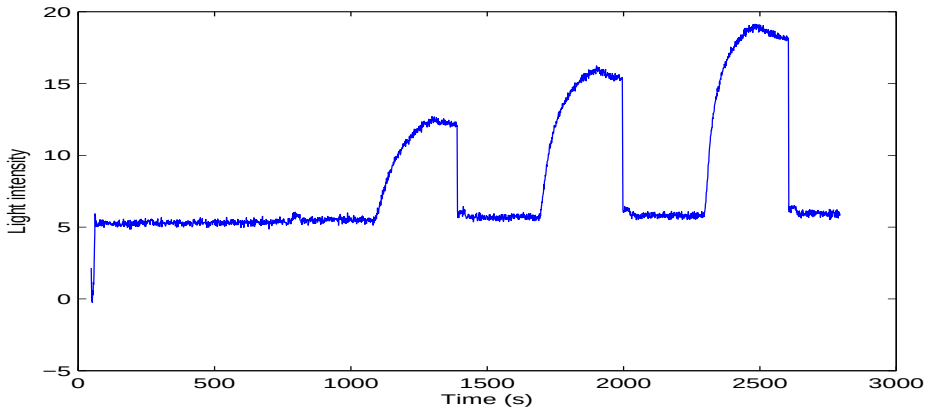

Figure A.55: SPR curve of Spot 94

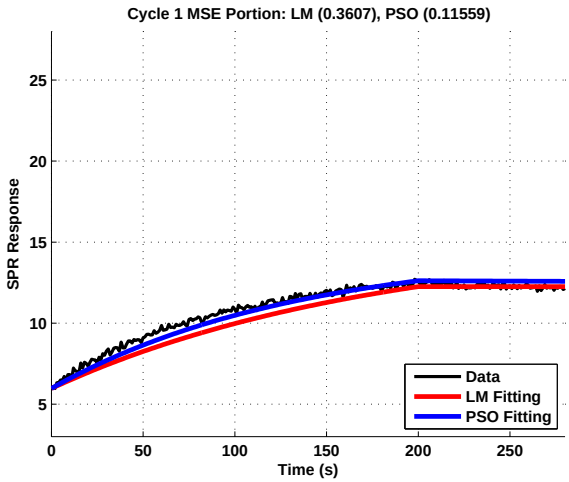

(a)

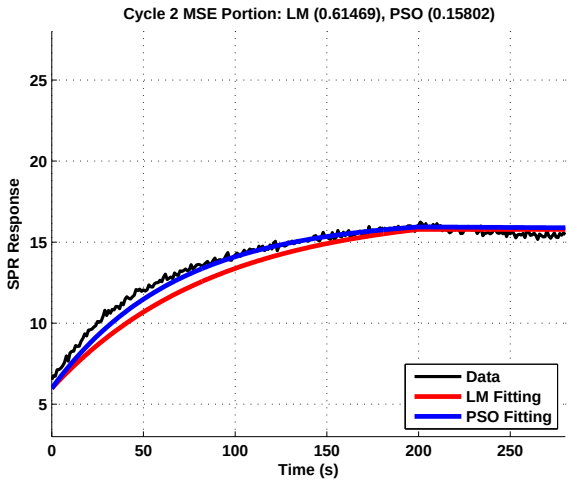

(b)

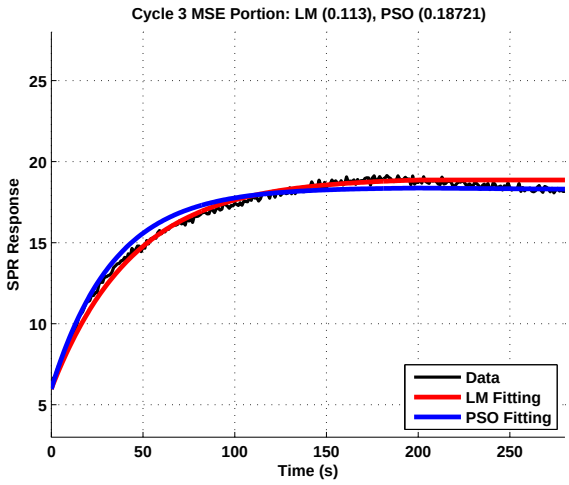

(c)

	$k_a(s^{-1}M^{-1})$	$k_d(s^{-1})$	MSE
LM	3.3700×10^4	0	1.0884
PSO best	4.4378×10^4	6.7123×10^{-5}	0.4608

The ranges of parameters obtained by PSO in 100 Monte-Carlo runs are below:

$$4.4378 \times 10^4 < k_a < 4.4774 \times 10^4$$
$$0 < k_d < 6.7123 \times 10^{-5}$$
$$0.4608 < \text{MSE} < 0.4734$$

Figure A.56: PSO curve fitting result for spot 94

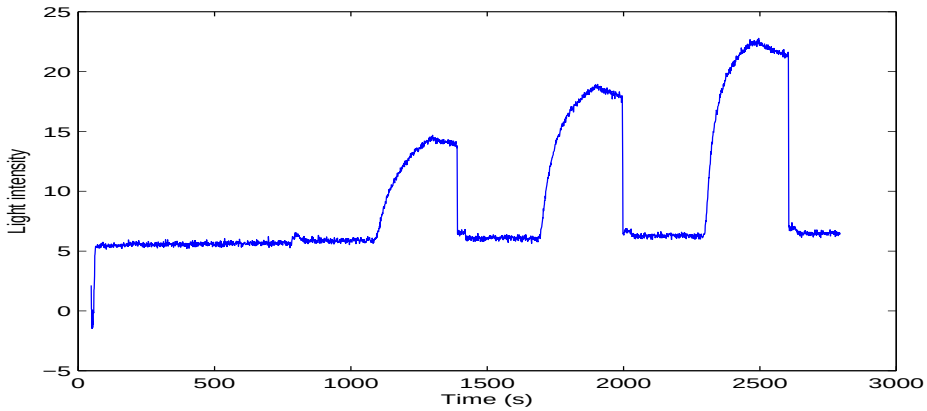

Figure A.57: SPR curve of Spot 95

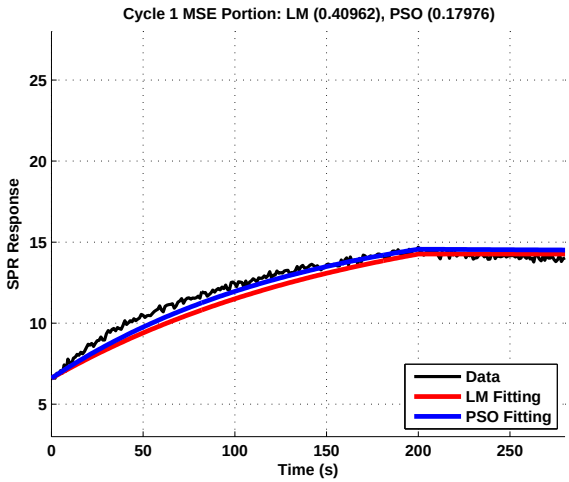

(a)

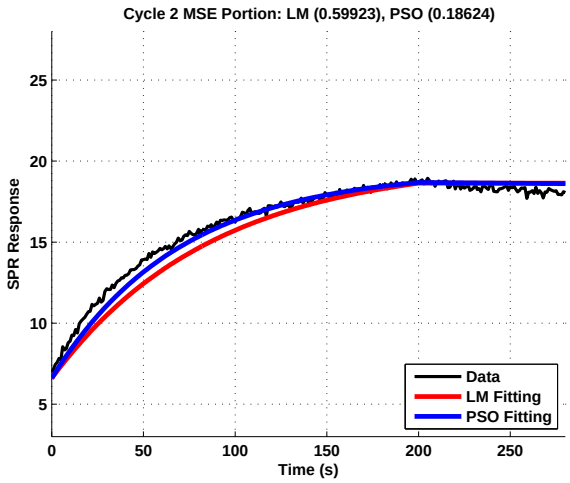

(b)

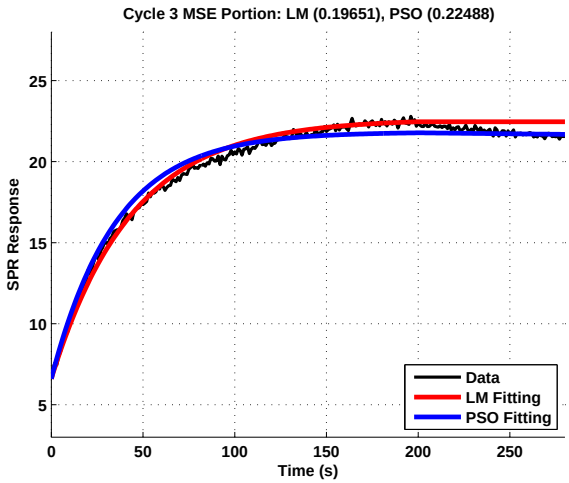

(c)

	$k_a(s^{-1}M^{-1})$	$k_d(s^{-1})$	MSE
LM	3.4400×10^4	0	1.2054
PSO best	4.2790×10^4	7.9544×10^{-5}	0.5909

The ranges of parameters obtained by PSO in 100 Monte-Carlo runs are below:

$$4.2790 \times 10^4 < k_a < 4.3313 \times 10^4$$
$$0 < k_d < 7.9544 \times 10^{-5}$$
$$0.5909 < \text{MSE} < 0.6131$$

Figure A.58: PSO curve fitting result for spot 95